Study of the Geoelectric fields at Vostok, Antarctica

Rita Corney, B.Sc.(Hons)

Submitted in fulfillment of
the requirements for the Degree of

Master of Science

School of Institute of Antarctic and Southern Ocean
Studies, Mathematics and Physics
University of Tasmania

October, 2002

Abstract

In fair weather regions, a downward directed geoelectric field of $\sim$ 100 – 200 Vm^{-1} can be measured at the surface of the Earth. At high latitudes, the interaction of the solar wind and interplanetary magnetic field with the Earth's magnetosphere and ionosphere imposes a variable dawn-to-dusk potential drop of 20 – 150 kV on the geoelectric field. Large scale horizontal electric fields in the ionosphere map into the vertical component of the near surface electric field. A total of 133 fair weather days of vertical geoelectric field data from Vostok, Antarctica (78.5°S, 107°E; corrected geomagnetic latitude, 83.5°S), obtained during 1998, were selected to investigate the suitability of the Vostok site for studies of the global electric circuit and confirm the linkage between the solar wind imposed potential patterns and the near surface electric field.

Seasonal variations in the diurnal electric field at Vostok are compared with the Carnegie diurnal curves, after appropriate allowance is made for the influence of the solar wind. Consistent features include the shift to later UT hours of the maximum between Southern Hemisphere (SH) summer and winter months, the seasonal constancy of the timing of the diurnal minimum and the diurnal range of the total dataset. The range of the diurnal curves, expressed as a percentage of the mean, increases by 7 to 9% when the imposed polar cap potential contribution is subtracted. The range of the total diurnal curve increases from 28% to 37% of the mean value, comparable with the Carnegie value of 37%. However, the diurnal range of the Vostok SH summer diurnal curve, 51% of the mean value, is excessive compared to the Carnegie value of 40%. The average magnitude of the electric field at Vostok peaks in the SH winter and is a minimum in the SH summer, consistent with global thunderstorm activity and monthly averages of recently re-analysed Carnegie data [Adlerman and Williams, 1996]. However, the Vostok equinoctal mean is similar to the Vostok SH winter mean while the Carnegie equinoctal mean is similar to the Carnegie SH summer mean. Broad

similarity of the Vostok and Carnegie diurnal-seasonal variations confirms Vostok as a suitable site for global circuit studies but the possibility that the comparisons are influenced by seasonal and diurnal variations in the average conductivity at ground level or possible inaccuracies in the ionospheric potential model used to subtract the influence of the solar wind on the Vostok data cannot be excluded.

Variations of the vertical electric field measurements are compared with both Weimer [1996] and IZMEM [Papitashvili et al., 1994] model calculations of the imposed polar cap potential above Vostok station. Variations of the electric field measurements are calculated using two previously published procedures, a monthly method as used by Frank-Kamenetsky et al. [2001], and a yearly method as per Frank-Kamenetsky et al. [1999]. By investigating the correlations between these parameters for individual UT hours, we confirm and extend the diurnal range over which sigificant correlations have been obtained. Using the yearly method, nineteen individual UT hours are significantly correlated with the Weimer model predictions and ten with the IZMEM model predictions. The linkage between ionospheric potential differences above Vostok and ground-level vertical electric field is clearly demonstrated. The ratio between the two variables is expected to be contant. Diurnal variations in the magnitude of the ratio for individual UT hours allows both models to be tested against the measured Vostok data, demonstrating that Antarctic polar plateau geoelectric field measurements can be used to investigate polar convection.

Declaration

This thesis contains no material which has been accepted for a degree or diploma by the University or any other institution, except by way of background information and duly acknowledged in the Thesis, and to the best of the Candidate's knowledge and belief no material previously published or written by another person except where due acknowledgement is made in the text of the Thesis.

Rita Corney

Rita Corney

Acknowledgements

My sincerest thanks to the following people:

- Gary Burns and Kelvin Michael, my supervisors. Thank you for all your support. You have both been the best supervisors a student could possibly ask for.

- All my office mates over the last two years: Teresa, who told me that pregnancy was not contagious; I soon proved her wrong. Alix, who is finishing the hard way, working fulltime as well as writing up. Wendy, Dave, Adam, Kristen and Pat, it has been a pleasure to share an office with you, however short that time may have been.

- All members of the IASOS and the Antarctic CRC, for making this a wonderful place to do a postgraduate degree.

- Frank Sainsbury, for all his computer support and friendship over the last two years.

- Jason Roberts, for being foolish enough to have an office nearby and knowledgeable enough to answer all my questions.

- Simon Wotherspoon (Spoon), for his knowledge of statistics.

- Anthony Breed, for his assistance with the ionospheric electric potential models. Sadly, Anthony passed away before seeing this final version.

- Jim and Michaela, for being the best friends a person could have and refusing to talk to me until I had finished.

- Emily, for encouraging me to finish so that she could discuss Star Wars with Stuart.

- Jim Bashford, for offering to proof read my thesis and then doing so within 24-hours.

- Mum, John, Dad, Audrey and Celena, for being very supportive with everything I have endeavoured to do.
- Katherine and Max, for being great in-laws and encouraging me to have more children.
- Inessa and Raphaela, you make everyday a wonderful day. You are my sweet and crazy "goggle-girts".
- Last but not least, Stuart, my wonderful husband. There are not enough words to convey everything I want to say, $\times^a$; $a \to \infty + 1$.

'Never for me the lowered banner, never the last endeavor'

Sir Ernest Shackleton

'She plays without the music, her eyes sometimes on her hands, sometimes closed. What she hears, what she imagines I do not know. There is no forced gravitas in her playing. It is a beauty beyond imagining - clear, lovely, inexorable, phrase across phrase, phrase echoing phrase, the incomplete, the unending "Art of Fugue". It is an equal music.

Music, such music, is a sufficient gift. Why ask for happiness; why hope not to grieve? It is enough...to live from day to day and to hear such music - not too much, or the soul could not sustain it - from time to time' An Equal Music,

Vikram Seth

Contents

Chapter 1

Introduction

Wilson [1920] first hypothesised that global thunderstorm activity maintains an electric potential between the ionosphere and the surface of the Earth. Thunderstorm activity draws current upward to the ionosphere and is partially responsible [Williams and Heckman, 1993] for a time-varying potential difference of the order of 250 kV directed downward from the ionosphere to the ground. Currents in the circuit are dispersed around the globe via the ionosphere and the magnetosphere, to eventually return to the ground. In fair weather regions, a downward directed geoelectric field of $\sim 100 - 200$ Vm^{-1} can be measured near the surface. The geoelectric field is responsive to variations in global current sources, including thunderstorm activity, on timescales of the order of 20 minutes [Bering et al., 1998]. Overviews of the development and present status of research in geoelectricity are provided by Bering et al. [1998], Tinsley [2000] and Rycroft et al. [2000].

The global significance of geoelectric field measurements is more readily observable in regions where local diurnal variations of atmospheric conductivity are small; over oceans, in polar regions and at some mountain sites. Sites are judged as suitable for such studies if the average diurnal variation as a function of Universal Time (UT), is consistent with the average fair-weather electric-field diurnal variation derived from measurements made during the voyages of the research ship Carnegie in the early decades of the last century [e.g. Reiter, 1992, p. 129].

The Carnegie measurements were made over the ocean where diurnal variations in conductivity are minimal and are representative of the global electric field. Previous studies have shown Vostok to be a suitable site for studies of the global electric circuit [Park, 1976b, Frank-Kamenetsky et al., 1999, 2001].

At high latitudes, the interaction of the solar wind and the Earth's magnetic field imposes on the geoelectric field a variable dawn-to-dusk potential drop of between 20 and 150 kV. Large-scale (> 200 km) horizontal electric fields in the ionosphere map into the vertical component of the electric field near the Earth's surface [Park, 1976a]. Burns et al. [1998] showed that the geoelectric field at Vostok is modulated by the B_y component of the interplanetary magnetic field (IMF) during times when Vostok is magnetically linked to the dayside interaction region between the solar wind and the Earth's magnetic field. Tinsley et al. [1998] compared variations of the surface electric field, ΔE_Z (the observed electric field measurements at South Pole minus the Carnegie curve scaled to the average of E_Z for $4-6$ UT and $14-16$ UT hours for each individual day) with variations in the calculated overhead ionospheric electric potentials, Φ_{AV}, inferred using the Hairston and Heelis [1990] model. The authors found positive correlations with a slope of ~ 0.7 Vm^{-1}/kV and correlation coefficients of ~ 0.5. Using chart-scaled hourly data, Frank-Kamenetsky et al. [1999] showed that the vertical electric field measured at Vostok was significantly correlated with IZMEM model [Papitashvili et al., 1994, 1995] calculated cross-polar-cap potential differences above the site, for six individual hours. Frank-Kamenetsky et al. [2001] introduced a modern Vostok data set and reported statistically significant linkages between the vertical electric field and B_y and B_z components of the IMF.

The seasonal variation of the average diurnal curve is of interest in terms of its relationship to variations in the global electric circuit generators [Adlerman and Williams, 1996, Israel, 1973, p. 350-351]. Frank-Kamenetsky et al. [2001] demonstrated the existence of a seasonal variation in the geoelectric field at Vostok, with an observed range of 40 Vm^{-1}, a maximum in August and minima in April and December. However, in determining the global circuit diurnal curve and its

seasonal variation in polar regions, the influence of the cross-polar-cap potential difference imposed by the interaction of the solar wind and the Earth's magnetic field [Tinsley et al., 1998, Frank-Kamenetsky et al., 1999] can be significant and should be accounted for.

The objectives of this thesis are:

- To determine if fair-weather diurnal curves can be observed at Vostok station, Antarctica, using the modern electric field mill and hence verify the suitability of the site for studies of the global electric circuit.
- To investigate further, the linkage between solar wind imposed potential patterns and near-surface electric field measurements.
- To determine if the agreement between the Vostok seasonal diurnal curves and the Carnegie curves can be improved by allowing for the cross-polar-cap potential difference.
- To compare the accuracy of two ionospheric electric potential models, the Weimer [1996] and IZMEM [Papitashvili et al., 1994] model, in predicting the ionospheric electric potential patterns above Vostok.
- To compare two methods of calculating variations in the average electric field measurements.

The structure of the thesis is outlined below:

Chapter 2 contains the background material necessary for an understanding and appreciation of the setting of this work. It begins with a review of the history of atmospheric electric field measurements. A brief description of the Carnegie results is presented as well as the re-analysis by Adlerman and Williams [1996], followed by a description of conductivity in the atmosphere and how it varies. The last section discusses the global electric circuit, including its sources and generators and solar wind modulation.

In Chapter 3, different models of ionospheric electric potentials are discussed. The two models which are employed in this thesis, Weimer and IZMEM, are outlined in detail, including a summary of the necessary input data and a comparison of their respective derivations.

Chapter 4 describes the instrumentation as well as criteria used for the selection of data. It contains a discussion of the electric field mill and the modifications that were made before deployment at Vostok station. Details are given of the fair-weather criteria used to select the 133 days of fair-weather geoelectric field measurements, as well as descriptions of the interplanetary magnetic field data used to calculate the cross-polar-cap potential differences above Vostok.

Chapter 5 investigates the diurnal and seasonal variation of the near-surface electric field measurements. Comparisons with the Carnegie curves are discussed. The influence of the solar wind interaction with the Earth's magnetosphere, clearly demonstrated in Chapter 6, is accounted for in the near-surface electric field measurements. The influence on the range of the diurnal curves observed at Vostok is shown to be significant.

Chapter 6 contains the second major result of this thesis. It demonstrates the influence of the solar-wind-imposed ionospheric potential differences on near-surface electric field measurements. The results of these correlations are used to compare the Weimer and the IZMEM models, as well as the monthly and yearly methods.

Finally, Chapter 7 presents the conclusions of this study as well as suggestions of future work.

Chapter 2

Background Material

This chapter gives an historical overview of the global electric field, from early studies of lightning and thunder to the cruises of the *Carnegie* research vessel. The widely-accepted Carnegie results are detailed as well as the results of the re-analysis of the Carnegie and Maud datasets by Adlerman and Williams [1996]. The conductivity of the atmosphere is described, including details of the various processes contributing to the atmospheric conductivity in each of the ionospheric layers and their variation with altitude and latitude. The last section describes the global electric circuit and the main sources of electromotive force; thunderstorms, the interaction of the solar wind with the magnetosphere and the atmospheric tides in the thermosphere.

2.1 Historical review - Wall to Whipple

Studies of atmospheric electricity became popular during the 18th century, begining with observations and theories of thunder and lightning and progressing to structured, scientific experiments. In 1707, Wall hypothesised that the crackling sparks discharged from a piece of rubbed amber appeared to be similar in nature to that of lightning [Reiter, 1992]. He theorised that lightning was a manifestation of static electricity. In 1752, Franklin achieved a major breakthrough when he designed the first systematic and scientific experiment to determine whether

or not thunderstorm clouds were electrified. He theorized that if thunder clouds were electrically charged then it would be possible to draw lightning from the clouds down to the ground. The experiment involved a person standing on a metal stand, fitted with a pointed metal rod rising some 6-10 metres into the air, and bringing a grounded wire near the rod to test if electricity was being conducted from the clouds through the metal rod. D'Alibart carried out this experiment and confirmed the electrical nature of thunderstorm clouds. Franklin modified his original experiment and replaced the metal rod with a kite. By measuring the sign of the charge delivered, he was able to infer that the lower regions of thunderstorm clouds were, in general, negatively charged. Le Monnier (in 1752) repeated and refined Franklin's original experiment. He strung a long wire from the iron rod to a nearby building. At the end of the wire, experiments involving sparking and the electrification of various objects, were carried out. Dust particles placed near the end of the wire were used to detect weak cases of electrification. Le Monnier found that the dust particles' attraction to the wire not only occurred on days when thunderstorm clouds were present, but also on days with very few clouds overhead. He concluded that the existence of electricity in the atmosphere was not dependent on the weather conditions or the presence of thunderstorm clouds and was in fact, a permanent feature of the atmosphere; he had discovered fair-weather electricity. Further experiments soon provided the first qualitative information on the diurnal variation of the electrical state of the atmosphere. Beccaria established the diurnal variation of the electrical state of the atmosphere and observed that electric charges found near the surface were of different signs, depending on the weather conditions. In 1785, Coulomb observed that a well-insulated conductor, exposed to air, gradually lost its charge and concluded that air had a conductive property. His observations, however, were not well understood at the time and lay forgotten for more than a century. Erman, in 1804, observed that the measured electric charge decreased with decreasing height and concluded that the Earth's surface was negatively charged.

The biggest advancement was achieved by William Thomson (later known as

Lord Kelvin) in 1860. He brought together all the separate pieces of information and formed a coherent system of atmospheric electricity. Thomson introduced the concepts of electric potential and electric field, and constructed the first precise instruments capable of continuously measuring parameters of atmospheric electricity. He likened the fair-weather electric field to that formed by a spherical capacitor. The ionosphere acts as the positive plate with a potential of $\sim$ 250 kV with respect to the Earth's surface, which was the negative plate. The atmosphere in between acted as a leaky dielectric, discharging an average current of about 1 kA integrated over the Earth's surface [Bering, 1995]. An average potential gradient of about 120 Vm^{-1} can be detected at the Earth's surface. This configuration is known as the DC global circuit.

The discovery of cosmic-ray ionization provided an explanation for Coulomb's observation that air was a conductor and allowed measurements of the conductivity of air to be carried out, as well as the determination of its dependence on the ion content of the air. As a result of this finite electrical conductivity, a vertical conduction current flows from the ionosphere down to the earth's surface. The continued existence of this current suggests that some mechanisms exist which oppose the flow of currents to the Earth's surface and act as a power source for the global circuit. Many experiments followed, enquiring into possible power sources. The first such experiments were carried out by Simpson in Lapland and Antarctica from 1905 to 1919. His results showed a single daily maximum but with a time difference between the two hemispheres. Hoffman in 1924 related the measurements to universal time instead of local time and found that the daily maxima occurred simultaneously [Reiter, 1992].

The data collected by the Carnegie cruises, which occurred during 1915-1929 over open ocean waters, provided the first really conclusive and reproducible evidence. A variation with Universal Time of the hourly average curve of electric potential gradient near the surface of the Earth was found by Mauchly [Reiter, 1992]. The Carnegie curves, as they are now known, are still used to provide a measure of the accuracy of attempts to measure worldwide variations of electri-

cal potentials and conduction currents in the atmosphere [Rycroft et al., 2000]. Detailed information about the Carnegie results and analyses are provided in the following section.

The next major development was achieved by Wilson in 1925. He proposed that global thunderstorm activity maintained the global electric potential between the ionosphere and the surface of the Earth. His theory was confirmed by Whipple and Scase in 1929 and 1936 [Reiter, 1992]. They showed, using data from the Carnegie and Maud cruises, that the diurnal variation of the electric field exhibited the same pattern over all parts of the Earth and was correlated strongly with global thunderstorm variations [Reiter, 1992].

More detailed historical accounts are provided by Reiter [1992] and Israel [1973], the information provided here is meant to give a brief overview, only.

2.2 The Carnegie Results

The results of the Carnegie cruises (1915-1929) established the existence of a common UT-dependent variation in the near-surface electric field. The Carnegie measurements were made over the open ocean, where atmospheric conductivity variations are relatively low. The diurnal variation that was observed, referred to now as the Carnegie curve, is commonly used as a benchmark of a site's suitability for studies of the global electric circuit. The Carnegie curves during SH winter, summer, equinox and in total are shown in Figure 2.1. The amplitude of the diurnal variation and the time of the minimum are not dependent on the season. The minimum consistently occurs between 3 and 4 UT but the time of the maximum varies between 18 UT and 21 UT depending on the season. The SH summer curve peaks first at 17.5 UT, followed by the equinox and total curves at 19.5 UT and the winter curve at 20.5 UT. The range of the total curve is 37% of the mean, the SH summer curve is 40% and the equinox and winter curves are both 31%.

Analysis of the Carnegie data also demonstrated that the electric field inten-

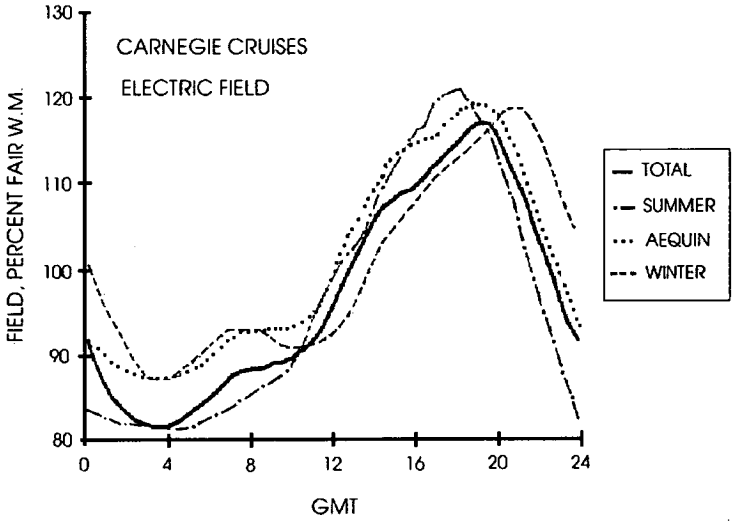

Figure 2.1: The Carnegie curves: Fair-weather diurnal variation of the electric field in percent of the fair-weather mean measured by the Carnegie vessel. Data subdivided with respect to austral seasons; winter - May to August, summer - November to February, equinox - March, April, October, November (figure taken from Reiter [1992] but modified to show Southern Hemisphere seasons).

sity varies seasonally, with a maximum in the NH winter (SH summer) [Parkinson and Torreson, 1931]. The electric field intensity was found to be 30% greater in winter than in summer. Early measurements of the seasonal variation of the atmospheric potential gradient at land-based stations in the northern hemisphere displayed a NH winter peak. Stations in the southern hemisphere, however, displayed an inverse trend, maximising during the NH summer. The idea of a NH winter maximum contradicts current knowledge of worldwide thunderstorm activity and temperature variations as well as seasonal variations of ionospheric potential, all of which indicated the presence of a NH summer peak. Previous explanations of the apparent winter peak have focused mainly on the seasonal distribution of thunderstorm activity and local influences but the discrepancy remained unresolved due to uncertainties involved in the accurate assesment of global thunderstorm activity. Analyses of air-Earth current measurements from

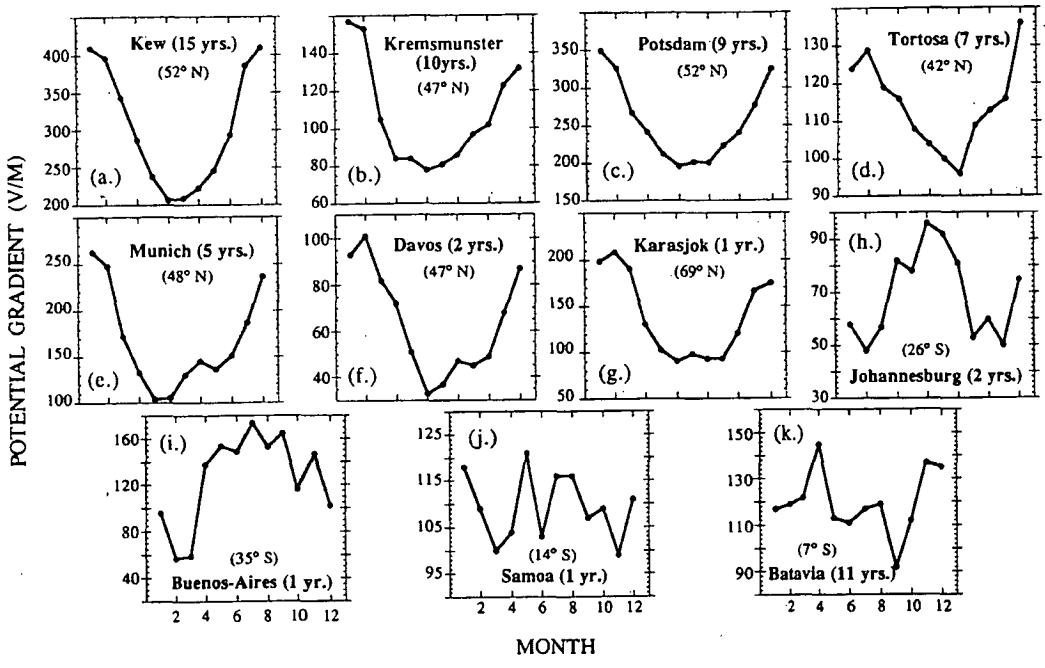

Figure 2.2: (a)-(g) Early measurements of the seasonal variation in potential gradient at northern hemisphere stations, (h)-(i) southern hemisphere stations and (j)-(k) tropical stations [Adlerman and Williams, 1996].

Mauna Loa by Adlerman and Williams [1996] again supported the idea of a NH summer maximum rather than a winter maximum in electric field components, compelling the authors to question the results of Parkinson and Torreson [1931]. Figure 2.3 shows several examples of common diurnal variation of the air-Earth current. A peak around 1900 UT and a minimum around 0100 UT to 0300 UT can be seen in each curve. Averaging of all the data (from the 1970 to 1983 dataset) by month, produced an annual variation with a peak in June and July (see Figure 2.4), consistent with the peak of the global thunderstorm activity but conflicting with reported variations of the Carnegie electric field measurements.

Investigations by E J Adlerman found that the original analysis by Parkinson and Torreson [1931] was based on a sampling of only 82 days from cruise VII of the Carnegie vessel, which included only seven days from the months May, June and July [Adlerman and Williams, 1996]. A re-analysis of the entire Carnegie and Maud datasets revealed that the mean potential gradient did in fact peak during

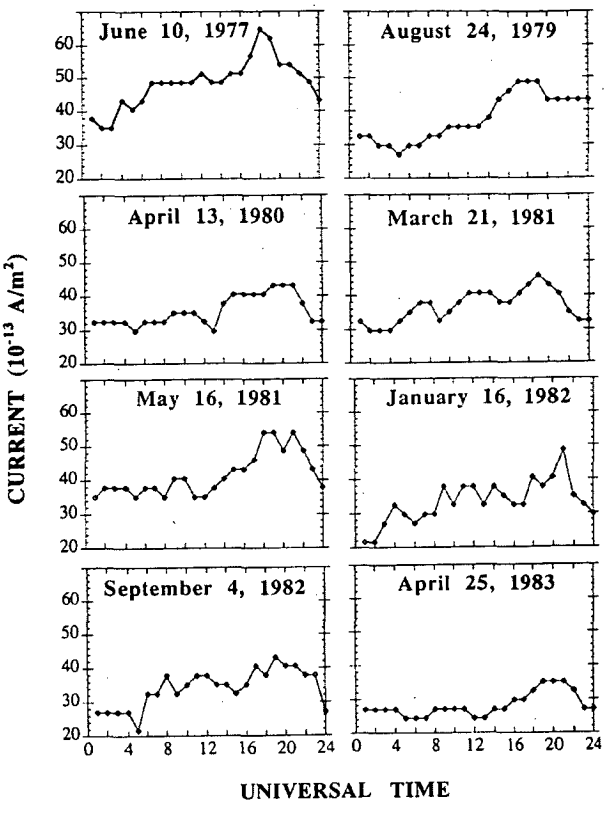

Figure 2.3: Typical diurnal variations in air-Earth current measured at Mauna Loa, Hawaii, from 11977 to 1983 by W. E. Cobb (data unpublished, 1993). Note the similarity to the well-known Carnegie curve. Dates indicated [Adlerman and Williams, 1996].

the northern hemisphere summer. Figure 2.5 shows the average annual variation of potential gradient. A strong summer peak is evident in all the curves, thus confirming the air-Earth current results from Mauna Loa.

2.3 Atmospheric Conductivity

The ionosphere is a weakly ionised fluid of neutral net charge. Ionised particles can be created by short wavelength solar radiation (EUV and x-ray) or by precipitating energetic particles [Brasseur and Solomon, 1986]. The ionosphere is divided into several characteristic layers based on the mean vertical profile of electron density (see figure 2.6). The boundaries between the different layers are not

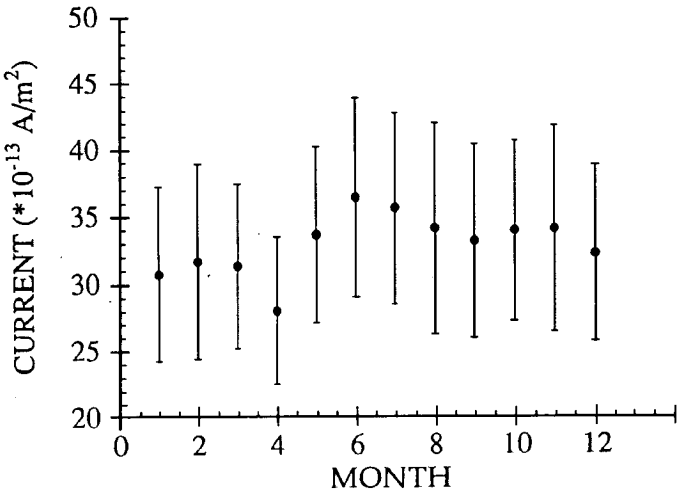

Figure 2.4: Seasonal variation of air-Earth current measured at Mauna Loa, Hawaii, from 1977 to 1983 by W.E. Cobb. Standard deviations of the data indicated. Standard deviations of the mean are all less than 0.30×10^{-13} Am^{-2} [Adlerman and Williams, 1996].

well defined and vary greatly with time, location and solar disturbances [Davies, 1990]. Energetic charged particles can penetrate into the Earth's atmosphere, propagating along the Earth's magnetic field lines in helical trajectories. In polar regions, magnetic field lines are open and cosmic rays can easily enter the atmosphere. The penetration depth of these charged particles depends on their mass and energy (see figure 2.7). Figure 2.8 shows the approximate penetration depth for different types of charged particles and x-rays produced by the precipitation of high energy particles. Ionised particles in the lower atmosphere are mainly created by galactic cosmic ray radiation. The cosmic ray flux is strongly attenuated as it comes down into the lower atmosphere, causing the electrical conductivity of the atmosphere to increase rapidly with altitude. The ionospheric potential is thus reached at the lower boundary of the ionosphere, less than 60 km above the surface [Tinsley et al., 1998]. At higher altitudes, free electrons and ions exist for long enough periods to take over as the main charge carriers [Rycroft et al., 2000].

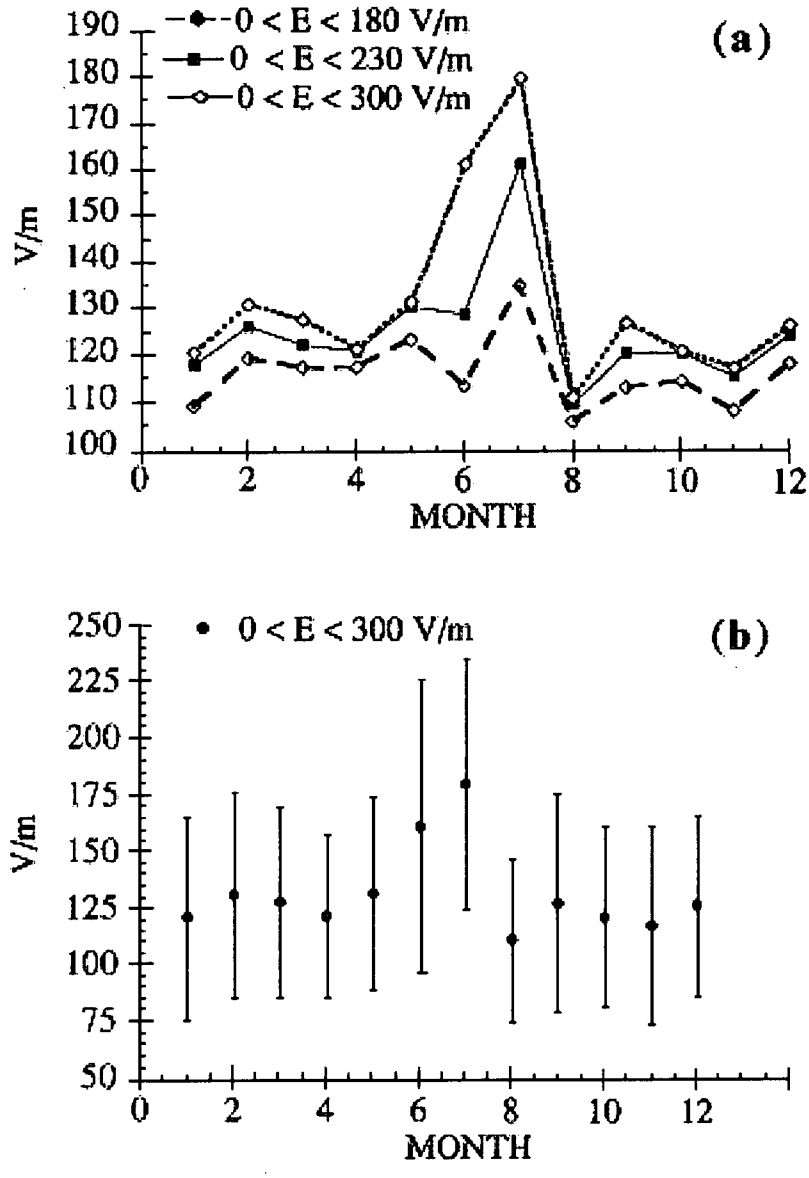

Figure 2.5: Seasonal variation of potential gradient measured by the Carnegie and Maud scientific expeditions and reanalysed by Adlerman and Williams [1996]: (a) variations over several ranges of potential gradient, $0 < E < 300$, $0 < E < 230$ and $0 < E < 180$ Vm^{-1}, (b) variations over $0 < E < 300$ Vm^{-1} with standard deviations of the data indicated. Standard deviations of the mean are all less than 3.2 Vm^{-1} [Adlerman and Williams, 1996].

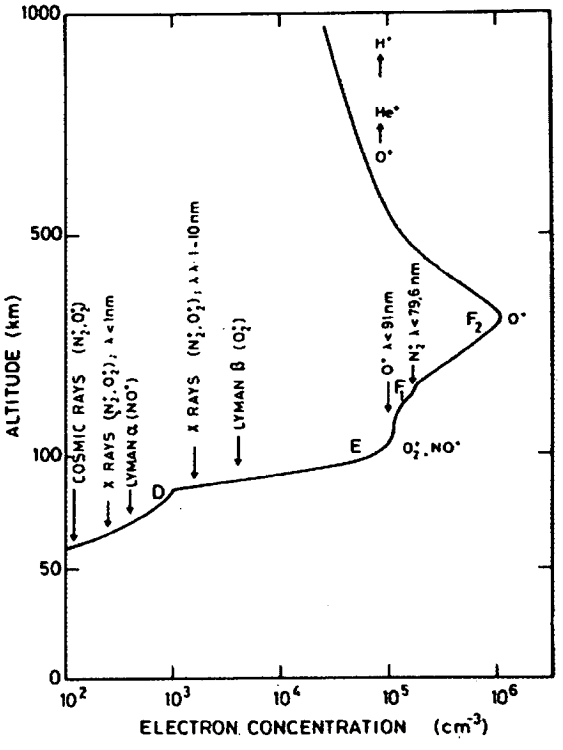

Figure 2.6: Definition of the ionospheric layers based on the vertical distribution of electron density [Brasseur and Solomon, 1986].

Although the ionosphere, at times, is considered to be a perfectly conducting layer, in reality it is not. The ionosphere possesses a finite conductivity and the electric currents and fields within it are driven by the combined action of the ionospheric and magnetospheric dynamo systems as well as by current generation from the lower atmosphere. This section will outline the types of ionisation processes occuring in the different layers of the atmosphere and ionosphere, the mobility of the ions and electrons and the variation of the electrical conductivity in that region.

2.3.1 The lower atmosphere and the ionospheric C layer

The ionospheric C layer and lower atmosphere are located below $\sim$ 60 km altitude. Small positive and negative ions in this region are created mainly by galactic

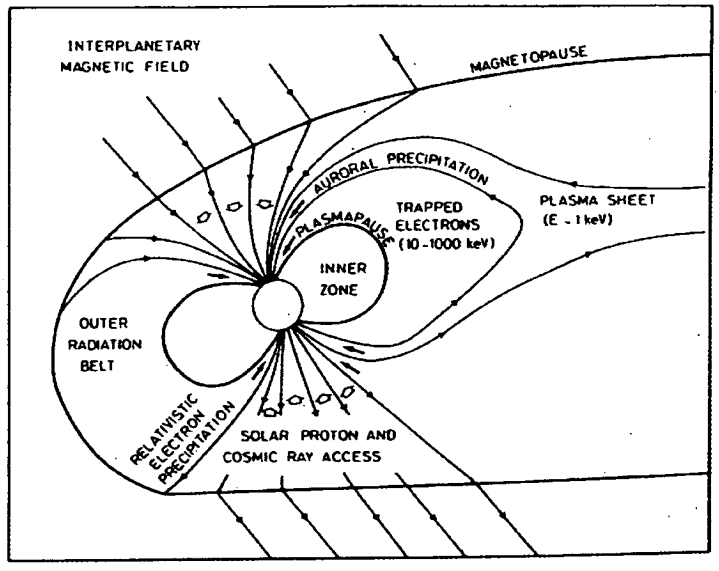

Figure 2.7: Schematic representation of the structure of the magnetosphere [Brasseur and Solomon, 1986].

cosmic ray ionisation [Rycroft et al., 2000]. In the lowest 100 m over land masses, radioactive decay of gases, mainly radon and thoron, leaching from the ground add to the rate of ionisation [Israel, 1973].

Galactic cosmic rays are produced outside the solar system, consisting mostly of protons and α particles. They tend to follow the magnetic field lines as they approach the earth, mainly penetrating near the magnetic poles (see figure 2.7). Galactic cosmic ray ionisation varies with latitude and altitude due to the Earth's magnetic field which acts as a cosmic ray filter [Roble and Tzur, 1986]. In the 0 to 60 km altitude range, the ion production initially increases exponentially with altitude,

$$\sigma_- = \sigma_0 \exp(\frac{z}{H}) \tag{2.1}$$

where $\sigma_0 = 4 \times 10^{-14}\ \Omega^{-1}\mathrm{m}^{-1}$, z is the altitude and H $\cong$ 6 km is the scale height [Dolezalek and Reiter, 1977], proportional to the atmospheric density. Cosmic ray ionisation reaches a maximum near 10 to 15 km (see figure 2.9).

High energy galactic cosmic ray particles penetrate into the atmosphere at low latitudes and only particles with energies greater than $\sim$ 15 GeV ever reach

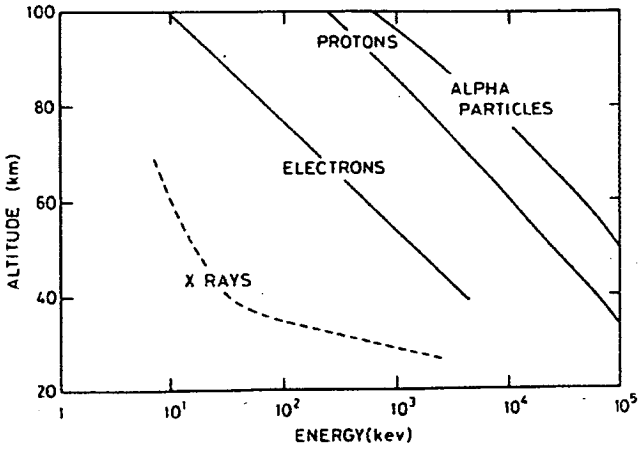

Figure 2.8: Depth of atmospheric penetration for different charged particles as a function of energy, as well as the altitude of bremsstrahlung x-ray penetration produced by the precipitation of high energy particles [Brasseur and Solomon, 1986].

the equator [Roble and Tzur, 1986]. Lower energy particles are progressively excluded by the Earth's magnetic field and particles with energies less than ~ 2 GeV are confined to latitudes above $\sim 50°$ [Tinsley and Heelis, 1993]. The cosmic ray ion production rate is nearly constant at these latitudes, indicating that the magnetic field is an inactive filter at or near the magnetic poles. Figure 2.10 shows the rate of ionisation by cosmic rays at different geomagnetic latitudes. Galactic cosmic ray fluxes are also modulated by the solar wind over the 11-year solar cycle. During periods of high solar activity, less galactic cosmic rays penetrate the Earth's magnetosphere, decreasing the conductivity, with larger changes occurring at higher latitudes than at lower latitudes [Tinsley and Heelis, 1993]. During periods of low solar wind activity the amplitude of the cosmic ray precipitation is increased, leading to a rise in the atmospheric conductivity. Figure 2.9 shows the rate of cosmic ray ionisation in the lower stratosphere and troposphere during a solar minimum and a solar maximum.

Approximately five times more ions are produced over the continents than over the seas, but on average the number density of ions over land and over sea are also approximately the same; 10^9 m^{-3}. The aerosol concentration of the atmosphere

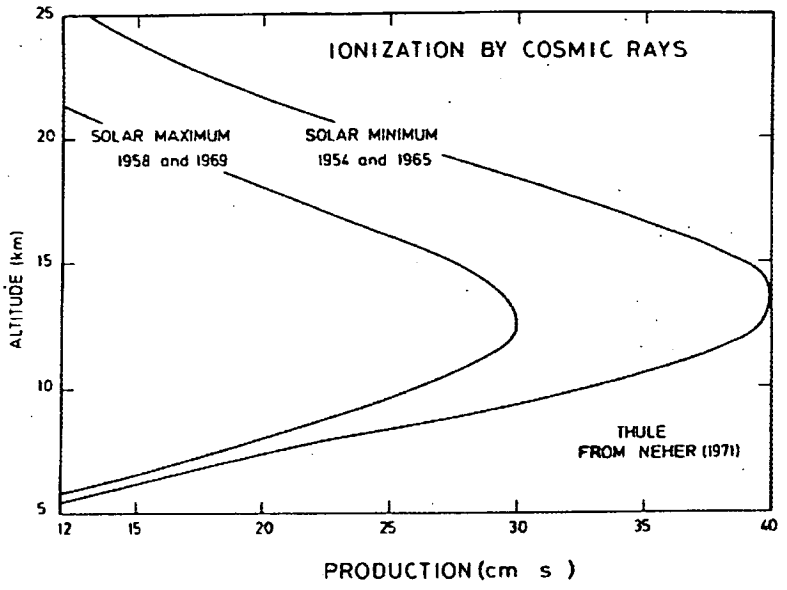

Figure 2.9: Rate of ionisation by cosmic rays in the lower stratosphere and troposphere [Brasseur and Solomon, 1986].

above the continents is approximately five times higher over the land resulting in an increase in the number of collisions between ions and neutral particles and a decrease in the number of small, fast ions. The fast ions become attached to the more massive particles (e.g. water particles within cloud or fog) decreasing their mobility and reducing the electrical conductivity of the atmosphere [Roble and Tzur, 1986]. The concentration of aerosols in the atmosphere is dependent on many factors; the meteorological conditions, the time of day, the season, the amount of pollution and other natural and man-made factors. It varies significantly with time and space, especially in the first kilometre above the ground. The conductivity also decreases later in the day due to the establishment of an exchange layer.

Up to 80 km altitude, the electrical mobilities of ions and electrons are dominated by collisions with the neutral gas and the frequency of the collisions is so high that the ions and electrons move with the speed of the neutral air. The variation of typical collision frequencies with altitude for ions and electrons is shown

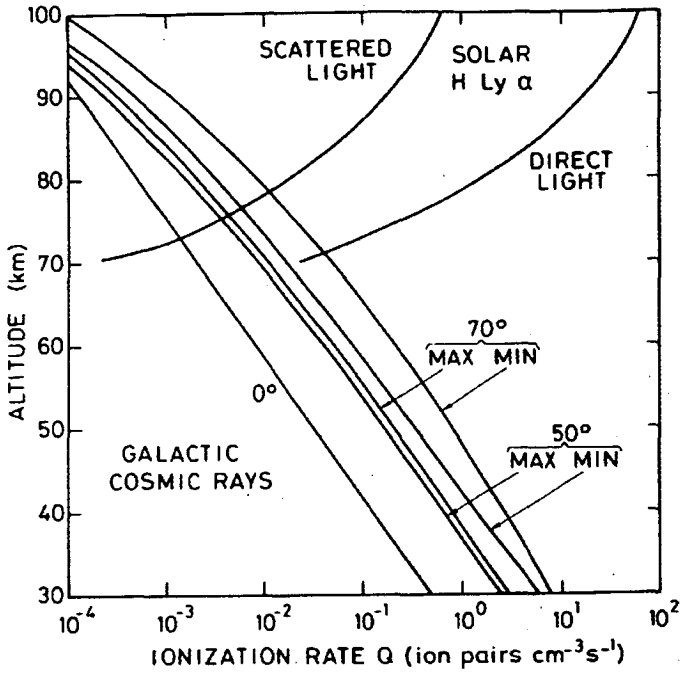

Figure 2.10: Rate of ionisation provided by cosmic rays at different geomagnetic latitudes (0°, 50° and 70°) and for minimum and maximum levels of solar activity [Brasseur and Solomon, 1986].

in figure 2.11. Under quiet conditions, the temperature of the upper atmosphere varies across the polar cap. It is highest near the sub-solar point and lowest on the nightside of the auroral oval. This temperature difference establishes a pressure difference across the polar cap that drives the horizontal neutral winds from the dayside to the nightside of the auroral oval [Davies, 1990]. This neutral wind motion is transferred to ions by neutral-ion collisions and to electrons by Coulomb attraction.

2.3.2 The Ionospheric D and E layer

The ionospheric D layer is located between 60 and 85 km. In this layer, ionisation by solar ultraviolet radiation replaces galactic cosmic ray ionisation as the main method of ion production with an efficiency which increases with height. Ionisation results mostly from photoionisation by Lyman α radiation (121.6 nm) and

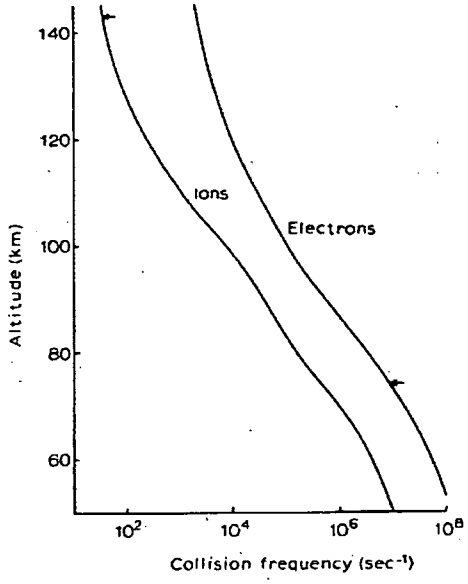

Figure 2.11: Typical collision frequencies versus altitude for ions and electrons. Arrows indicate the approximate gyrofrequencies for electrons and oxygen molecules of unit charge [Verniani, 1974].

X-ray radiation ($\lambda < 1$ nm) [Davies, 1990]. Ionisation due to energetic aurora electron precipitation and sporadic meteor effects also contribute to the ionisation of O_2 and N_2, particularly at night [McCormac, 1974]. The E layer extends from about 85 km to 130 km. It is produced by ionisation of molecular and atomic oxygen, and molecular nitrogen by X-ray radiation, by Lyman β radiation and by ultraviolet radiation in the Lyman continuum (91 to 98 nm) [Davies, 1990]. Other ionisation processes which contribute to the production of ions and electrons in the E layer include: ionisation due to energetic aurora electron precipitation, EUV radiation and auroral x-ray bremsstrahlung radiation during geomagnetic storms and proton bombardment during solar proton events.

Collisions between electrons, ions and neutral particles occur frequently and the mobilities of the ions and electrons are controlled by these collisions. Free electrons start to become significant as the main charge carriers and their higher mobility causes a rapid increase in the conductivity. The electron concentration is greatest at local noon. At night the electrons disappear almost entirely in the

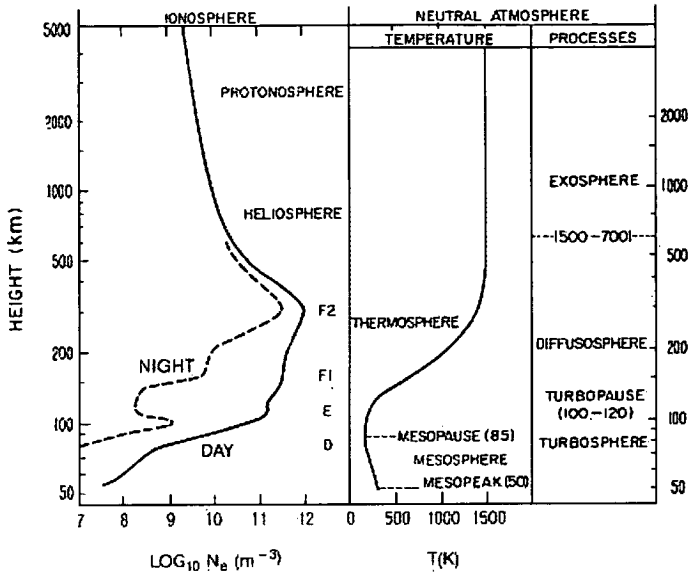

Figure 2.12: Atmosphere division by temperature and dynamics. The approximate altitude regimes of the different regions of the atmosphere are shown [Davies, 1990].

D layer and are reduced in the E and F layers (see figure 2.12). The numbers of neutrals in the D and E regions decrease at an exponential rate with altitude with an exponential scale height of about 6 km. The mobilities of ions and electrons and hence the conductivity of the atmosphere increases at a similar rate. Figure 2.13 shows the conductivity profile of the atmosphere and the ionosphere. Near the surface the conductivity is of the order of 10^{-14} siemens/m, large enough to dissipate any electric field within 40 minutes. At 100 km altitude, the conductivity is $\sim 10^{-3}$ siemens/m [Bering et al., 1998].

In the D and E layer, as well as the lower reaches of the F_1 layer, the collision frequency between ions and neutrals is sufficiently high that the plasma motion is determined by the motion of the neutral particles [Davies, 1990]. Differential heating of the atmosphere by the sun creates tidal wind systems that interact with the ionospheric plasma above 80 km altitude. Collisions between neutrals and electrons become less important and the electrons start to gyrate along the

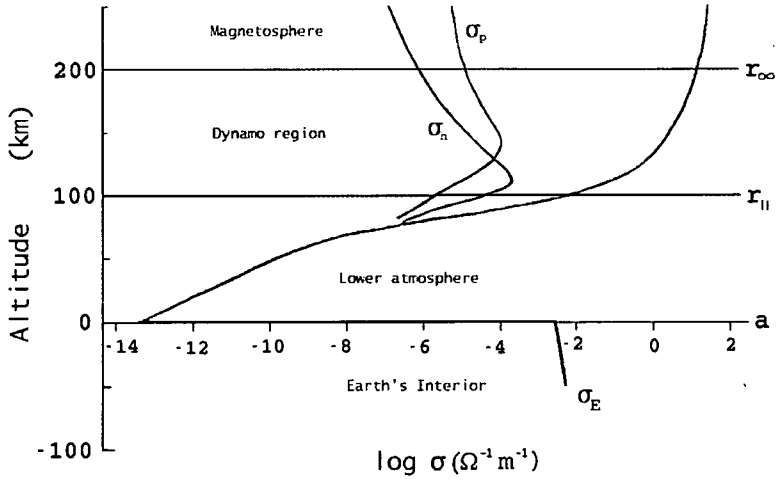

Figure 2.13: Altitude variation of the electrical conductivity in the Earth's atmosphere and ionosphere from the ground to 200 km altitude. The conductivity within the Earth is shown for comparison [Roble and Tzur, 1986].

geomagnetic field lines. The electron gyrofrequency is greater than the electron-neutral collision frequency and thus the mobility of electrons is governed by the geomagnetic field. Ions are not restricted by the magnetic field lines until about 140 km altitude, up until that height the ions essentially move with the neutral wind.

The conductivity parallel to the magnetic lines of force, $\sigma_{||}$, increases strongly with height. The differential motion of the ions and electrons within this dynamo region (100 km to 200 km altitude) causes instabilities to occur in the plasma, the conductivity to be anisotropic and a horizontal electric current to be generated across the polar caps [Roble and Tzur, 1986]. The effect of imposing a vertical electric field perpendicular to the geomagnetic field causes the ions and electrons to experience both a drift parallel to the electric field and orthogonal to the magnetic field and a drift orthogonal to both electric and magnetic fields. The conductivity of the atmosphere along these vectors are called the Pedersen and Hall conductivities respectively. Figure 2.13 shows the variation of $\sigma_{||}$, σ_p and σ_h with height. The Pedersen conductivity, σ_p, is reduced compared to $\sigma_{||}$

and maximises near 140 km, where the ion-neutral collision rate is equal to the gyrofrequency of the ions. It is carried mainly by electrons below 140 km and by ions above this height where it decreases proportionately with the mean density. The Hall conductivity, σ_h, is maintained primarily by the electrons [Roble and Tzur, 1986]. Positive and negative particles drift in the same direction and at the same speed. The difference in the mobilities of these particles leads to a finite value of the Hall conductivity which maximises near 110 km altitude and decreases with height more rapidly than σ_p. Above 200 km, the Pedersen and Hall conductivities are reduced by 90% of their maximum values. Both conductivities are subject to large diurnal, seasonal, and latitudinal variations due to the varying electron number density. At night, the magnitudes of the conductivities may drop by a factor of $\sim 10^{-1}$. X-rays from solar flares which penetrate into the ionospheric D and E layers temporarily shift the lower boundary of the dynamo region to lower altitudes.

2.3.3 F layer

The F layer is situated at the base of the magnetosphere, at an altitude range of $\sim 140 - 1000$ km. It consists of two layers, F_1 and F_2, during the daytime and one layer at night, when it is referred to simply as the F layer. The F_1 layer is located from about 140 km to 250 km altitude and the F_2 layer begins at about 250 km (see figure 2.6) [McCormac, 1974]. The main ionization process in the F_1 and F_2 layers is ionization of atomic oxygen and molecular nitrogen by solar extreme ultraviolet radiation (EUV) in the Lyman continuum. Ionisation due to UV and x-ray radiation and auroral electron precipitation continue to contribute to the ion-production rate. Electron densities maximise in the F_2 layer, decreasing rapidly above this altitude (see figure 2.12). The EUV radiation undergoes large day to day variations as well as periodic 27-day solar rotation and solar-cycle variations [Roble and Tzur, 1986]. Solar flare events enhance the EUV and x-ray radiation, causing an increase in the electrical conductivity.

At high latitudes, processes other than solar illumination have a role in de-

termining the diurnal variations of the ionosphere. One important factor is the upward electromagnetic ($\mathbf{E} \times \mathbf{B}$) convection of ionisation from lower daylit latitudes toward the nightside [Davies, 1990]. This 'evening uplift' is called the Fountain effect. It is an equatorial phenomenon, caused by the west-to-east electric field generated in the E region of the ionosphere [Davies, 1990]. In general, the Fountain effect also causes the height of the F_2 peak to fall at dawn and rise during the afternoon or evening, especially at low latitudes.

The plasma motion in the F_1 layer is still determined by the neutral wind motions because the collision frequency of ions and neutrals is sufficiently high. The electrons are tied to the magnetic field lines but the ions are still free to move. In the F_2 layer, however, the collision frequency is relatively low and the ions are tied to the Earth's magnetic field. The plasma in this layer is essentially collisionless and hydromagnetic.

Above the F layer, helium and hydrogen ions dominate. The motion of these particles is influenced by the Earth's magnetic field and the particles tend to gyrate along the magnetic field lines [Brasseur and Solomon, 1986].

2.4 Generators and Sources of the Global Electric circuit

A downward electric field of between 100 and 200 Vm^{-1} can be detected near the surface in fair-weather regions of the Earth. A time-varying potential difference of the order of 250 kV, directed downwards, is maintained between the ionosphere and the ground. This capacitor discharges through the atmosphere with an average current of $\sim$ 1 kA integrated over the Earth. The global electric circuit is driven by three quasi-DC sources of electromotive force: thunderstorms, a dynamo interaction between the solar wind and the magnetosphere, and the dynamo effect of atmospheric tides in the thermosphere; the last possibility is not discussed here. It is widely believed that thunderstorms are the dominant power source, however, direct conclusive evidence of this fact has been difficult

to obtain [Reiter, 1992].

2.4.1 Thunderstorms

Thunderstorms interact electrically with the upper atmosphere and ionosphere. Thunderstorm (cumulonimbus) clouds are essentially vertical electric dipoles. The positive and negative charges in the cloud are separated by the intense updrafts and downdrafts occuring in the cloud. Positive charges are carried upwards and negative charges are left at the bottom of the cloud. Electric currents flow between these charged regions as well as to the ground via cloud-to-ground lightning strikes, falling precipitation (rain and hail) and via the Wilson currents flowing upwards from the cloud tops. Wilson currents flow through the ionosphere and through the magnetosphere, along the magnetic field lines to the opposite hemisphere, to return to the ground as the fair weather air-Earth current [Bering et al., 1998] (see figure 2.14).

The conductivity of the air plays an important role in the electrical behaviour of thunderstorm clouds. At the top of a thunderstorm cloud, at an altitude of about 10 km, the conductivity is approximately ten times greater than at the Earth's surface [Bering et al., 1998]. At the bottom of the cloud ($\sim$ 5 km altitude) the negative charges are contained within the cloud and the conductivity is decreased relative to the clear air due to the presence of large cloud particles. The columnar resistance is much greater in the lower 10 km of the atmosphere. Bering et al. [1998] estimates the resistance from the ground to a height of 10 km of a cylinder of clear air with a radius of 20 km to be about 400 MΩ. In cloudy air, the columnar resistance increases dramatically to several GΩ. For a cylinder of air of the same radius, reaching from 10 km altitude up to the ionosphere, the resistance is only about 40 MΩ (see figure 2.15).

Active thunderstorm clouds contain an enormous amount of energy built up by the circulating air within the cloud [Cotton and Anthes, 1989]. Figure 2.16 depicts the circulation of air in a thunderstorm cloud. Fast moving updrafts are surrounded by violent downdrafts, bringing rain to the surrounding area below the

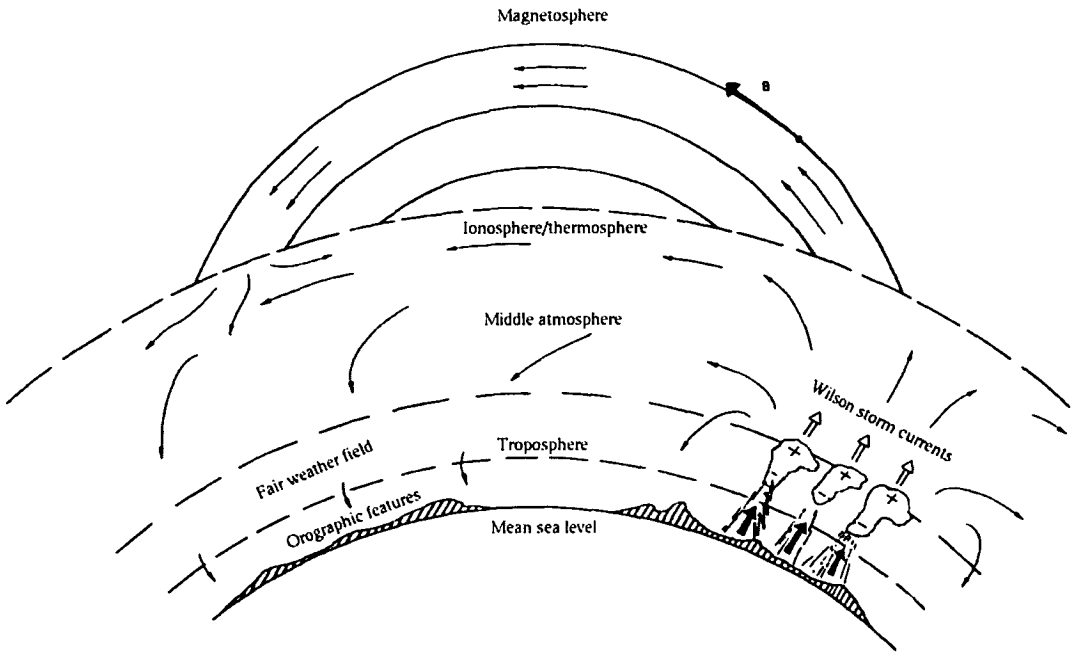

Figure 2.14: Schematic of the various electrical proccesses in the global electric circuit. All the unlabelled arrows represent current flow in the circuit. The strongest generator in the circuit, thunderstorms, are indicated on the right. Thunderstorms produce Wilson currents, which flow up into the ionosphere and spread out around the globe [Hays and Roble, 1979].

cloud. Small cloud particles, which carry a net positive charge, are transported upwards by the strong updrafts. As the mass of a particle increases, its upwards motion ceases and the particle begins to fall relative to the Earth and the surrouding updrafts. These heavier particles carry a net negative charge. The drag on the air created by the falling precipitation particles induces a downdraft which flows out the bottom of the cloud and spreads out across the surface. The downdrafts can be quite violent and may bring heavy rainfall or hail and strong gusts of wind to the underlying regions. The massive build up of static charge created by the updrafts and downdrafts is eventually released from the cloud via lightning strikes; negative cloud-to-ground and on rare occasions, positive cloud-to-ground, cloud-to-cloud, or intra-cloud lightning strikes, quasi-DC point discharge currents

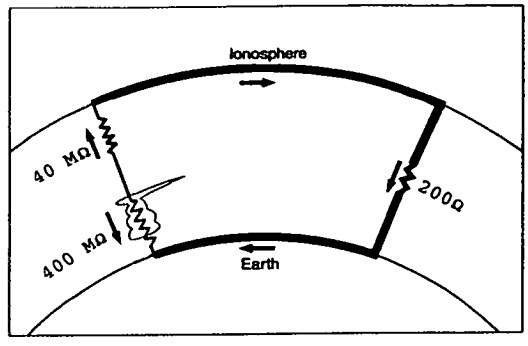

Figure 2.15: Diagram of the global electric circuit with estimates of the resistances in the system. Diagram based on one by Rycroft et al. [2000].

such as St Elmo's fire, conduction current, and negatively-charged precipitation.

The vast majority of lightning activity occurs over the continental regions of the Earth. Lightning is rarely seen over the oceans because of the significant difference in updraft intensities found in oceanic and continental thunderstorm clouds [Rycroft et al., 2000]. This difference in updraft intensities is attributed to small differences in surface temperature over land and over the sea [Williams, 1992]; air near the ground is strongly heated and becomes buoyant and thus unstable. The same sort of heating does not occur over the ocean, with its more conservative temperature range. The electrification of thunderclouds is controlled by departures from hydrostatic equilibrium caused by small temperature changes and by buoyancy, which is in turn dependent on the surface air temperature.

There are three main regions of lightning activity: Asia and Australia, Africa and Europe, and America [Roble and Tzur, 1986]. Figure 2.17 shows the distribution of lightning activity over the earth as recorded by the Optical Transient Detector (OTD) during 1998. Since the majority of the landmass is located in the northern hemisphere, more thunderstorms occur in that region of the world resulting in a maximum in global lightning activity during the northern hemisphere summer (June to August). Figure 2.18 shows the lightning activity of figure 2.17 split into each of the seasons.

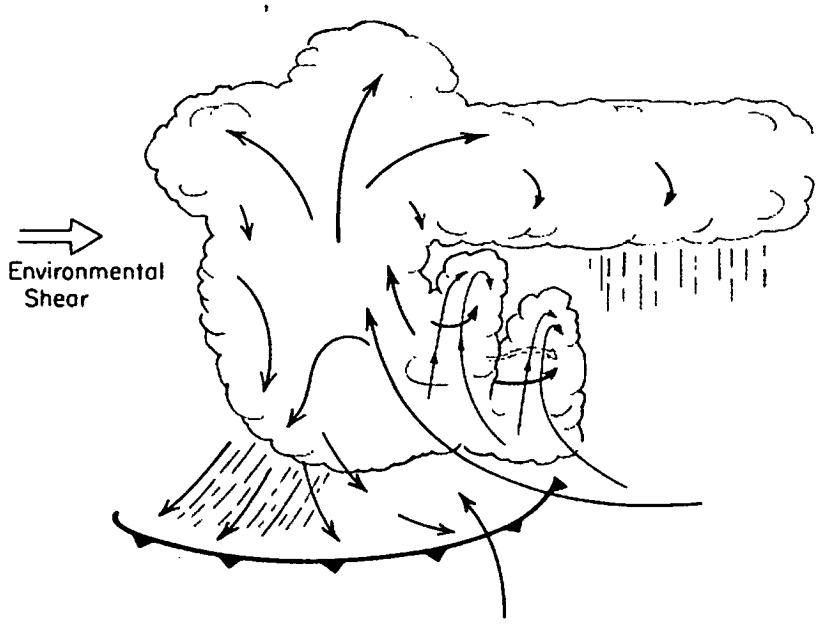

Figure 2.16: The motion of the updrafts and downdrafts in a cumulonimbus cloud. These clouds extend from the lower layers of the atmosphere to the top of the troposphere. Typically, cumulonimbus clouds have a flat top which is surrounded by curving sides, resembling an anvil. The anvil shape is created by the divergence of the updrafts just below the tropopause and by the temperature of the atmosphere which, in the troposphere, tends to decrease with height [Cotton and Anthes, 1989].

The global thunderstorm rate is not constant but varies across the day according to the irregular distribution of the continents. Daily lightning activity in the tropics maximises in the late afternoon (16-18 hours local time). Over the entire globe, this produces a diurnal variation of global thunderstorm activity with maxima at 0800, 1400 and 2000 UT, corresponding to the longitudinal distribution of the three main regions of lightning activity, Asia/Australia, Africa/Europe and America. The curve exhibits a general similarity to that of the diurnal electric field curve (see top figure of figure 2.19) which has a minimum at 0400 UT and a maximum between 1800 and 2100 UT, depending on the season.

The mean thunderstorm probability as a function of time was determined by Whipple and Scrase in 1936 [Reiter, 1992]. They used corona current record-

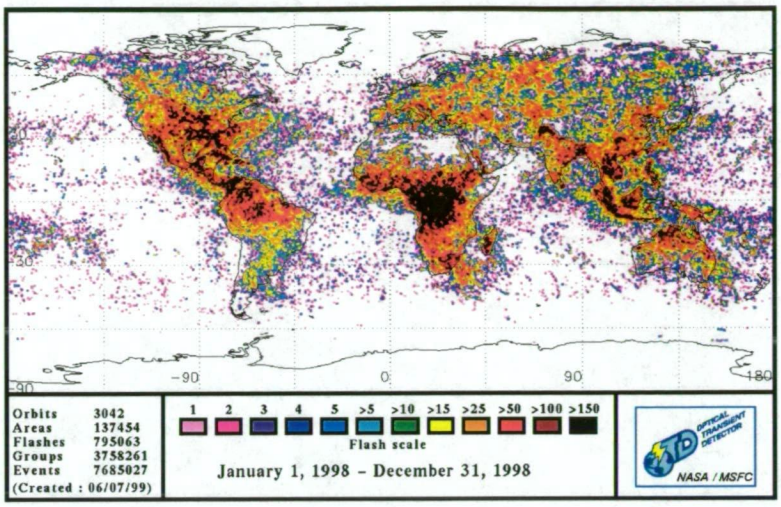

Figure 2.17: Lightning activity during 1998 as recorded by NASA's Optical Transient Detector.

ings and assumed that the same probability distribution existed on all other continents. Whipple and Scrase combined their results with the world thunderstorm statistics acquired by Brooks to obtain the diurnal variation of global thunderstorm activity (bold line in figure 2.19) and provided the first experimental evidence of Wilson's thunderstorm generator hypothesis [Reiter, 1992]. The thunderstorm diurnal curve published by Whipple and Scrase is still used today although there are uncertainties regarding the accuracy of the data [Reiter, 1992]; thunderstorm observations were highly subjective in nature and the accurate counting of lightning strikes, especially in regions of high thunderstorm activity, was nearly impossible, thunderstorms occuring over the oceans far from the coasts are mostly unobservable and their frequency dependent on their geographical location. Whipple's assumption of a globally uniform background lightning strike rate has since been shown to be incorrect. Recent satellite studies have shown that lightning strikes occuring over the oceans account for less than 10% of the total number occuring over land [Bering, 1995].

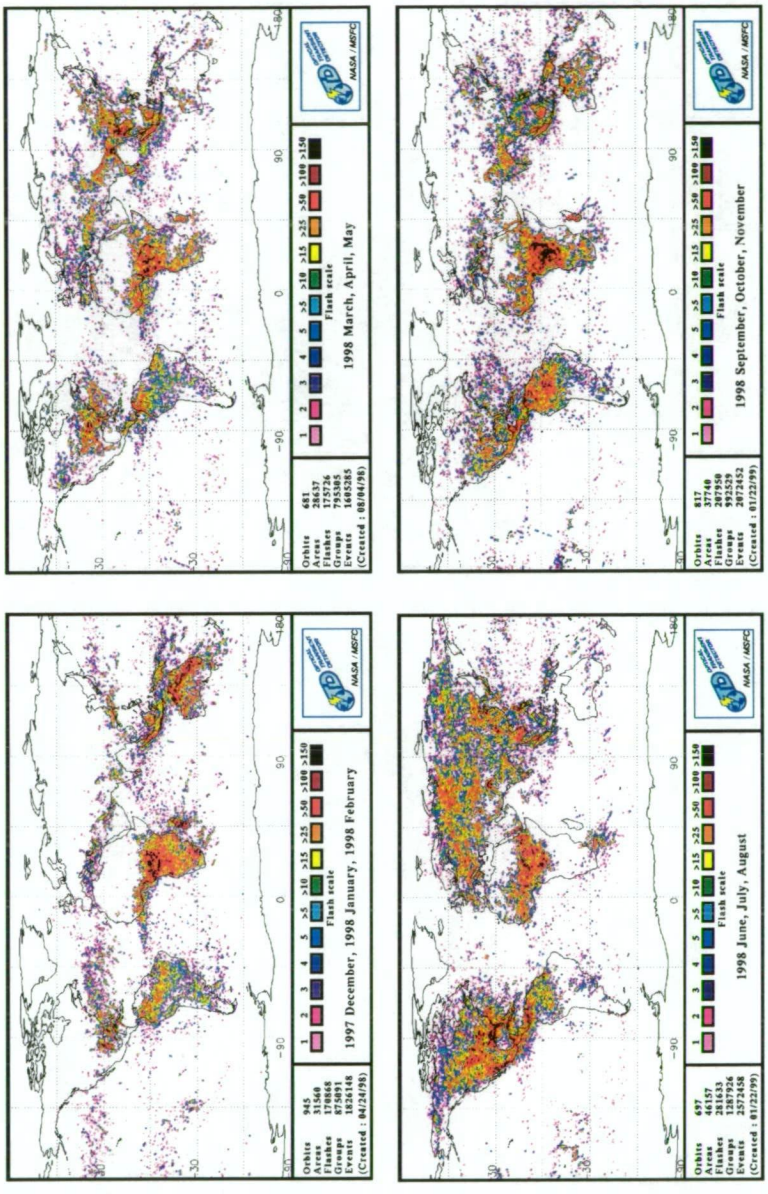

Figure 2.18: Lightning activity during the southern hemisphere summer, autumn, winter and spring of 1998 as recorded by NASA's Optical Transient Detector. Lightning activity is greatest during the Northern Hemisphere summer (June to August) because of the greater proportion of landmass in the Northern Hemisphere.

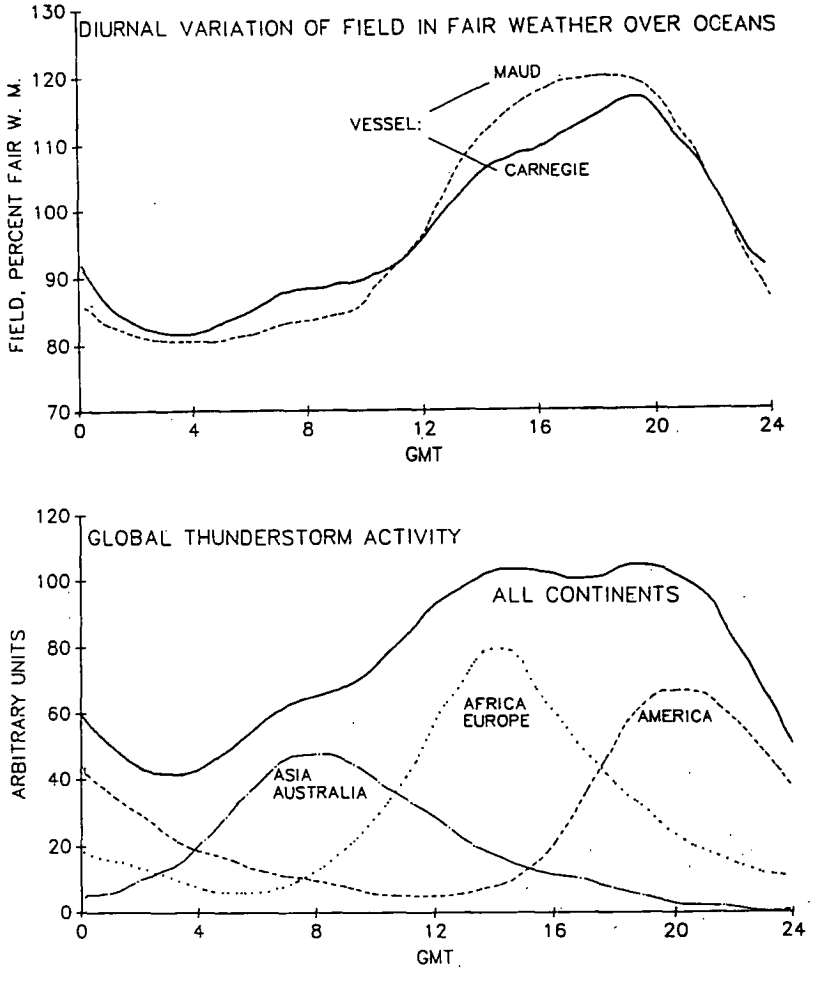

Figure 2.19: Diurnal variations of the average potential difference measured by the research vessels *Carnegie* and *Maud* during fair weather and global thunderstorm activity as estimated by Whipple in 1929, using audible thunder and meteorological observations from around the world [Reiter, 1992].

Red Sprites, elves, blue jets, and other transient phenomena

Thunderstorms interact electrically with the upper atmoshere and ionosphere producing transient optical and radio wave phenomena. The first of these optical phenomena to be discovered were red sprites. Other optical and radio wave phenomena have since been found; elves, blue jets, transionospheric pulse pairs (TIPPS), X-ray and gamma ray flashes.

Red sprites are optical emissions observed in the mesosphere above thunderstorms lasting between about 5 to 300 ms. They can exist as single elements but are generally composed of sets of columns, with each column showing a large number of fine structures at the top or bottom of the sprite, described as 'hair' or 'tendrils' [Rodger, 1999]. Sprites are predominantly red in colour due to the excitation of a set of bands of neutral N_2 molecules. The lower tendrils change colour, with decreasing altitude, from red through to purple and blue. Figure 2.20 shows the three different appearances of sprites. The first type are plumes which are red in colour and visible to the naked eye. The second shows columns of different lengths which can overlap creating the appearance of a continuous diffuse curtain of light [Rodger, 1999]. The third type of sprite has the appearance of a jellyfish with a broad quasi-circular head with fine tendrils below. There is no commonly agreed type of red sprite. They can have spritelets and tendrils that are not vertically oriented and can be bent with respect to other structures present and appear to diverge from a common point in the clouds [Rodger, 1999]. Red sprites tend to occur after large-amplitude, positive cloud-to-ground lighting strikes, but can occur anywhere within 50km of the lightning strike. Positive cloud-to-ground lightning discharges account for about 10% of all cloud-to-ground lightning strikes. The rate of occurence ranges from 50% down to 2% of positive cloud-to-ground discharges.

A number of theories have been presented in an attempt to explain the existence of red sprites. All involve lightning discharges "acting either as a causative agent or as a simultaneous but noncausative consequence of electical breakdown triggered by cosmic rays" [Sentman and Wescott, 1996]. The main mechanisms

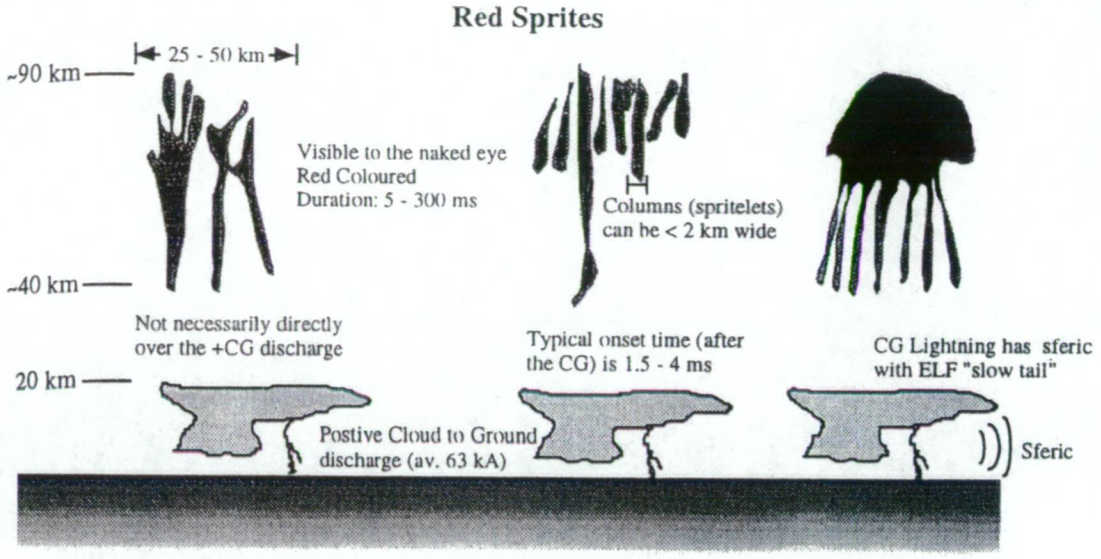

Figure 2.20: Schematic of red sprite events. A number of sprite forms are shown; (from left to right) plumes, columns of different lengths and a "jelly fish" sprite [Rodger, 1999]

proposed are the fluorescence or luminescence of the atmosphere, lightning electromagnetic pulse (EMP), thunderstorm quasi-electrostatic fields, and cosmic-ray triggered runaway breakdown [Rodger, 1999].

Elves (Emissions of Light and VLF pertubations due to EMP Sources) are transient luminous events, occuring briefly in the lower ionosphere ($75 - 105$ km altitude) just after the onset of cloud-to-ground lightning discharges. Elves last for < 1 ms duration, have quite high intensities (> 1 MR) [Inan et al., 1997] and have a horizontal scale width of 100 to 300 km. Elves have been described as diffuse optical flashes consisting of pancake shaped layers or rings of light which expand and dissipate rapidly. Red sprites sometimes appear a few milliseconds after an elve, approximately in the centre of the region where the elve was observed [Rodger, 1999]. Elves are believed to results from electromagnetic pulses (EMP) produced by lightning discharges. The electromagnetic pulse propagates up into the stratosphere and mesosphere, producing large electric fields that emit a ring of light at the base of the ionosphere. As the EMP propagates away from the lightning source, the ring of light expands outwards [Rycroft et al.,

2000]. ELF/VLF radio studies of lightning flashes associated with sprites and elves have reported that elves are always accompanied by large amplitude VLF perturbations [Fukunishi et al., 1996].

Blue jets are sporadic optical emissions that erupt in narrow cones (about 15° full width) from small regions directly above the active core of the thundercloud and propagate upwards through the stratosphere. Blue jets extend to altitudes of $40 - 50$ km at vertical speeds of $75 - 220$ km s^{-1} over a lifetime of about 300 ms [Rodger, 1999]. They are deep blue in colour and have an intensity of the order of 500 kR at the base decreasing to about 7 kR at the top [Rodger, 1999]. The jets are quasi-vertical and are not aligned with the geomagnetic field. Although blue jets occur above thunderclouds, no clear association with lightning discharges have been reported. However, Wescott et al. [1995] did make the observation that blue jets were "often observed to follow upward lightning strokes". There is no currently accepted theory which explains the occurrence of blue jets.

Transionospheric pulse pairs (TiPPs) or extremely intense pairs of VHF pulses are satellite-observed radio noise bursts with a duration of approximately 10 μs. They typically occur in pairs with a separation of $10 - 110$ μs between the pulses. Some TiPPs have been shown to be associated with lightning activity and observations of TiPPs show that their global distribution is similar to that of lightning flashes [Zuelsdorf et al., 1997]. Strong correlations between TiPPs and positive intracloud and intercloud lightning discharges have been reported for some TiPPs, however, there have been a larger number of TiPPs observed which are not correlated with positive intercloud lightning discharges [Rodger, 1999].

X-ray and terrestrial gamma ray (TGR) events are thought to be associated with lightning activity and its associated effects (eg. red sprites). X-ray bursts with energies of 2 to > 110 keV were observed inside thunderstorms. The bursts were seen to occur several seconds before a lightning flash and then decrease immediately afterwards to background levels [Rodger, 1999]. It has been proposed that the X-ray bursts are produced by collision of ionised particles with neutral particles. The ionised particles are produced by acceleration of electrons

to sufficiently high energies by the strong electric fields contained within the thundercloud [Rodger, 1999]. Terrestrial gamma-ray flashes are short blasts of gamma-ray energy associated with thunderstorms. The radiated energy is significantly higher than that of large solar flares or cosmic gamma-ray bursts [Fishman et al., 1994]. Terrestrial gamma ray events are thought to be associated with red sprites and other high-altitude phenomena and observations have shown that some gamma ray flashes are associated with a "slow-tailed" positive cloud-to-ground sferic consistent with red sprite occurrences [Rodger, 1999]. Evidence for the association of TGRs and high altitude effects of thunderstorms is somewhat circumstantial and there has been no universally accepted theory for TGRs.

Schumann Resonances

Schumann resonances are global electromagnetic phenomena that are driven by worldwide lightning activity. Lightning activity, which is linked with cloud electrification and the accumulation of ice particles in the upper troposphere, responds sensitively to subtle temperature variations at tropical sites, suggesting a global response [Williams, 1992]. The global electric circuit may thus provide a natural global thermometer in the form of Schumann resonances.

Schumann resonances are excitations of the AC component of the global circuit, resulting from the interference of propagating waves within the Earth's atmosphere. The neutral atmosphere between the Earth's surface and the ionosphere behaves like a waveguide when excited by extremely low frequency (ELF) electromagnetic radiation from lightning strikes. At low frequencies, from 5 to 50 Hz, the radio waves propagate several times around the globe before disspating. Contructive interference produces standing resonant waves; Schumann resonances [Rycroft et al., 2000]. The fundamental resonance is approximately 8 Hz and the harmonics are given by

$$f_n = f_1\left[\frac{n(n+1)}{2}\right]^{\frac{1}{2}}, \tag{2.2}$$

at approximately $14, 20, 26, 33, \ldots$ Hz.

Schumann resonances are not influenced by changes in the local conductivity

and are dependent only on global lightning activity. Variation in the background Schumann resonance intensities reflect those of temperature over long time scales; from months to years [Williams, 1992]. Figure 2.21 shows the monthly variations of tropical surface air termperature and the mean magnetic field for the fundamental mode of Schumann resonances. Variation of Schumann resonance intensities is shown to closely follow that of monthly tropical temperature intensities. Schumann resonances are linked to temperature variations via lightning flash rates and provide an ideal way to study the global variability of lightning activity [Rycroft et al., 2000]. The AC component of the global circuit is better correlated with global lightning activity than the DC component, which is influenced by changes in the conductivity of the atmosphere. Like the DC measurements of the geoelectric field, Schumann resonance can be monitored from a single position on the Earth's surface. Transient Schumann resonance signals have also been shown to be well correlated with sprite activity and hence could also be used to study sprites on a global scale [Rycroft et al., 2000].

2.4.2 Solar Wind Modulation of the Global Electric Circuit

The interaction of the solar wind and the Interplanetary Magnetic Field (IMF) with the Earth's magnetopause generates a horizontal dawn-to-dusk potential drop of $20 - 150$ kV across the polar caps and auroral currents of the order of 10^6 A in the polar regions. The solar wind and IMF control the shape of the Earth's magnetosphere as well as the location of the magnetopause.

Variations in the solar wind influence the global electric circuit. The solar wind modulates the flow of galactic cosmic rays, the precipitation of relativistic electrons from the magnetosphere and changes the ionospheric potential distribution in the polar caps via interactions with the Earth's magnetosphere. Solar influences on the global electric circuit vary temporally and spatially. An overview of each of these processes is provided here; more detailed descriptions are provided

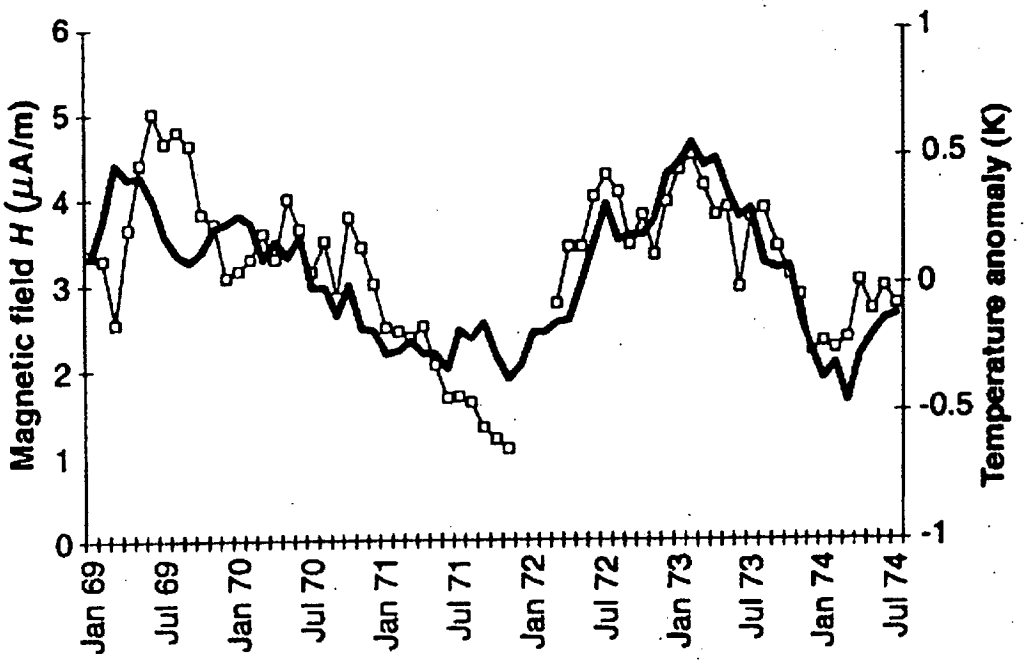

Figure 2.21: Variation of the monthly mean maximum wet-bulb tropical surface air temperature for 1989 (heavy line) and the monthly mean magnetic field for the fundamental mode (8 Hz) of Schumann resonance in Kingston, Rhode Island (light line) [Williams, 1992].

by Tinsley [2000].

Theory

The ionosphere and the surface of the Earth are effectively equipotential surfaces except within the polar regions. The influence of the solar wind at these high latitudes is several times stronger than at lower latitudes. Auroral currents of several million amperes, flowing through the polar cap ionospheric regions result in changes ($\sim$ 50 kV) in the ionospheric potential difference. Figure 2.22(a) is a schematic diagram of the global electric circuit. It shows the current flows generated by tropical thunderstorms and the possible influences of the solar wind.

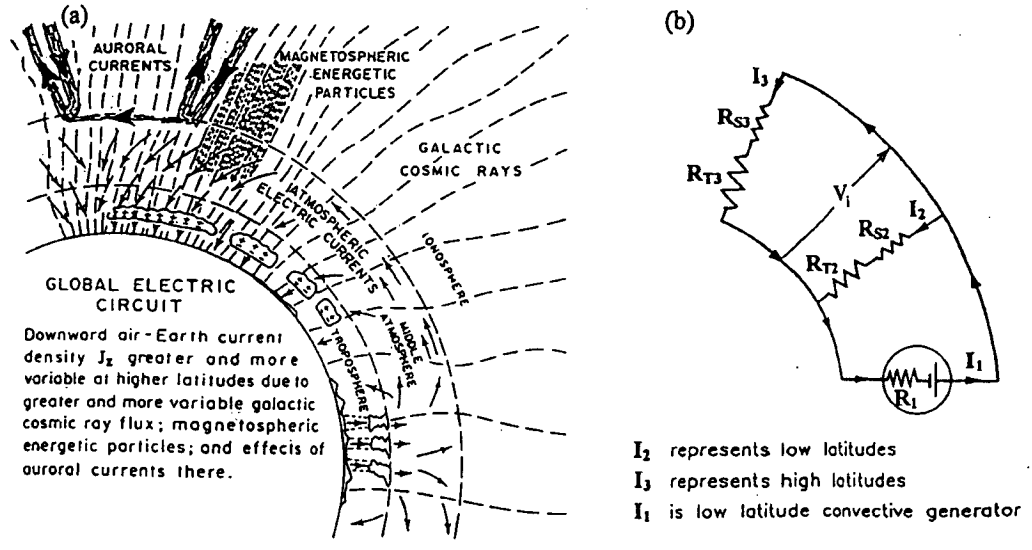

Figure 2.22: Representations of the global atmospheric electric circuit. (a) A diagram of part of a meridional section, with arrows representing the current density glow generated by tropical thunderstorms. (b) An equivalent circuit for the global circuit with the only horizontal variation due to magnetic latitude. The ionosphere-earth current is divided into a low-latitude branch and a high-latitude branch. The high-latitude branch is greatly affected by variations in the solar wind [Tinsley and Heelis, 1993].

The global electric circuit is essentially a spherical shell capacitor. The potential difference between the ionosphere and the surface of the Earth, the top and bottom plates of the capacitor, gives rise to a vertical current density, J_Z, which is modulated by changes to the atmospheric conductivity, $\sigma(z)$, and/or the vertical component of the electric field, E_Z,

$$J_Z = \sigma(z)E_Z. \tag{2.3}$$

It may also be expressed in terms of the ionospheric potential difference, V_i,

$$V_i = J_Z \int \frac{1}{\sigma(z)} dz, \tag{2.4}$$

where z is the altitude and $\sigma(z)$ is the conductivity of the column of air which increases strongly with altitude in clear air [Tinsley et al., 1998]. For vertical

conductivity profile the potential gradient, E_Z, at any altitude varies linearly with overhead ionospheric potential [Tinsley et al., 1998].

The solar wind modulates the global electric field by varying the current density. J_Z is modulated by either varying the latitudinal distribution of $\sigma(z)$ in the troposphere and lower stratosphere or by varying ionospheric potential difference, V_i, especially in the polar regions.

Figure 2.22(b) shows an equivalent circuit for the global circuit, with the only horizontal variation due to a variation with magnetic latitude [Tinsley, 2000]. The return path is divided into two sections, one representing the low-latitude regions with an integrated return current, I_2 and the other representing high-latitude regions with an integrated return current, I_3, thus allowing the variation of the ratio of the currents through the return paths to be described. The columnar resistance is separated into tropospheric (R_T) and stratospheric (R_S) components. I_1 and R_1 represent the current and resistance of the low latitude generators, which in this case are tropical thunderstorms. The internal impedance, R_1, is much greater than the sum of the resistances of the two return paths, and so the current I_1 is believed to be essentially independent of the load and is equal to the sum of the currents in the two return paths, I_2 and I_3. The low latitude return path has a relatively constant inpedance compared to the high latitude path, which is highly responsive to solar wind influence. The latitude gradient, caused by the latitudinal variation of the conductivity of the atmosphere, controls the distribution of J_Z between the high and low latitude return paths.

Variations in Solar Irradiance

The radiative output of the Sun is not constant and varies over the 11 year solar cycle. Variation of the global surface temperature is closely associated with long term variation of solar activity [Friis-Christensen and Lassen, 1991]. Correlation of reconstructed solar irradiance and Northern Hemisphere surface temperature for the period 1610 to 1800 produced significant correlations [Lean et al., 1995], implying a predominant solar influence. Lean et al. [1995] theorised

that solar forcing may have contributed to about half of the observed 0.55°C surface warming observed from 1860 to 1990 and about one third of the surface warming between 1970 and 1990, hence suggesting that solar variability may be largely responsible for global temperature changes. Satellite measurements taken over 1 solar cycle show that the total solar irradiance is not constant and varies by $\sim 0.1\%$ over the 11 year solar cycle [Tinsley, 1997]. This 0.1% variation is too small to have a significant impact on day to day changes in the climate.

A second hypothesis, proposed to explain the apparent correlation between surface temperature and solar activity, involved variations in the solar ultraviolet (UV) flux. Solar UV irradiance contributes significantly to the total irradiance variations but is absorbed in the upper stratosphere. Variable UV irradiance may affect climate indirectly by affecting ozone production and hence the radiative and dynamical coupling of the stratosphere and the troposphere [Lean et al., 1995]. Changes in tropospheric dynamics are postulated via the intermediate process of changes in dynamics of the upper stratosphere [Tinsley and Deen, 1991]. It is generally accepted that the magnitude of the variations from this process cannot account for significant climate variations.

Galactic Cosmic Ray Flux Variations

Galactic cosmic rays are the main source of ionization in the stratosphere and troposphere and are modulated by variations in the solar wind plasma and irregularities in the solar wind magnetic field. Galactic cosmic ray flux in the lower atmosphere has the largest modulation through the solar cycle and variations occur over all time scales; from the order of a few days to a century [Tinsley et al., 1989]. Galactic cosmic ray flux variations change: the ion production rate (and hence the conductivity of the atmosphere); the rate of charge dependent chemical reactions; charge dependent droplet and crystal formation; and, the current flow in the global electric circuit.

Svensmark and Friis-Christensen [1997] observed that changes in oceanic cloud cover were correlated with changes in the galactic cosmic ray flux. They hypoth-

esised that changes in solar activity and geomagnetic field intensity may trigger changes in the Earth's climate by modulating the galactic cosmic ray flux penetrating into the atmosphere. Marsh and Svensmark [2000] provided evidence that supported this hypothesis but restricted the observed correlations to the mean global low cloud cover below an altitude of $\sim$ 3200 m. Several microphysical mechanisms were proposed by which galactic cosmic rays might influence cloud formation and air temperature. Dickinson (1975) speculated that galactic-cosmic-ray-induced ionisation near the tropopause might influence the formation of sulfate aerosol cloud condensation nuclei. Tinsley [2000] proposed a mechanism in which the galactic cosmic rays modulate the ionosphere-Earth current density flow in the global electric circuit and thus modulate the rate of ice nucleation.

Tinsley and Deen [1991] proposed a mechanism connecting atmospheric electricity with the rate of contact ice nucleation in clouds, which effects the rate of latent heat release, the vertical motions, atmospheric vorticity and atmospheric pressure.

There are two processes by which electrostatic charging of cloud droplets and aerosols will enhance the contact ice nucleation rate; an increase in collection efficiency for aerosols acting as ice nuclei by charged droplets and the effect of electrostatic charge on the physics of nucleation itself [Tinsley and Heelis, 1993].

Tinsley [2000] proposed that changes in the air-earth current density, due to solar wind modulations, affected the accumulation of electrostatic charge at the tops of clouds. He hypothesised the existence of a physical mechanism, relating the accumulation of charge at cloud tops to microphysical changes in clouds, which affected atmospheric dynamics and storm intensities. The accumulation of electrostatic charge on supercooled droplets and aerosols affects the probability of ice nucleation and droplet freezing, enhancing the rate of growth and sedimentation of ice crystals [Tinsley, 2000]. The effect of this on weather and climate is to reduce cloud opacity and albedo of light cloud, to intensify storm cloud systems through enhancement of precipitation rates and latent heat release.

Tinsley's model predicts that at solar maximum or low-energy galactic cosmic

ray minimum there is a global maximum in ionospheric potential, V, a maximum in air-earth current density, J_Z, at low latitudes and a minimum in J_Z at high latitudes. A reduced flux of lower energy galactic cosmic rays increases the impedance of the high latitude path and thus decreases the current, I_3, see Figure 2.22. The total current through the load, I_1, is isolated from the solar wind influence and remains constant. I_2 is thus increased to maintain the relation, $I_1 = I_2 + I_3$. The potential V_i is increased and the current density, J_Z, is re-distributed across the latitudes [Tinsley, 2000].

Precipitation of relativistic electrons from the magnetsosphere

Precipitation of relativistic electrons into the ionosphere affects the state of ionisation and the neutral composition of the atmosphere and produces electromagnetic radiation over a wide range of wavelengths. It is an important source of ionisation in the D region of the ionosphere and the x-ray Bremsstrahlung radiation produces ionisation down to 20 km. For higher flux rates, the ion production rate, down to 30 km, exceeds that due to galactic cosmic rays.

Studies have noted decreases in the fluxes of relativistic electrons following decreases in solar wind velocity starting a few days before the time of HCS (Heliospheric current sheet) crossings. Observed changes in the current density, J_Z and vertical electric field, E_Z, were found to also coincide with the passages of the HCS over the Earth. The mechanism behind this effect is generally believed to be due to changes in the fluxes of precipitating relativistic electrons in the sub-auroral region and not due to variations in galactic cosmic ray or to changes in geomagnetic activity [Tinsley and Heelis, 1993].

Ionospheric potential distribution in the polar caps

A potential difference of $20 - 150$ kV exists across the polar cap ionosphere. Although, the ionosphere and the surface of the Earth are considered to be highly conducting equipotentials, this assumption is only true at low latitudes. At high latitudes, the flow of auroral currents, generated by the dynamo interaction of the

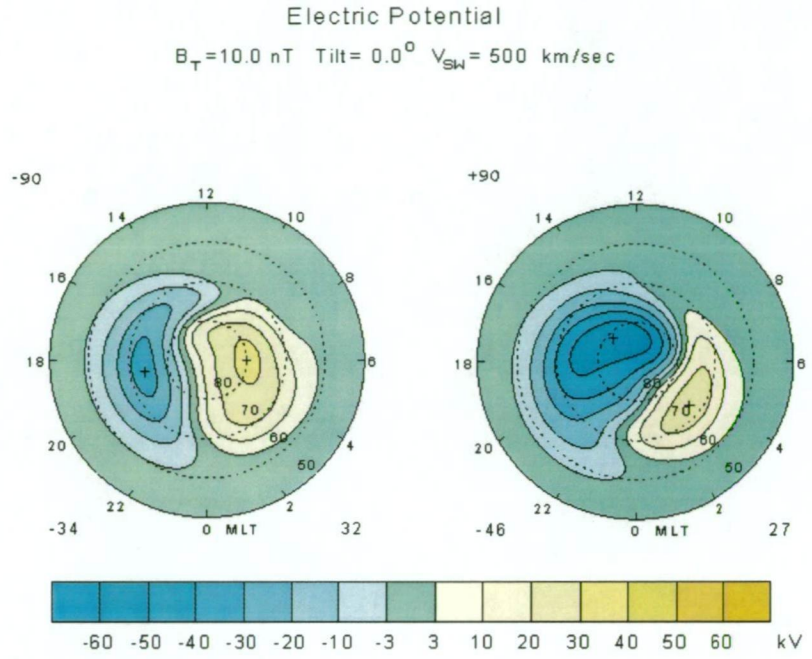

Figure 2.23: Electric potentials derived at IMF angles $-90°$ $(-Y)$ and $+90°$ $(+Y)$. The numbers at the lower left and right corners show the minimum and maximum potentials in units of kV [Weimer, 1996].

solar wind with the Earth's magnetosphere, through the polar cap ionospheric regions result in relatively large convection potentials superimposed on top of the low latitude potentials. These convection potentials vary with solar wind velocity and IMF magnitude and direction [Tinsley and Heelis, 1993]. Figure 2.23 shows the effect of changes in IMF B_y on the electric potential patterns near the geomagnetic pole. The magnetic field lines in the polar region can be regarded as equipotentials, because of the high electrical conductivity along the geomagnetic field lines. Any potential difference across the field lines in the magnetosphere is essentially mapped down to the lower edge of the ionosphere.

Large scale horizontal electric fields in the ionosphere map into the vertical component of the near surface electric field and the vertical electric fields should have the same dawn-to-dusk variation across the polar cap [Park, 1976a]. The

vertical electric field, E_Z, and by proxy J_Z, is thus proportional to the overhead ionospheric potential. Tinsley et al. [1998], using South Pole electric field data from 1982 to 1986, demonstrated that E_Z and the overhead ionospheric potential, V_i, were linearly correlated,

$$E_Z = C[\Phi(t) + \Psi(t)], \tag{2.5}$$

where the $\Phi + \Psi$, the sum of the low-latitude ionospheric potential for some time, t, and the ionospheric convection potential for some location and time, t, is the overhead ionospheric potential [Tinsley et al., 1998]. The constant ratio linking E_Z and V_i is given by

$$C = \frac{E_Z}{V_i}. \tag{2.6}$$

For the Vostok site, using $V_i = 250$ kV and $E_Z = 177$ Vm^{-1} gives a constant ratio of

$$C = \frac{E_Z}{V_i} = \frac{177}{250} = 0.71 \ Vm^{-1}/kV. \tag{2.7}$$

Chapter 3

Models of Ionospheric Electric Potentials

The interaction of the solar wind and IMF with the Earth's magnetosphere and ionosphere imposes an electrostatic potential field across the polar caps. The potential field generates current flows into and out of the polar ionospheres along the magnetic field lines, closing through ionospheric currents. A potential drop of between 20 and 150 kV exists across the polar cap ionosphere. The magnitude of the cross polar cap potential drop is influenced by the direction and magnitude of the z components of the IMF whereas the dawn-to-dusk distribution of the electrostatic equipotentials is influenced only by the direction of the y component [Rich and Hairston, 1994]. The ionospheric electric potentials mirror the potentials and plasma convection throughout the entire magnetosphere and convection maps of the electric potentials provide an insight into the physical processes occurring in the coupled solar wind-magnetosphere-ionosphere system.

There have been many attempts to produce ionospheric convection maps. Early electric potential models consisted of pictorial sketches, lacking in numerical representations and/or parameterisation [Papitashvili et al., 1999]. The models were limited in that they described the convection patterns for loosely-defined IMF conditions and were unable to reproduce the potential pattens at arbitrary times for given IMF values. Each successive model either improved or extended

upon previous models through the use of additional data or different analysis techniques. The various models consist of empirical models derived from satellite or radar observations [e.g. Heelis et al., 1982, Foster, 1983, Heppner and Maynard, 1987, Hairston and Heelis, 1990, Rich and Hairston, 1994, Weimer, 1995, 1996, 2001], ground-based magnetometer studies [e.g. Levitin et al., 1982, Friis-Christensen et al., 1985, Papitashvili et al., 1994, 1999] and theoretical approaches to modelling of high latitude convection patterns [e.g. Heelis et al., 1982].

Magnetospheric convection has been studied using satellite observations since the early 1960s. Satellites have accumulated large sets of convection velocity measurements [Ruohoniemi and Greenwald, 1996]. Ionospheric convection maps, derived by statistical analysis of data collected by polar-orbiting satellites, are organised by IMF magnitude and orientation, season and dipole tilt. The electrostatic potentials are determined as a function of satellite position by integrating the electric field component along the motion of the satellite. The most recent and detailed models derived using satellite observations are those by Weimer [1995, 1996, 2001] who used the technique of spherical harmonic expansion to represent the electrostatic potential and linear regression techniques to determine the spherical harmonic coefficients instead of averaging in latitude-MLT bins.

Some models utilise direct radar observations of convection velocities. They have shown general associations between polar cap convection and IMF orientation and geomagnetic activity but are not as detailed nor provide the same level of coverage as the satellite-based models [Ruohoniemi and Greenwald, 1996].

In this chapter, the Weimer [1996] and the IZMEM [Papitashvili et al., 1994] models, which are used to calculate the ionospheric potential patterns above Vostok, are presented. The advantages and disadvantages of the different statistical techniques used to derive the models are discussed as well as the subsequent improvements. These two models were chosen to compare and contrast the use of satellite-based and ground-based data as well as the different techniques used to derive the models.

3.1 Weimer Model

The Weimer [1996] model calculates the electric potential patterns for any arbitrary combination of the IMF B_z and B_y magnitudes, solar wind velocity and dipole tilt angle. The model is an improvement on an earlier model [Weimer, 1995] which derived electric potential maps for only a few discrete combinations of IMF magnitude, angle and season. The Weimer [1996] model utilises a new technique of using a least error fit of spherical harmonic coefficients with data from a finite number of statistical patterns in an algorithm which is capable of calculating the electric potential pattern for any IMF value [Weimer, 2001]. Inputs to the model are the magnetic latitude of the site, magnetic local time, time (year, month, day, hour, minute, second), IMF B_z and B_y (but not B_x) magnitudes and solar wind velocity. The effects of IMF B_x variations have been predicted to be minor compared to IMF B_z and B_y effects.

The Weimer model uses electric field data from the Dynamics Explorer 2 (DE 2) satellite in combination with solar wind and IMF measurements from the IMP 8 and ISEE 3 satellites. The satellite data were matched with IMF measurements by calculating 40-minute IMF averages, beginning 30 minutes before the start of each DE 2 polar pass. Satellite passes were sorted into 26 separate groups according to the IMF magnitude, dipole tilt and solar wind velocity. The groups were not exclusive but contained overlapping passes. The number of satellite passes available was limited and thus the groups were not sorted by all three parameters at the same time, only one or two [Weimer, 1996]. The electric potentials were derived by an integration of the electric field component in the direction of motion and represented using a spherical harmonic expansion [Weimer, 1996]

$$\Phi(\theta,\phi) = \sum_{l=0}^{8} \sum_{m=0}^{Min(1,3)} (A_{lm}\cos m\phi + B_{lm}\sin m\phi) P_l^m(\cos\theta), \qquad (3.1)$$

where φ is the MLT angle, θ is a function of the CGM colatitude and P_l^m is the associated Legendre function. The spherical harmonic coefficients, A_{lm} and B_{lm}, are determined at sixteen different 'clock angles' by a least error fit. The variation of A_{lm} and B_{lm} is smooth and periodic with respect to the angle of the

IMF vector in the Y-Z plane and can be represented as a combination of Fourier series for the harmonic coefficients. Multiple linear regression can be used to determine how each Fourier coefficient varies with IMF magnitude, dipole tilt angle and solar wind velocity (see Weimer [1996] for details). The resulting linear regression coefficients are capable of producing potential maps for any reasonable combination of IMF magnitude and orientation, solar wind velocity and dipole tilt angle.

As the Weimer model is derived from actual electric field measurements (rather than ground-based magnetometer data and assumed ionospheric conductivities) it is expected to provide better predictions of the potential patterns on the night-side of the polar cap where the conductivity is low. The inclusion of the dipole tilt angle allows the model to set the angle that the Earth's magnetic field makes to the solar wind presure. The orientation of the Earth's magnetic axis, and hence the location of the major magnetospheric current systems, with respect to the Sun-Earth line varies with time because of both the Earth's diurnal rotation and its yearly orbital motion around the Sun. The use of a solar wind velocity input parameter implies that the Weimer model can make some allowances for solar wind viscosity influences on polar cap convection. The spherical harmonic coefficients are determined by a least error fit as opposed to averaging in latitude-MLT bins.

The plasma convection and potential near midnight have been shown to be influenced by substorm activity in the magnetotail [Weimer, 1999]. The Weimer model cannot make detailed forecast of processes associated with the nightside and does not allow for the influence of magnetospheric substorms. The model uses 40-minute averages of the IMF variables, however, ionospheric convection has been reported to respond over shorter periods (3 to 26 minutes) to IMF variations [Ridley et al., 1998]. The convection can begin to reconfigure throughout the ionosphere almost immediately after the arrival of the signal from the IMF.

3.2 The IZMIRAN electrodynamic model

The IZMIRAN electrodynamic model (IZMEM) [Papitashvili et al., 1994] describes the ionospheric convection patterns as a function of IMF magnitude and direction. It was developed from ground-based magnetometer data obtained in both northern and southern polar regions and represents a regression mapping of ionspheric electrodynamics. Inputs to IZMEM are time (year, month, day, hour, minute), IMF $|B|$, B_z, B_y and B_x. The model was developed to model large-scale, quasi-steady events but can be applied to time-varying phenomena with a proper time delay between the IMF data and ground observations.

The IZMEM model uses ground-based geomagnetic field variations as input data for the derivation of an ionospheric electric potential model. The magnetometer data were obtained from 21 magnetic observatories and autonomous magnetometers located across Antarctica during 1978-1980 and 1983-1984. Regression analysis techniques were used to relate variations in the magnetic field components to changes in the corresponding IMF parameter for each UT hour, for example [Papitashvili et al., 1994]

$$H^i = K^i_{HB_x} B^i_x + K^i_{HB_y} B^i_y + K^i_{HB_z} B^i_z + HO^i, \tag{3.2}$$

where K^i_H are regression coefficents for the corresponding IMF component, $i = 1, \ldots, 24$, where i is the UT hour, HO^i, is a residual term representing H for average conditions of the solar wind (e.g. $n = 4$ cm, $V = 450$ kms^{-1}). The term, HO^i can be expanded to include changes in the solar wind velocity and density but in the IZMEM model, this expansion is not carried out by the authors.

The regression coefficients are determined by an interpolation of all points for each UT hour, resulting in 24 values of K^i_H for each observatory. The electrostatic potential and equivalent current function are derived using this regression model of geomagnetic variations. The electrostatic potential is a function of conductivity, and statistical models are used to derive the ionospheric conductivity in both northern and southern polar regions (see Papitashvili et al. [1994] for details). The IZMEM electrodynamic parameters were obtained initially using the iono-

spheric conductivity distribution derived for local noon and local midnight. The average of the two conductivity distributions is then used to compute the entire set of electrodynamic parameters. This averaging avoids any UT dependence of the IZMEM output but assumes that the geographic and geomagnetic poles are coincident [Papitashvili et al., 1994].

The IZMEM model was the first model of ionospheric convection fully parameterised by the IMF strength and direction. Ionospheric convection patterns can be derived for both northern and southern polar regions and for all three seasons (summer, winter and equinox) from IMF data alone. The model is derived from a large quantity of geomagnetic data from ground-based observatories located at different local times in the polar cap region. The numerical algorithm is similar to the KRM [Kamide, Richmond, and Matsushita, 1981], assimilative mapping of ionospheric electrodynamics (AMIE) [Rich and Kamide, 1988] and technique of inversion of the magnetogram (TIM) [Mishin et al., 1980] but differs from these techniques in that the IZMEM model does not require a selection of magnetically quiet periods or the use of spherical harmonic expansion to process the initial geomagnetic data and cover large gaps between magnetic observatories at high latitudes [Papitashvili et al., 1994]. The model does not require an in-situ collection of magnetometer data, only IMF data, to calculate global convection patterns and electric potentials.

The IZMEM model splits the IMF B_z into negative (southward) and positive (northward) components, which generally represent disturbed and quiet geomagnetic conditions, respectively, although a northward B_z can also induce a strong polar cap current. During intervals of $B_z < 0$ a standard two-cell convection pattern with antisunward flow over the polar cap is observed. During intervals of $B_z > 0$, the reverse two cell convection pattern is developed on the dayside of the polar cap [Papitashvili et al., 1995].

The IZMEM model is limited in that it does not allow for a solar wind viscosity influence and is only broadly variable with respect to average dipole tilt; summer, winter and equinox split only. Ground-based geomagnetic disturbances

are assumed to be proportional to variations of the IMF components, which has been proven for IMF B_z but not for IMF B_y or B_x [Papitashvili et al., 1994]. The IZMEM approach is somewhat indirect in that a model is used to infer the ionospheric conductivity which is then used to calculate the electrostatic potential distributions from a distribution of geomagnetic perturbations. No ionospheric conductivity model exists for the Southern Hemisphere and the model used in the IZMEM model was developed for the Northern Hemisphere. The geometry of convection patterns in both hemispheres, as inferred by the IZMEM model, are asymmetrical, indicating possible effects of using a northern hemisphere ionospheric conductivity model, a natural north-south asymmetry in the electric potential, or the ellipticity of the Earth's orbit. The ellipticity of the Earth's orbit means that the southern polar cap is facing more towards the sun than the northern polar cap at the perihelion of the Earth's orbit implying that the ionospheric conductivity should be greater for the Southern Hemisphere summer than for the NH summer [Papitashvili et al., 1994]. The IZMEM model is limited to specifying large scale, quasi-steady events but can be used to investigate short-term events. The model cannot forecast magnetic substorms and its accuracy is not guaranteed for periods following such an event.

Chapter 4

Instrumentation and Data Selection

In December 1997 a rotating dipole electric field mill was deployed at Vostok, Antarctica, under a cooperative research effort between the Russian Arctic and Antarctic Institute, Australian Antarctic Division, Space Physics Research Laboratory of the University of Michigan and the University of Houston. The instrument was designed to measure the vertical component of the atmospheric electric field. Vostok station was an ideal site for this purpose because of its location; situated on the Antarctic Plateau, approximately 3500 m above sea level, at 78 °28′ S and 106 °48′ E. The Plateau is extremely flat and has a desert-like climate, it is relatively free from local disturbances and man-made atmospheric pollution. The local atmospheric convection is minimised by a deep temperature inversion, the local weather patterns are exceptionally stable and the sky clear throughout the year. The local topography results in an amplification factor of 2 or more in electric field strength and the current density.

Previous studies of the geoelectric field at the Vostok site have shown promising results. Park [1976b] demonstrated that the global fair-weather diurnal curves could be detected at Vostok and showed that the influence of the solar magnetic sector structure of the IMF on the variations of the vertical electric field could be discerned. Burns et al. [1998] provided statistical evidence that the geoelec-

tric field at Vostok is modulated by the IMF B_y components during times when Vostok is magnetically linked to the dayside interaction region between the solar wind and the Earth's magnetic field. Frank-Kamenetsky et al. [1999] confirmed that the influence of the cross polar cap potential difference could be discerned in ground based geoelectric field measurements at Vostok and found significant correlations (less than 5% probability of chance correlation) for six individual hours when Vostok was on the magnetic and geographic dayside. Previously to this, Tinsley et al. [1998] showed positive correlations between surface electric field measurements observed at South Pole (CGM $\Phi = -73.91\ ^\circ$, $\Gamma = 18.73\ ^\circ$) and the overhead ionospheric electric potential as predicted by the Hairston and Heelis [1990] model.

The electric field mill deployed at Vostok in 1997 is a rotating dipole electric field mill, similar to that used at Davis Station [Burns et al., 1998] and at Vostok Station by Park [1976a]. The newer mill has several advantages over previous mills in that its output is digital and can be calibrated regularly. A recent paper by Frank-Kamenetsky et al. [2001] published the first set of results using data from the first year of operation in 1998. Correlations of variations in the average electric field measurements with IMF B_y and B_z showed that the electric fields at Vostok responded to changes in both IMF components.

This chapter gives an overview of the electric field mill and its operation, the improvements made to the mill design and the calibration process. A brief description is given of the criteria used by Frank-Kamenetsky et al. [2001] to select fair-weather days of electric field data for further analyses as well as the IMF dataset selected to predict the cross polar cap potential differences above Vostok.

4.1 The Rotating Dipole Electric Field Mill

The electric field mill deployed at Vostok is similar to the type used by Park and was originally used at Davis Station. The descriptions given in this section

are taken from an internal Australian Antarctic Division document by Symons [1997]. The mill was refurbished in 1995 before deployment to Vostok station. In this refurbishment, the internal electronics of the mill were completely redesigned and a new data acquisition system was developed to simplify the installation and operation of the instrument. This was important because of the extreme temperatures that the mill would be expected to encounter. The temperature at Vostok ranges from −30 °C to −89 °C, with an average temperature of about −70 °C during winter months. Many commercially available electronic components are inoperable at these temperatures, and while there are some military components available that can handle temperatures down to −55 °C, it was not feasible to obtain these parts. Changes were made to the mill design to allow the use of commercially-available components rated to −40 °C in the extreme temperatures to be expected at Vostok and to allow it to be internally heated. Fibreglass cladding was added to the rear of the mill to provide some thermal insulation, the motor voltage was increased from 180 V to 240 V and two large 100 Ω power resistors were added to each of the circuit boards, increasing the power dissipated and thus generating excess heat. With these additions, the temperature inside the mill is −27 °C when the outside temperature is −80 °C.

4.1.1 Principles of Operation

The electric field mill uses a rotating dipole technique to measure the vertical component of the geoelectric field. When the mill is placed in an external electric field, a static charge is induced on the surface of the dipole antenna. In the horizontal position, the two halves of the dipole are in equipotential. In the vertical position, each half of the dipole acquires a potential equal to that of the surrounding electric field and the difference in potential between the two halves induces a current flow across the dipole. The dipole is rotated, at a constant speed, in the vertical plane to measure the vertical component of the electric field. As the dipole is rotated a sinusoidal alternating current, which is proportional to the rate of change of electric charge flowing across the dipole, is generated. The

signal is amplified and converted to a DC voltage.

4.1.2 Mechanical and Electronic Design

The electric field mill consists of a dipole antenna connected to a 240 V AC induction motor, an optical chopper and sensor, and several electronic circuits responsible for amplifying, converting and storing the sinusoidal signal. The field mill is housed in a large diameter aluminium tube which acts as an electrical shield for the internal components. A cross-sectional diagram of the electric field mill is shown in Figure 4.1. The dipole is connected to the motor via a drive

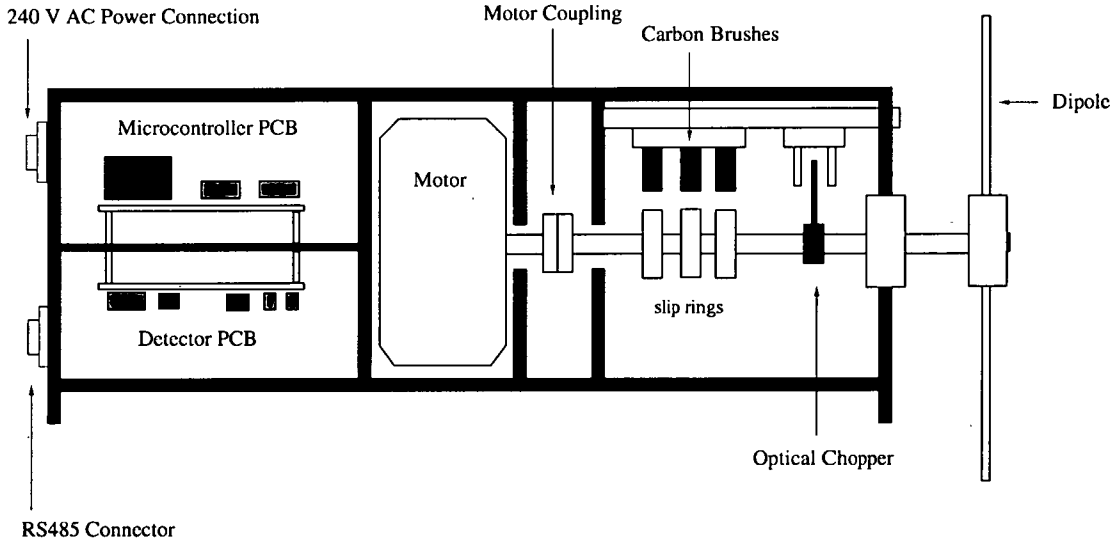

Figure 4.1: Cross sectional diagram of the electric field mill

shaft which protrudes through one end of the mill. The three slip rings on the shaft provide the contact between the carbon brushes and the two halves of the dipole. The optical chopper, also on the shaft, is used to detect the orientation of the dipole and hence the polarity of the external electric field. It is aligned with the dipole, as shown in Figure 4.2, and rotates with the dipole. An optical sensor detects the motion of the optical chopper and is switched on and off as each half of the dipole passes through the top vertical position. Signals from the dipole and the optical sensor are passed via the brushes to the two printed circuit boards located at the rear of the mill. The circuit boards are housed in separate,

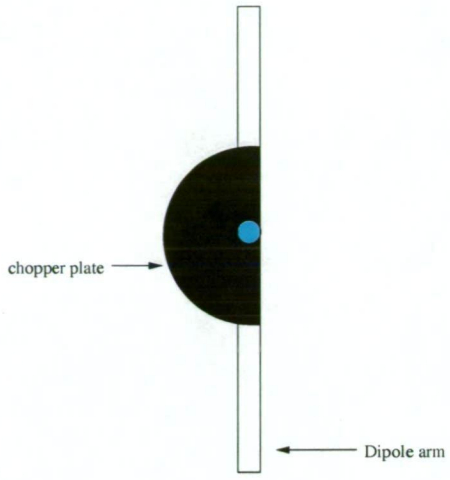

Figure 4.2: Alignment of the optical chopper with respect to the dipole arms

shielded chambers to minimise any radiated interference between the two boards. The bottom circuit board (see Figure 4.1) contains a synchronous detector circuit that amplifies and converts the dipole AC current into a high level proportional DC voltage. The synchronous detector uses the signal from the optical sensor to switch the positive and negative cycles of the input signal through inverting and non-inverting amplifiers to produce a rectified sinusoidal signal which reflects the polarity of the external electric field. A 4-pole low-pass filter is then used to obtain the DC component which is then sent to the 12-bit analogue-to-digital converter located on the microcontroller PCB (on the top circuit board). The signal is converted to RS486 format and transmitted to a host PC located nearby. The mill also transmits information on the temperature of the windings and the detector PCB assembly and the speed of the motor, which is collected by the PIC 16C73 microcontroller.

4.1.3 Calibration

The electric field measurements are accurate to 1 Vm^{-1}. The output of electric field mill is dependent on the local field which is in turn related to its physical surroundings. In-situ calibrations of the electric field mill were carried out by Russian scientists at Vostok on a monthly basis and the electric field mea-

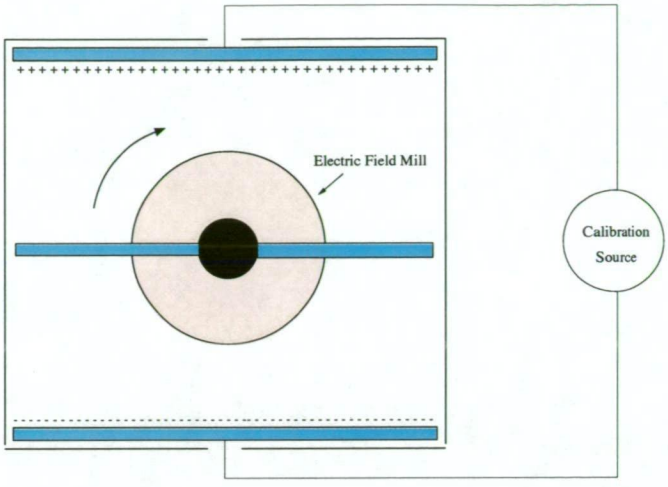

Figure 4.3: Cross sectional diagram of the calibration box used to calibrate the electric field mill.

surements adjusted accordingly. The calibration process involved generating an electric field of known potential difference across the dipoles of the electric field mill and recording the values measured. The electric field was generated by applying a range of voltages, up to 600 V, across two parallel plates contained within an aluminium box. The aluminium box was fitted over the front of the mill, fully enclosing the dipoles, and acting as a Faraday cage. Any external electric fields were excluded, ensuring that the field mill measured only the artificial vertical electric field during calibrations. A cross-sectional diagram of the calibration box is shown in Figure 4.3.

The mill output was stored in binary format. The digital values were converted into physical units using,

$$E_Z = m \times E \text{ (digital)} + C, \tag{4.1}$$

where m and C is the slope and y-intercept of the graph E (digital) versus applied voltage, E_Z. Plots of the calibration curves are plotted in Figure 4.4. A variation in offset up to ~ 20 Vm^{-1} between calibrations were recorded over the December 1997 to November 1998 period. The largest offset values occurred for the months of May to June and June to July. The equations for these months are

$$E\ (Vm^{-1}) \quad = \quad 1.02 \times E \text{ (digital value)} + 102,$$

$$E\ (Vm^{-1}) = 0.98 \times E\ (\text{digital value}) + 122.2,$$
$$E\ (Vm^{-1}) = 1.02 \times E\ (\text{digital value}) + 103.8.$$

For the remaining months, the offsets were less than 6 Vm^{-1}. The slope of the graphs remained relatively constant for the December 1997 to February 1998 and the March 1998 to November 1998 periods. The electric field mill was replaced in March 1998 by a second identical mill due to technical problems with the first mill. The change in instruments is evident as a change in slope, from an average value of 1.52 to 1.02 Vm^{-1}per digital unit (see Figure 4.4). The vertical electric field values were adjusted each month to reflect the new calibration readings.

4.1.4 Site Selection

The selection of the mill site is an important factor in insuring that the data collected is free from local influences. The position of the field mill at Vostok is shown in figure 4.5. The site was chosen by Dr Frank-Kamenetsky and Mr Lloyd Symons, so that the field mill could be easily and safely accessed on a monthly basis, even in mid-winter, and be within 200 m of the 240 V AC power source. The mill was placed upwind of any buildings or machinery, especially, the station's diesel power generator, which might emit polluting fumes that could alter the conductivity of the air. It was also placed at some distance from buildings or antenna masts and power lines which might distort the local electric field. The mill was mounted on a steel pole at a distance of about 1.5 m above the surface of the snow and aligned with the prevailing wind direction, southeasterly, with the dipoles facing into the wind to minimise the effect of the actual mill on the conductivity of the air. The power, communications and calibration cables were buried in a shallow trench in the ice to prevent wind from vibrating the cables and affecting the measurements.

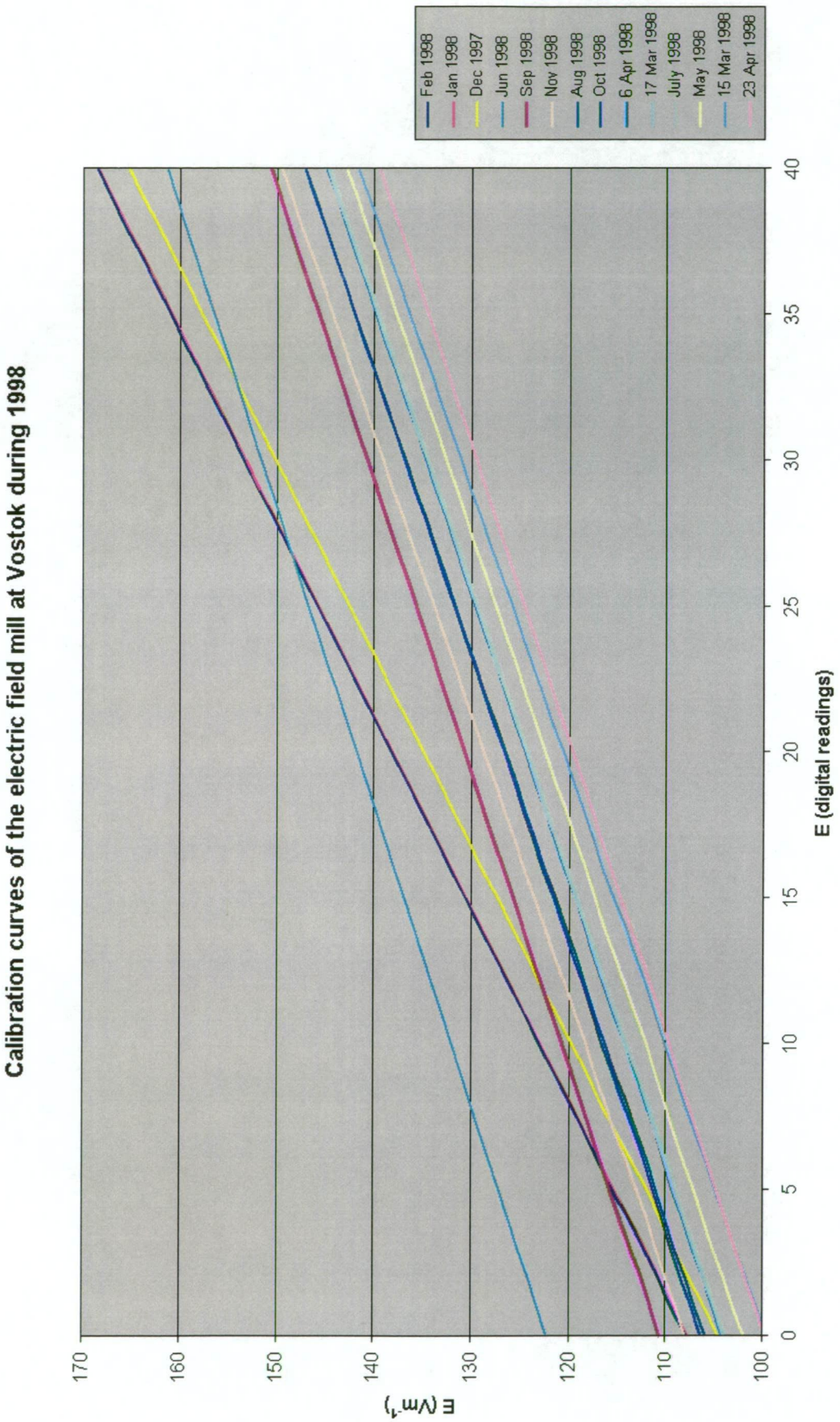

Figure 4.4: Plots of the calibration curves for the electric field mill at Vostok station during 1998

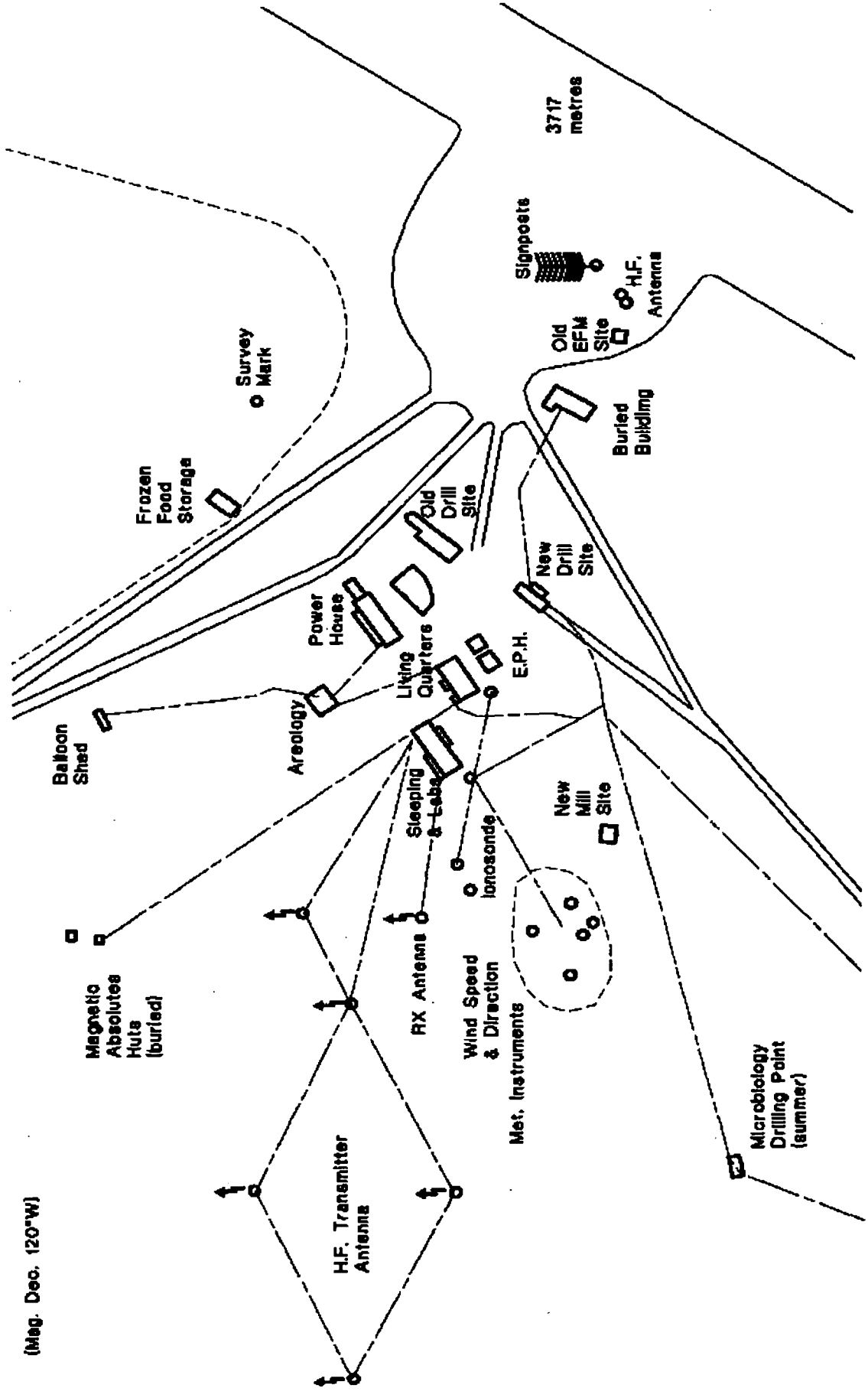

Figure 4.5: Map of Vostok Station showing the electric field mill location

4.2 Data Selection

4.2.1 Selection of the Geoelectric Field Data

Frank-Kamenetsky et al. [2001] selected a total of 134 days which satisfied fair-weather conditions and contained a complete 24 hours of electric field measurements. Local meteorological phenomena, aerosol particles and vertical convective air currents can strongly influence the measurements of the geoelectric field near the surface, making the detection of the global circuit extremely difficult. It is generally believed that electric field measurements at Vostok are significantly dependent on the wind velocity [Burns et al., 1998]. High winds can lift and carry fine ice particles large distances. The ice particles can carry a large and variable electric charge which can cause large variations in the local conductivity or can attach a strong and rapidly varying electrical charge to the electric field mill antennae. For this reason, days with wind velocities greater than 6.5 ms^{-1} were excluded as well as days with falling or drifting snow. Winds at Vostok are typically southwesterly and do not adversely affect the electric field measurements. Northeasterly winds, however, occassionally cause unusually large values of E_z to be obtained. It is generally believed that the high electric field values are as a result of pollution emitted by the station's diesel power plant which is located approximately 200 m north-east of the electric field mill.

In this study, a dataset consisting of 133 of the 134 Frank-Kamenetsky et al. [2001] selected fair-weather days was selected for further analysis. The 20th of March, 1998, was excluded due to incomplete 24-hours of hourly electric field values. Daily averages of E_z can vary significantly due to variations in the global electric circuit and a complete 24-hours of electric field measurements is essential in ensuring unbiased diurnal averages. It is not known whether this missing hour is also missing in the original dataset, Frank-Kamenetsky et al. [2001], or only inherent in the dataset provided.

4.2.2 Selection of the Interplanetary Magnetic Field Data

Hourly-averaged Interplanetary Magnetic Field (IMF) components and solar wind plasma data were obtained from the National Space Science Data Centre (NSSDC) OMNIWeb database and used as inputs for the models employed to calculate the cross polar cap potential difference above Vostok.

The OMNI IMF data consisted of measurements made by the Interplanetary Monitoring Platform 8 (IMP8), Wind and Advanced Composition Explorer (ACE) satellites. The OMNI solar wind data consisted only of measurements from the IMP8 and Wind satellites. Wind and ACE data were used only when IMP8 data was unavailable or when the hourly averages from IMP8 were based on five or less data points (out of a possible 45) and Wind or ACE were based on more than 5 data points [King and Papitashvili, 1999]. IMP8 is located close to the Earth, typically within 12 minutes for average solar wind flow speeds. IMP8's orbital path takes the spacecraft in and out of the Earth's magnetopause, thus limiting the times when IMF and solar wind speed data can be obtained. The Wind and ACE spacecraft are located much further out, at the L1 libration point, and do not have the same problems as IMP8. However, their location puts them about 1 hour upstream of the Earth. Data from Wind and ACE are timeshifted to Earth using position information and solar wind speed data before building hourly averages and interspersing with IMP8 hourly averages in OMNI [King and Papitashvili, 1999].

Of the 133 selected days, IMF and solar wind speed data were available for 95% of the selected hours. IMP8 provided 46% of the IMF data and 45% of the solar wind speed data, Wind 49% and 50% respectively and ACE 0.3% of the IMF data.

Chapter 5

The Diurnal Geoelectric Field

Fair-weather diurnal curves have previously been detected in ground-based measurements at Vostok Station, Antarctica [Burns et al., 1998, Park, 1976b, Frank-Kamenetsky et al., 1999, 2001]. In the past, the electric field measurements were recorded on chart recorders and average hourly values, centred on the half hour, determined from these charts. The electric field mill deployed at Vostok station in December 1997 was designed to be simple to operate and install, enabled regular on-site calibration and digitally recorded measurements of the geoelectric field. The electric field measurements from the mill are expected to be more accurate and reliable, resulting in a larger number of data suitable for further analysis.

Park [1976a] stated that Vostok's location near the centre of the polar cap tends to minimise the effects of electric generators in the magnetosphere and ionosphere. Not only has Park's statement been disproved experimentally but also theoretically it was expected to be incorrect [Tinsley and Heelis, 1993]. Frank-Kamenetsky et al. [1999] have shown that the interaction of the solar wind with the Earth's magnetosphere can be detected in ground measurements of the vertical electric field at Vostok. Vostok's location near the centre of the polar cap and hence near the geomagnetic pole, minimizes the effect of B_z but maximizes the effect of B_y on the day-to-day variability of the ionospheric convection potential patterns across the polar cap. Frank-Kamenetsky et al. [1999] have shown that this interaction of the solar wind with the Earth's magnetosphere can be detected

in ground measurements of the vertical electric field at Vostok. The influence of the solar wind on ground measured geoelectric fields had previously been demonstrated by Tinsley et al. [1998] using South Pole data. Using the 1998 Vostok dataset and models of the imposed polar cap potential, we compare the seasonal diurnal curves, both uncorrected and corrected for the polar cap influence, with the Carnegie seasonal curves [Israel, 1973] and their re-analysis by Adlerman and Williams [1996]. In this chapter the 1998 Vostok diurnal curves are compared to previous Vostok electric field studies [Frank-Kamenetsky et al., 1999, 2001, Park, 1976a].

5.1 Results

Diurnal variations were calculated using raw electric field data for all 133 fair-weather days. Figure 5.1(a) shows the diurnal curve of the raw electric field data and figure 5.1(b) shows all the hourly values used to calculate this diurnal curve. The mean is 176.6 Vm^{-1}, the diurnal minimum occurs at 3.5 UT and the maximum at 19.5 UT and the range, as a percentage of the mean, is 28.9% (see Table 5.1). Standard errors

$$\sigma = \frac{s}{\sqrt{n}}, \tag{5.1}$$

where s is the standard deviation and n the number of data points, are shown for each UT hour in figure 5.1(a). In figure 5.1(b) the electric field values are plotted 30 minutes earlier to allow a plot of the average hourly values to be shown on the same set of axes.

To allow for a more direct comparison with the Frank-Kamenetsky et al. [1999] results, scaled electric field values were also calculated,

$$E_S(day, h) = \frac{E(day, h)}{\bar{E}(day)} \times \bar{E}(133days). \tag{5.2}$$

The diurnal curve and scaled electric field data are presented in figures 5.1(c) and 5.1(d), respectively. The range of the raw and scaled diurnal curves differ only by $\sim 0.5\%$ (see Table 5.1). This difference is considered to be insignificant

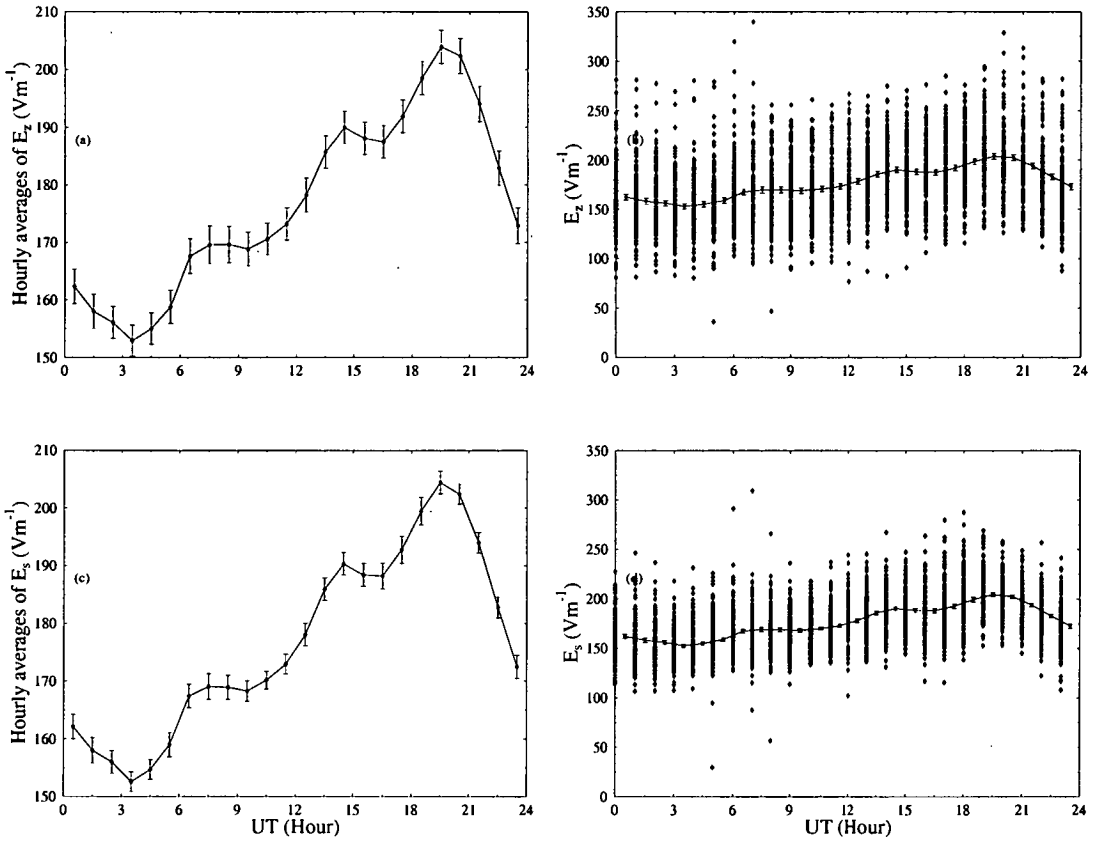

Figure 5.1: (a) The average diurnal curve of the 133 selected days. (b) All the data that contribute to the average geoelectric field diurnal curve. (c) The average diurnal curve of the 133 days of the scaled electric field values. (d) All the scaled geoelectric field values for the 133 days of selected data that contribute to the scaled average geoelectric field diurnal curve. Note that the error bars are $\pm$ one standard error and the values of the electric field in figures (b) and (d) are offset by 30 minutes.

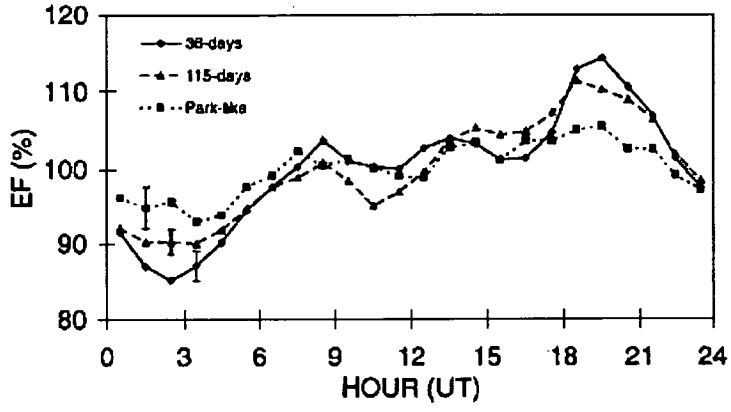

Figure 5.2: Frank-Kamenetsky et al. [1999] Vostok 1979 to 1980 scaled, average diurnal curves of geoelectric field observed for the primary (36 days) and secondary (115 days) data sets, along with the curve derived from the May 1979 to May 1980 data treated as per Park [1976a] [Frank-Kamenetsky et al., 1999]

and unscaled values are used hereafter for determining the annual and seasonal values.

Table 5.1 also lists the mean, the range and the UT hours of the diurnal minimum and maximum for previous Vostok studies [Park, 1976a, Frank-Kamenetsky et al., 1999] and the Carnegie cruises [p.369 Israel, 1973]. The mean value of the Carnegie curve was calculated from monthly averages presented in the re-analysis by Adlerman and Williams [1996].

Figure 5.2 shows the scaled average diurnal curves for the three datasets discussed by Frank-Kamenetsky et al. [1999]. Figure 5.3 shows the Park [1976a] diurnal curve and figure 5.4 shows the Carnegie curves [Reiter, 1992].

Frank-Kamenetsky et al. [1999] scaled the electric field measurements to remove the day-to-day variation from the derivation of the diurnal curve, as per equation 5.2. The authors selected three datasets, each based on slightly different selection criteria and with progressively less stringent meteorological selection criteria. 36 fair-weather days were selected on the basis of strict fair-weather criteria; a complete 24 hours of electric field values, and in the interval May to

Table 5.1: Results of all studies utilising data measured at Vostok Station and the Carnegie data

	Min. (UT hour)	Max. (UT hour)	Range (%)	Mean (Vm^{-1})
Vostok 1998 Jan. - Dec., 1998 133 days, Raw EF	3.5	19.5	28.9	176.6
Vostok 1998 Jan. - Dec., 1998 133 days, E_s	3.5	19.5	29.4	176.6
Vostok 1979 May - Dec., 1979 36 days, E_s [Frank-Kamenetsky et al., 1999]	2.5	19.5	29	169
Vostok 1979 May 1979 to May 1980 115 days, E_s [Frank-Kamenetsky et al., 1999]	3.5	18.5	21	146
Vostok 1979 Mar. - Nov., 1979 Park criteria, 174 days E_s [Frank-Kamenetsky et al., 1999]	3.5	19.5	17	Not given
Vostok 1974 Mar. - Nov., 1974 [Park, 1976a]	5	20	23	93.7
Carnegie [Israel, 1973, Reiter, 1992]	3.5	19.5	37	132 [a]

[a] calculated from Adlerman and Williams [1996].

December when hourly wind speeds and directions were available. The 115 days were selected from 13 months of data, May 1979 to May 1980, based on strict fair weather criteria and complete 24 hours of electric field data. The data were not constrained to times when concurrent wind speeds and directions were available. The final dataset consisted of the equivalent of 174 days of data, selected using similar criteria to that used by Park [1976a]; days with falling or drifting snow and ice were excluded, as well as electric field values measuring more than 353 Vm^{-1}. Complete 24 hours of electric field data was not an essential criteria.

The same UT variation is evident in all the diurnal curves (figures 5.1, 5.2, 5.3 and 5.4). The Vostok 1998 diurnal curve exhibits a minimum at $\sim$ 3.5 UT, a maximum at $\sim$ 19.5 UT as well as two smaller peaks at $\sim$ 7.5 UT and $\sim$ 14.5 UT. These features are also observed in the Vostok 1979 and 1974 diurnal curves as well as the Carnegie curve at approximately the same times. The 36 days, Vostok 1979, diurnal curve minimises an hour earlier and peaks at $\sim$ 8.5 UT, $\sim$ 13.5 UT and $\sim$ 19.5 UT. The secondary Vostok 1979, diurnal curves minimise and peak at approximately the same UT hours. The UT hour of the diurnal mininum of the Vostok 1974 diurnal curve is much later than any of the other curves, $\sim$ 5 UT but the diurnal maximum and secondary peaks occur at about the expected times, 20 UT and 8 and 14 UT, respectively.

The range of the diurnal variation of the Vostok 1998 curve is similar to the range of the 36 days Vostok 1979 curve but is still less than the expected range

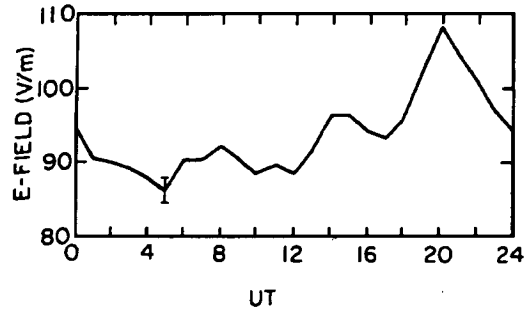

Figure 5.3: Park [1976a] vertical geoelectric field measured at Vostok during March - November 1974. A typical standard error of the mean is shown at 5 UT.

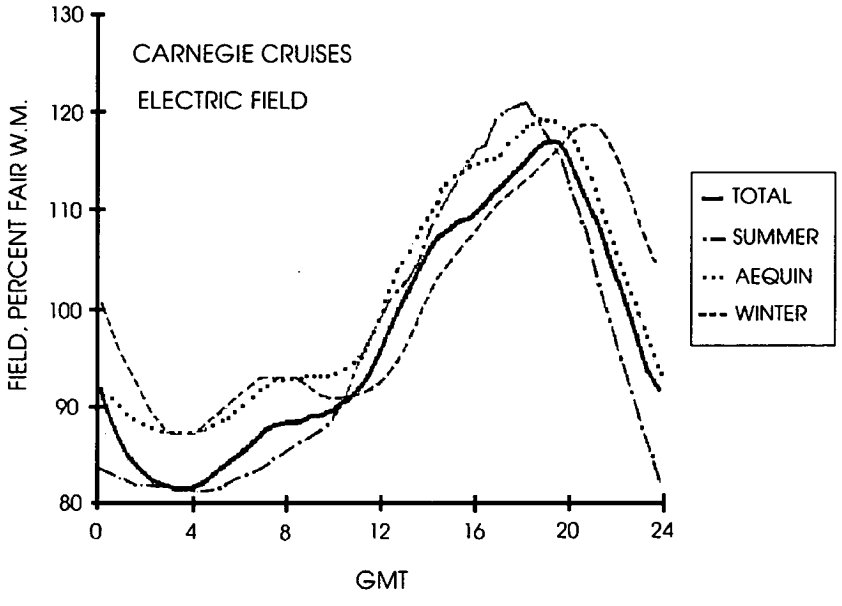

Figure 5.4: The Carnegie curves. Fair-weather diurnal variations of the electric field in percent of the fair-weather mean measured by the Carnegie vessel. Data subdivided with respect to the austral seasons, winter (May to August), summer (November to February) and equinox (March, April, September,October) (figure taken from Reiter [1992] but modified to show Southern Hemisphere seasons).

of the Carnegie curve, 37%. Of the three Vostok 1979 datasets, the primary dataset had the greatest diurnal range, possibly due to the tighter meteorological rejection criteria applied to that dataset [Frank-Kamenetsky et al., 1999]. The range of the Vostok 1974 diurnal curve, 23% of the mean, is more comparable with the diurnal curve of the Vostok 1979, 36 days dataset than the similarly selected 174 days. The mean value of the Vostok 1998 data is also similar to the mean of the 36 days, Vostok 1979 dataset. The average value of the Vostok 1974 dataset is significantly less, 93.7 Vm^{-1}.

Daily averages fluctuate greatly, from a minimum value of 111 Vm^{-1} to 237 Vm^{-1} (see figure 5.5), and peaking during the winter. Frank-Kamenetsky et al. [2001] reported that a polynomial fit of the daily averages resulted in a smooth seasonal variation with a maximum in August, minima in April and De-

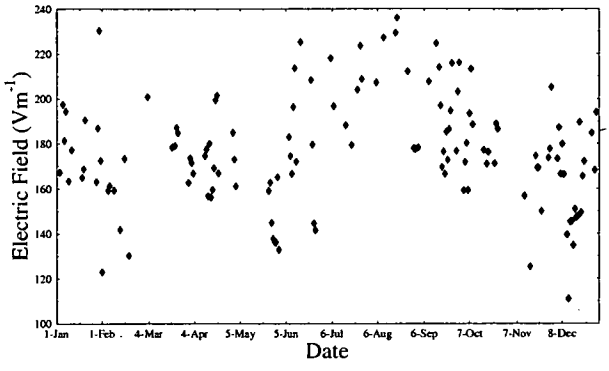

Figure 5.5: The daily mean of each of the 133 days of selected data. A seasonal variation is apparent, maximal during August, SH winter.

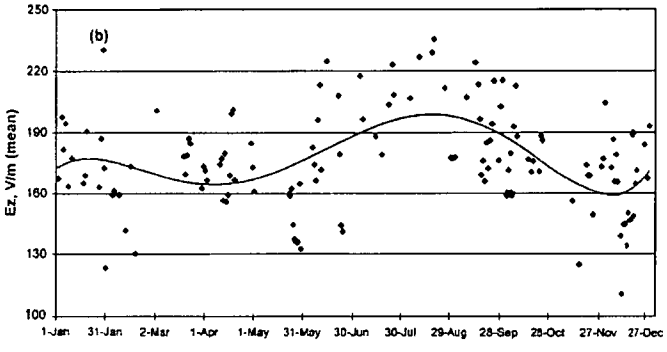

Figure 5.6: The seasonal variation of electric field values obtained by fitting a polynomial curve to daily averages of the electric field measurements.

cember and a range of 40 Vm^{-1}. The polynomial fit applied by Frank-Kamenetsky et al. [2001] is shown in figure 5.6. A wintertime maximum is clearly observed in the daily averages (see figure 5.5) and corresponds with the expected Northern Hemisphere summer maximum [Adlerman and Williams, 1996]. The range of the maximum peak covers the months of June to October, encompassing three winter months and 2 equinox months. The minima in April and December inferred by the polynomial fitting carried out by Frank-Kamenetsky et al. [2001] are not readily apparent in the raw data (see figure 5.5). The low outlying points with daily averages between $100 - 130$ Vm^{-1} in November and December may

significantly affect the shape of any fit applied to the data.

Seasonal diurnal variations for the Vostok site were calculated, by averaging electric field data, using the same seasonal splits as [Israel, 1973]; winter (May to August), summer (November to February) and equinoxes (September, October, April and March). Figure 5.7 shows the seasonal variations. Typical standard errors are plotted for one hour between 2 UT and 6 UT on each curve. The time occurrence of the minimum hourly value is mostly consistent throughout the year, appearing at 3.5 UT for the summer and equinox curves and at 4.5 UT for the SH winter curve. The time of maximum varies between 18.5 UT and 20.5 UT, the summer curve maximises first at 18.5 UT followed by the equinox curve at 19.5 UT and then the winter curve. The Carnegie seasonal diurnal variations peak in a similar fashion. Table 5.2 lists the times of the diurnal minimum and maximun, range and mean value for the seasonal diurnal variations for Vostok 1998 and Carnegie datasets. The seasonal averages of the Carnegie curve were calculated as averages of the monthly values determined by Adlerman and Williams [1996] in their reanalysis of the Carnegie data. Differences in the time occurrence of the diurnal minimum and maximum are evident between the two curves (see Table 5.2), however, the variations are less than an hour and can be considered to be minor.

Although the range of the Vostok 1998 total diurnal curve is much less than the corresponding Carnegie curve, the range of the summer seasonal curves are similar, 42% and 40% respectively. The range of the Carnegie equinox and winter curves are equal at 31% of the mean. The same trend is not observed in the Vostok 1998 equinox and winter curves. The range of the Vostok 1998 equinox curve is equal to the range of the total curve and not the winter curve. The range of the Vostok winter curve is very low at 19%. A comparison of the means show that the Vostok 1998 equinox and winter means are similar and have a value greater than the summer and total means. In the Carnegie seasonal curves, the equinoctal mean value is low and similar to the summer mean and the monthly mean value peaks during the winter.

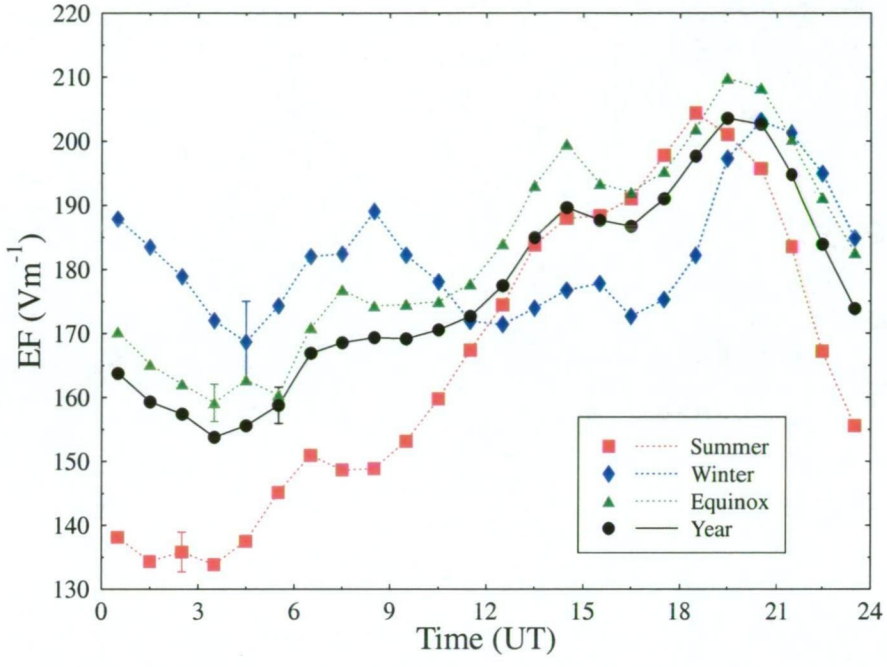

Figure 5.7: Average geoelectric field diurnal curve at Vostok for the SH winter, SH summer and equinox curves. A typical standard error is plotted for each curve between 2 and 6 UT.

In the next chapter (Chapter 6), the influence of the solar wind imposed polar cap potential on ground level measurements of the electric field at Vostok is clearly demonstrated. Allowances for this influence should be made in calculations of the diurnal variations, thus allowing a better comparison with the Carnegie curve. Of the 133 selected fair-weather days, 106 complete days of Vostok convection potentials were used to calculate the corrected electric field values; IMF and solar wind speed data, which are required inputs for the Weimer and the IZMEM models, were available for only 95% of the selected time, of which there were 106 days with complete 24 hours of data. The seasonal diurnal variations were initially recalculated on the basis of these 106 days without correction for the influence of the solar wind imposed polar cap potential. The times of the diurnal

Table 5.2: Results of Vostok 1998 data and Carnegie data

		Min. (UT hour)	Max. (UT hour)	Range (%)	Mean (Vm^{-1})
Vostok Raw EF	Summer	3.5	18.5	42	166
	Equinox	3.5	19.5	28	183
	Winter	4.5	20.5	19	182
	Total	3.5	19.5	28	177
Carnegie	Summer	3.5	17.5	40	125 [a]
	Equinox	3.5	19.5	31	125 [a]
	Winter	3.5	20.5	31	147 [a]
	Total	3.5	19.5	37	132 [a]

[a] calculated from Adlerman and Williams [1996].

minimum and maximum are unchanged, except for the diurnal minimum of the equinox curve which minimises two hours later at 5.5 UT. The average hourly value at 3.5 UT is only slightly higher than the minimum value, 157.8 Vm^{-1} compared with 155.9 Vm^{-1} (see Table 5.3). The range values are approximately the same and vary only by $\sim$ 3%. The mean values have also changed slightly. The mean of the summer diurnal curve is increased by 4 Vm^{-1} to 170 Vm^{-1}, the mean of the winter curve is decreased by 5 Vm^{-1} to 177 Vm^{-1} and the mean of the equinox and total curves are basically unchanged.

The $\sim$ 250 kV potential difference between the ionosphere and the ground yields a vertical electric field of $\sim$ 177 Vm^{-1} for the Vostok site, implying a ratio of 0.7 Vm^{-1}/kV (see page 41, section 2.4.2). The average imposed polar cap potential above Vostok station, predicted using the Weimer and IZMEM models, is subtracted from the average electric field using this ratio, 0.7 Vm^{-1}/kV, to allow for the influence of the imposed polar cap potential on the global signal of the geoelectric field variation at Vostok. Diurnal variations, calculated using these

corrected electric field measurements are shown in figures 5.8 and 5.9. The diurnal variation of the raw electric field measurements and the Weimer and IZMEM inferred potentials are also shown. Times of the diurnal minimum, maximum, range and mean are shown in Table 5.3 for both Weimer and IZMEM corrected diurnal curves as well as the Carnegie curves.

The range of the corrected diurnal curves have increased by between 6% and 12% (see figures 5.8 and 5.9). The range of the total diurnal curve for both Weimer and IZMEM models, 36% of the mean value, are comparable to the Carnegie value of 37%, however, the range of the corrected summer diurnal curves, $\sim$ 50%, is excessive when compared to the associated Carnegie value of 40%. The times of the diurnal minimum and maximum are basically unchanged with one exception, the diurnal curve of the equinoctal, Weimer model corrected electric field values reaches a minimum at 5.5 UT instead of 3.5 UT. The average hourly value at 3.5 UT, 155.6 Vm^{-1}, is not too dissimilar to the value at 5.5 UT, 153.2 Vm^{-1}. Using Weimer model potentials to allow for the influence of the solar wind on the electric field values results in increases in the mean values for each of the seasonal curves. The increases are such that the mean values of the equinox, winter and total diurnal curves are now similar and the mean value of the equinox curve is not significantly greater than the mean of the winter curve. IZMEM model predicted potentials tended to decrease the mean of each seasonal curve. The mean of the IZMEM corrected summer and total curves are similar in value, with the equinox curve still showing the highest mean value.

The average diurnal variation of the Weimer and IZMEM inferred polar cap potential generally appears to be the inverse of the electric field diurnal curves (see figures 5.8 and 5.9), maximising between 4.5 UT and 6.5 UT and minimising between 18.5 UT and 20.5 UT. The maximum values occur about an hour later than the corresponding minimum on the diurnal field curves. Subtracting the model inferred polar cap potential results in changes to the diurnal range but not to the times of the diurnal minimum and maximum due to a fortuitous temporal alignment of the average imposed polar cap potential diurnal curve and

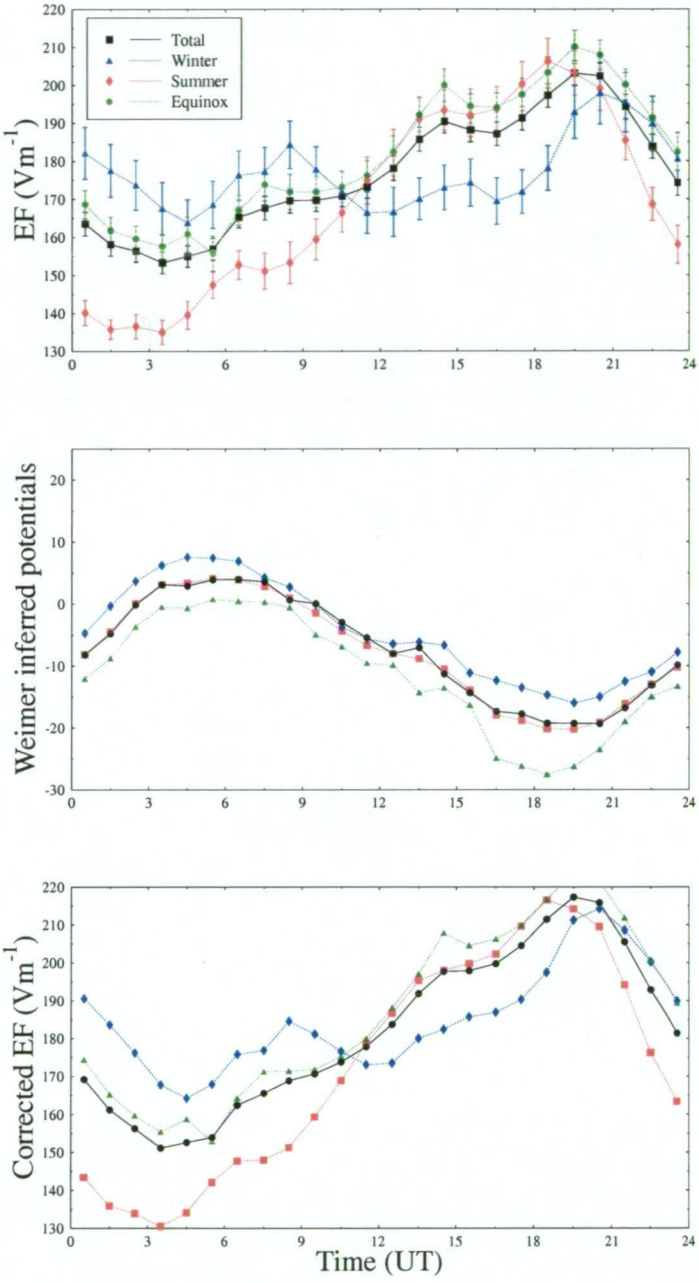

Figure 5.8: (a) The average geoelectric field diurnal curves at Vostok for the summer, winter, equinox and the full year (106 days). (b) The Weimer model calculated average imposed polar cap potentials above Vostok station. (c) Estimated global circuit variations obtained by subtracting the imposed polar cap potentials.

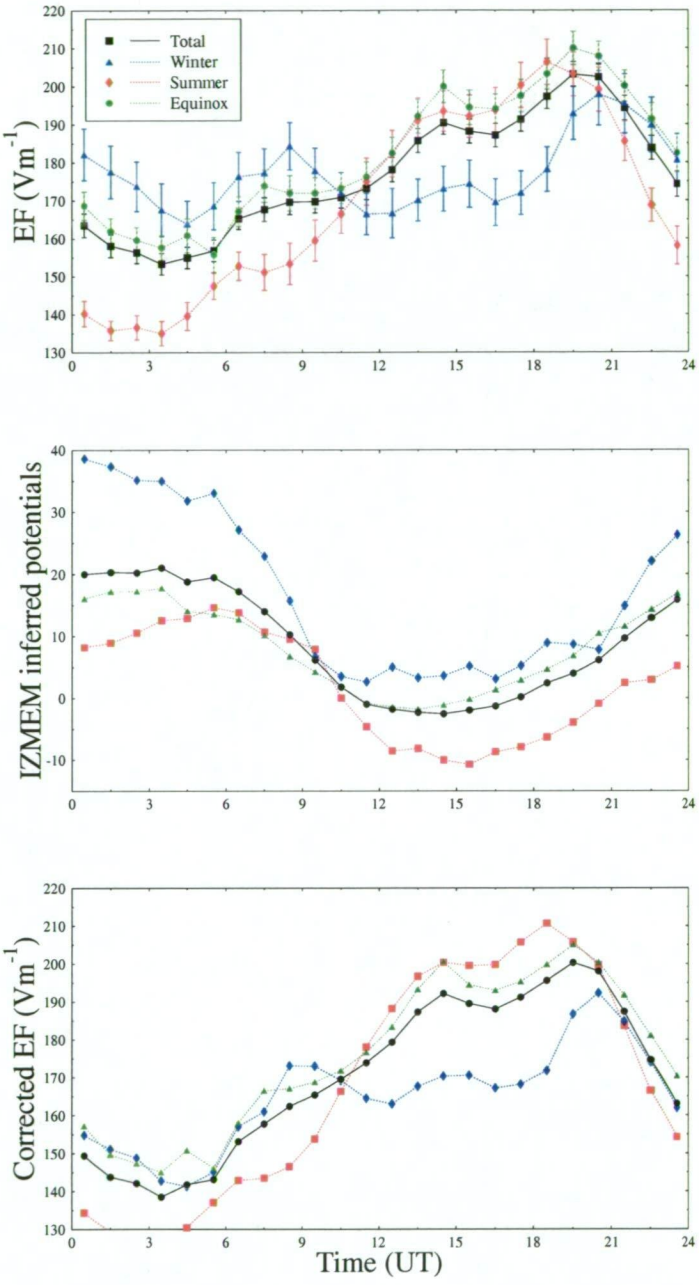

Figure 5.9: (a) The average geoelectric field diurnal curves at Vostok for the summer, winter, equinox and the full year (106 days). (b) The IZMEM model calculated average imposed polar cap potentials above Vostok. (c) Estimated global circuit variations obtained by subtracting the imposed polar cap potentials

Table 5.3: Results of Vostok 1998 data and Carnegie data

		Min. (UT hour)	Max. (UT hour)	Range (%)	Mean (Vm^{-1})
Vostok 1998, 106 days, Raw EF	Summer	3.5	18.5	40	170
	Equinox	5.5	19.5	31	182
	Winter	4.5	20.5	19	177
	Total	3.5	19.5	28	177
Corrected EF, Weimer model	Summer	3.5	18.5	50	173
	Equinox	5.5	19.5	38	187
	Winter	4.5	20.5	27	185
	Total	3.5	19.5	36	182
Corrected EF, IZMEM model	Summer	3.5	18.5	50	168
	Equinox	3.5	19.5	34	176
	Winter	4.5	20.5	31	165
	Total	3.5	19.5	36	170
Carnegie	Summer	3.5	17.5	40	125 [a]
	Equinox	3.5	19.5	31	125 [a]
	Winter	3.5	20.5	31	147 [a]
	Total	3.5	19.5	37	132 [a]

[a] calculated from Adlerman and Williams [1996].

the relatively low magnitude of the average values.

5.2 Discussion

Diurnal and seasonal variations of the Vostok electric field curves are generally comparable with the reported variations of the Carnegie curves. Consistent features include the shift to later UT of the maximum as the year progresses, the consistent appearance of the diurnal minimum between 3 and 4 UT and the range of the total dataset. The fair weather diurnal curve can be observed at Vostok Station using the more modern electric field mill, verifying once again, the suitability of the site for studies of the global electric circuit [Park, 1976a, Frank-Kamenetsky et al., 1999, 2001].

A total of 133 days, with complete 24 hours of electric field data, were selected on the basis of strict fair weather criteria. Previous studies have either relied upon fewer complete fair-weather days or included days with less than 24-hours of electric field data. For example, data from Vostok station observed during 1979 yielded 36 complete fair-weather days [Frank-Kamenetsky et al., 1999, Burns et al., 1995], South Pole observations from 1982 to 1986 resulted in 27 complete fair-weather days [Tinsley et al., 1998] and observations from Davis station [Burns et al., 1995] and balloon observations above South Pole station [Byrne et al., 1991] resulted in the equivalent of $\sim$ 46 and $\sim$ 19 days, respectively. Average daily values of the electric field may vary significantly because of variations in the global circuit. Selection of days with complete 24 hours of electric field measurements removes a possible bias from the diurnal averages.

The electric field measurements were recorded digitally, the measurements are accurate down to 1 Vm^{-1} and are less prone to the errors associated with the chart recorders used in previous studies. The electric field mill was calibrated on a regular basis, ensuring the relative accuracy of the electric field measurements. In the past, calibration of the data was determined before the equipment was deployed and no in-situ calibrations were made. Occasionally, data were not

recorded due to chart recorder failure or when charts and ink ran out. Chart data were also limited in the range of values they could measure, for example, the chart recorder used by Park [1976a] saturated when the electric field values reached 353 Vm^{-1}, and quickly varying electric field values could not be recorded accurately. The maximum electric field value for the Vostok 1998 dataset was $\sim$ 328 Vm^{-1}, below the saturation limit of the chart recorders.

The range of the Vostok 1998 diurnal curve is similar to the values observed by Park [1976a] and Frank-Kamenetsky et al. [1999] but is still much less than the range of the Carnegie curve, implying the influence of some other phenomena acting to reduce the range of the diurnal curve. The Vostok 1998 diurnal curve exhibits a minimum at 3.5 UT and peaks at 7.5 UT, 14.5 UT and 19.5 UT, similar to the peaks seen in the Carnegie curve and also corresponding to the peaks in predicted thunderstorm frequency for each of the three major continents (see figure 5.10). The peaks in the thunderstorm activity curve correspond to local afternoon time on each of the continents; Asia and Australia peak first at $\sim$ 8 UT, followed by Africa and Europe, and then America at $\sim$ 14 UT and $\sim$ 20 UT, respectively. The annual variation in the magnitude of the electric field at Vostok, which peaks

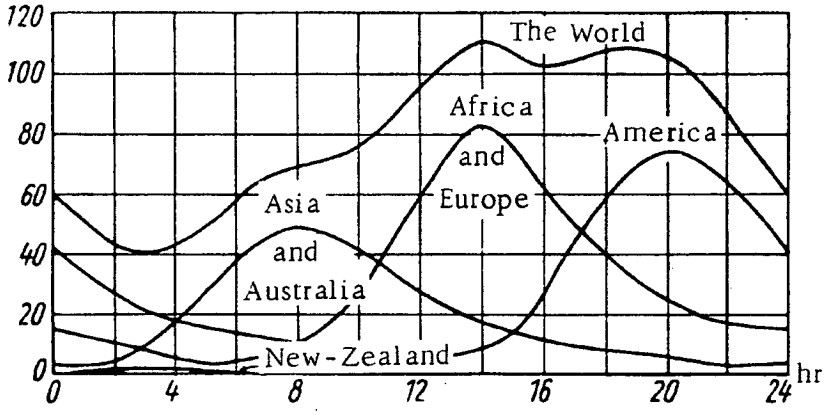

Figure 5.10: Estimated thunderstorm acitivity in major continents of the world plotted against UT [Israel, 1973]

during winter and minimises in the summer, is also consistent with the annual variation in global thunderstorm activity. Global thunderstorm activity should

be stronger during the NH summer (SH winter) because thunderstorm activity is principally a summer, landmass phenomena. The Carnegie curves were initially reported to show a NH winter peak in magnitude [e.g. Israel, 1973, p364-366] but the discrepancy was resolved by Adlerman and Williams [1996] who re-analysed the Carnegie data and found the expected NH summer peak.

The mean value of the Vostok 1998 dataset is higher than the mean of the Carnegie dataset. The Carnegie data were collected by the *Carnegie* research vessel during 1915-1929, over open ocean waters. Approximately half of the total columnar resistance occurs in the lower 3 km of the atmosphere. Sites located on the high Antarctic Plateau will have smaller columnar resistances than sites at sea-level. The local topography magnifies the electric field and current density but the shape of the diurnal variation should still be UT dependent and follow that of the global thunderstorm activity. This, however, does not explain why the Vostok 1998 mean is also higher than the Vostok 1974 mean. The Vostok 1998 electric field measurements are not absolute measurements of the electric field but representative of the potential difference applied across the parallel plates of a calibration box. The difference in the means may be due to monthly or yearly variations in either the average local atmospheric conductivity or global thunderstorm activity.

Differences between the Vostok and Carnegie diurnal and seasonal variations point to some of the uncertainties associated with using ground-level geoelectric field measurements to investigate the global circuit. The mean Carnegie equinoctal value is similar to the mean Carnegie summer value, whereas the mean equinoctal Vostok value is similar to the mean Vostok winter value. This is a significant distinction in terms of the annual variations. Although vertical electric fields are relatively easy to measure, these measurements are inversely proportional to the local conductivity. The possibility of seasonal variations in the local conductivity influencing the seasonal variations in the geoelectric field measurements have not been excluded.

Reducing the dataset from 133 days to 106 days resulted in slight changes

to the seasonal electric field variations, with the most notable changes occurring during the equinoctal months. The number of days in each season for the 106 days dataset are 34 days in summer, 42 in equinox and 30 days in winter compared to 49, 50 and 34 days for the 133 days dataset. A larger number of days were excluded, because of the lack of solar wind speed data, during the summer months of November to February. It is interesting to note that the seasonal diurnal curve showing the greatest difference between the two datasets occurred during the equinox months which lost only 8 days.

The average diurnal variation of the Weimer and IZMEM inferred polar cap potential above Vostok station generally appears to be the inverse of the electric field diurnal curves, maximising between 4.5 and 6.5 UT, about an hour later than the corresponding minimum on the diurnal field curves, and minimising between 18.5 and 20.5 UT. The implication of this is that the solar wind interaction with the Earth's magnetosphere reduces the diurnal range of the electric field values for the Vostok site but does not affect the time of diurnal minimum or maximum. The diurnal curves of the electric field measurements, corrected for the influence of the solar wind imposed ionospheric potentials, are still consistent with the diurnal variation of the uncorrected 106 days. The mean values are high, for the Weimer model corrected electric field values, the mean is 182 Vm^{-1} and the IZMEM model corrected electric field mean is 170 Vm^{-1}. The range of the diurnal curves are increased by between 6 and 12%. The range of the total diurnal curve for both Weimer and IZMEM models are 36% of the mean value, a value comparable to the Carnegie value of 37%. The range of both Weimer and IZMEM corrected summer diurnal curves, $\sim$ 50%, is excessive when compared to the associated Carnegie value of 40%. Average diurnal variations in conductivity at the site may influence such range measurements. The analysis approach presented in this study comparing the geoelectric field measurements with the imposed polar cap potentials above the site removes the effect of any day-to-day variation in ground level conductivity but does not preclude average diurnal conductivity variations influencing the results.

Chapter 6

Solar Variability influence on the Geoelectric field

In this chapter, model-calculated imposed polar cap potentials above Vostok station are compared with the ground measured vertical geoelectric field, thus enabling comment on the influence of the solar wind on the near surface geoelectric field in the polar caps, and on the accuracy of the models in estimating the potential difference above the site.

Several electric potential models have emerged that provide estimates of the convection patterns and electric potentials above any given point from values of the Interplanetary Magnetic Field and the solar wind velocity. Two of these models, the Weimer [1996] and the IZMEM Papitashvili et al. [1994] model, are used to calculate the imposed polar cap potentials above Vostok Station. Although the IZMEM model has been recently recalibrated utilizing the DMSP electrostatic potentials Papitashvili et al. [1999], we have chosen to use only the 1994-IZMEM model (hereafter referred to as the IZMEM model). This allows a comparison to be made between the different techniques and data used to derive the models (refer to Chapter 3 for details of the two models).

Electric field measurements observed near the surface are inversely proportional to the local atmospheric conductivity. For this reason, sites with diurnal variations in local conductivity are rarely suitable for investigating the global

electric circuit. Day to day and long term influences on the electric field measurements, due to varying local atmospheric conductivity, varying cosmic ray fluxes, high wind speeds or subvisual ice particles, are removed by normalising the electric field measurements such that the daily average of the electric field values is equal to the average of the entire dataset. This process effectively attributes the variation in the daily averaged electric field measurements solely to the conductivity at the surface and removes any influence of the daily average of the ionospheric potential.

The effect of the global fair weather diurnal variation is subtracted from the normalised electric field values before comparison with the model-calculated imposed polar cap potentials above Vostok station. The global fair weather diurnal curve is, however, not implicitly known but can be approximated using the measured electric field values. Two approaches have been used to approximate the global diurnal curve, one by Tinsley et al. [1998] and the other by Park [1976a]. The Tinsley method involved scaling the Carnegie curve by a factor equal to the average of all the observed electric field measurements, subtracting 250 Vm^{-1} and then subtracting these values from the observed electric field values. The Park [1976a] method approximates the global diurnal variation by using the hourly means of the measured electric field values. Linear regression analysis is then used to compare these residual values with the similarly treated, modelled Vostok convection potentials. In this study, two methods are used to treat the electric field measurements, a monthly method [Frank-Kamenetsky et al., 1999] and a yearly method [Frank-Kamenetsky et al., 2001], both based on the Park [1976a] method.

6.1 Methods of analysis

The electric field values are normalised by the corresponding daily averages. Normalised electric field values are calculated as ratios of the average daily values,

$$E_n(d,h) = \frac{E(d,h)}{\bar{E}(d)}, \tag{6.1}$$

where $\bar{E}(d)$ is the daily average of the measured electric field values, $E(d, h)$. The averaged diurnal variations of the Vostok 1998 electric field measurements can be associated with the global fair-weather diurnal variation and, hence, can be considered as background curves for the separation of the influence of the solar wind imposed ionospheric electric potentials from near-surface measurements of the electric field. Two methods are used, a monthly, $\Delta E_n(d, h)$, and a yearly, $\Delta E_S(d, h)$, method. The basic difference between the two methods is in the calculation of the background diurnal variation.

The first method, approximates the background diurnal variations on a monthly basis. The diurnal curves of the unscaled electric field values, show variations from month to month. Variations from the monthly average are calculated by subtracting the hourly averages of each month, $\bar{E}(mth, h)$, from each corresponding $E_n(d, h)$ value,

$$\Delta E_n(d, h) = E_n(d, h) - \bar{E}(mth, h). \tag{6.2}$$

In the second method, the background diurnal variation is determined as the average of the entire dataset (106 days). The $E_n(d, h)$ values are scaled before subtracting the average electric field value for each UT hour. $E_n(d, h)$ values are scaled such that the daily average of the scaled values equals the average of the entire dataset, $\bar{E}$,

$$E_S(d, h) = E_n(d, h) \times \bar{E} \qquad (Vm^{-1}). \tag{6.3}$$

Variations from the average electric field values are calculated as,

$$\Delta E_S(d, h) = E_S(d, h) - \bar{E}_S(h) \qquad (Vm^{-1}). \tag{6.4}$$

The assumption with this method is that the electric circuit does not vary significantly from one part of the year to another and it is sufficient to look at the dispersion of normalised electric field values from the yearly hourly averages.

Variations in the imposed polar cap potentials, $\Delta\phi(d, h)$, were determined in a similar manner to the two methods described. The potentials across each day were centred about a zero level to match the forcing imposed on the scaled electric field

values but still maintaining the magnitude of the difference in kilovolts. Weimer and IZMEM model predicted variations in the imposed polar cap potentials above Vostok are calculated as

$$\Delta\phi(\mathrm{d,h}) = \phi(\mathrm{d,h}) - \phi(\bar{\mathrm{h}}) - [\bar{\phi} - \bar{\phi}(\mathrm{d})] \quad (\mathrm{kV}). \tag{6.5}$$

Linear fits of $\Delta E_S(\mathrm{d,h})$ and $\Delta E_n(\mathrm{d,h})$ against $\Delta\phi(\mathrm{d,h})$ are determined for each UT hour and for both Weimer and IZMEM calculated Vostok convection potentials. The regression correlations are described as significant if the chance probability (P-value) is less than 5%.

An average convection potential of $\sim$ 250 kV generates an average vertical electric field near the ground at Vostok of 177 Vm^{-1}. The expected slope of correlation is $\sim$ 0.71 $\mathrm{Vm}^{-1}/\mathrm{kV}$.

6.2 Results

Figure 6.1 shows the average diurnal variation of the imposed polar cap potential above Vostok as inferred by both the Weimer and the IZMEM models. Although the two models show considerable difference in thèir predictions, the average diurnal range for both is $\sim$ 25 kV, about 10% of the average global circuit magnitude.

Linear fits are calculated of $\Delta E(\mathrm{d,h})$ against $\Delta\phi(\mathrm{d,h})$ for each UT hour for both Weimer and IZMEM models and both monthly and yearly method of treating the ground measured electric field values. Figure 6.2 shows the results for the IZMEM model for the hour 12 UT to 13 UT (hereafter referred to as 12.5UT) for both the monthly and the yearly methods. Figure 6.3 shows similar results for the Weimer model. Considerable noise is apparent in the $\Delta E(\mathrm{d,h})$ values. This is not unexpected due to day-to-day variations in the global electric circuit which are not expected to correlate with $\Delta\phi(\mathrm{d,h})$ values. However, both Weimer and IZMEM linear correlations for this particular UT hour are significant with chance probabilities of less than 1%. Figures 6.4 and 6.5 show the slope of the linear fits ($\mathrm{Vm}^{-1}/\mathrm{kV}$) and the chance probabilities for each UT hour for the IZMEM model

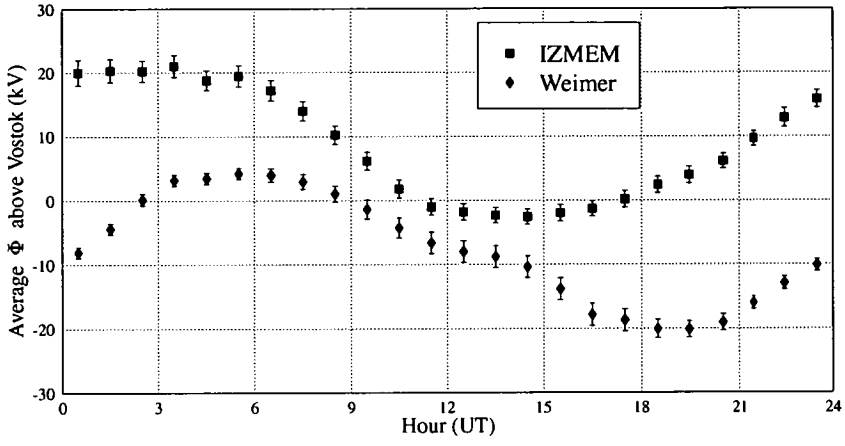

Figure 6.1: Average Weimer and IZMEM model calculated polar cap potential differences above Vostok for the 106 days analysed. Standard errors for each hour are also plotted

using the monthly and the yearly methods, respectively. Figures 6.6 and 6.7 shows similar results for the Weimer model. Standard errors are plotted on the slope values in all figures. The slope values for the IZMEM and Weimer monthly method analyses were scaled by 176.6 Vm^{-1}, the average electric field value, to allow a direct comparison with the expected slope value of 0.71 Vm^{-1}/kV. For the Weimer model, the slope obtained from combining all data is 0.66 Vm^{-1}/kV for the monthly method and 0.77 Vm^{-1}/kV for the yearly method (compared to the expected slope of 0.71 Vm^{-1}/kV). The linear correlations are significant for 20 and 19 individual hours, respectively. For the monthly method, the individual hours are generally significantly correlated across the magnetic daylight hours (magnetic noon $\sim$ 13 UT) and near magnetic midnight. The yearly method yields a similar spread in significant correlation hours. The individual hours are significantly correlated across almost all magnetic daylight hours, with 14.5 UT almost significantly correlated at 7.7%, and around magnetic midnight. The average slope across significantly correlated hours was 0.72 Vm^{-1}/kV for the monthly method and 0.89 Vm^{-1}/kV for the yearly method.

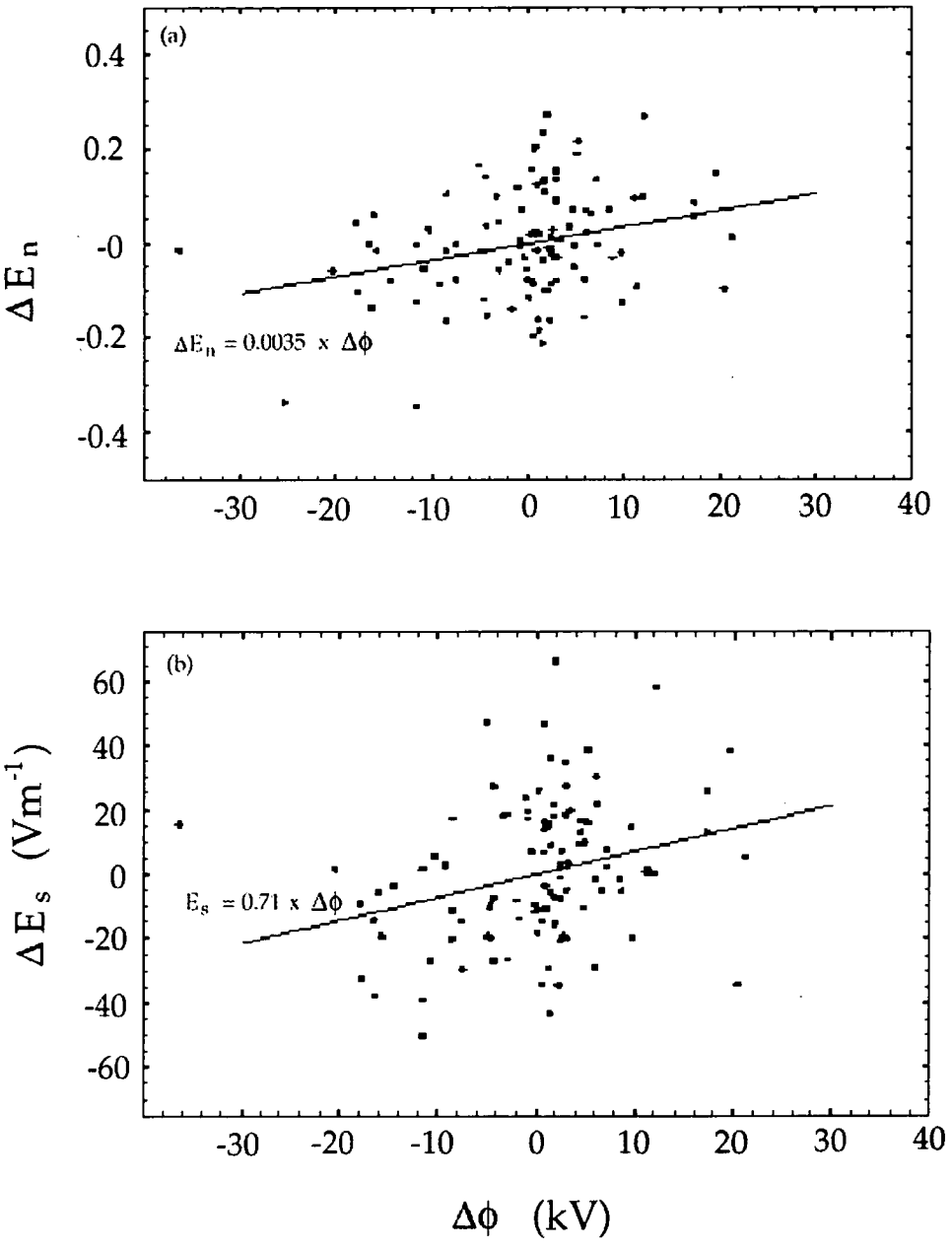

Figure 6.2: Linear fits of IZMEM calculated imposed polar cap potentials and variations in the ΔE for 12.5 UT. (a) $\Delta E_n(d, h)$ against $\Delta\phi(d, h)$, the monthly method. (b) $\Delta E_S(d, h)$ against $\Delta\phi(d, h)$, the yearly method.

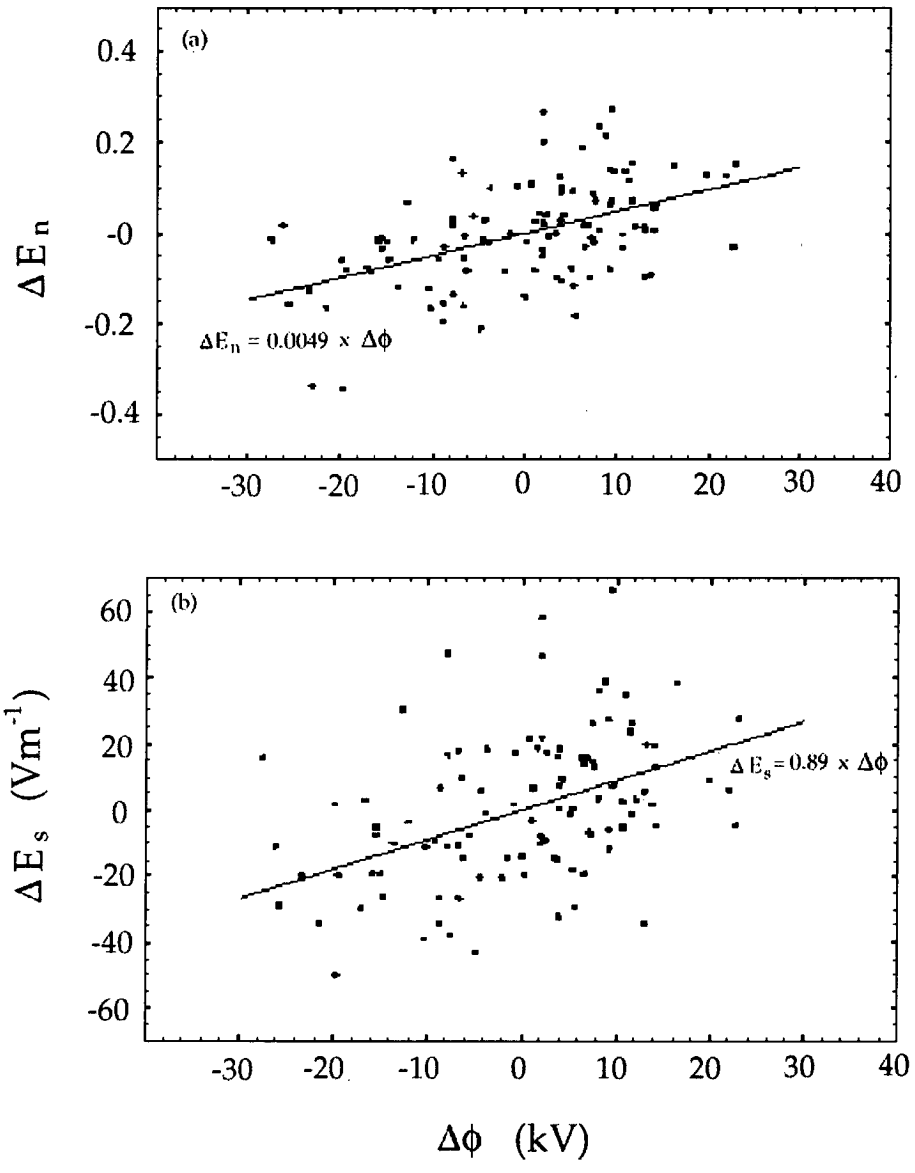

Figure 6.3: As per Figure 6.2, but using Weimer calculated imposed polar cap potentials.

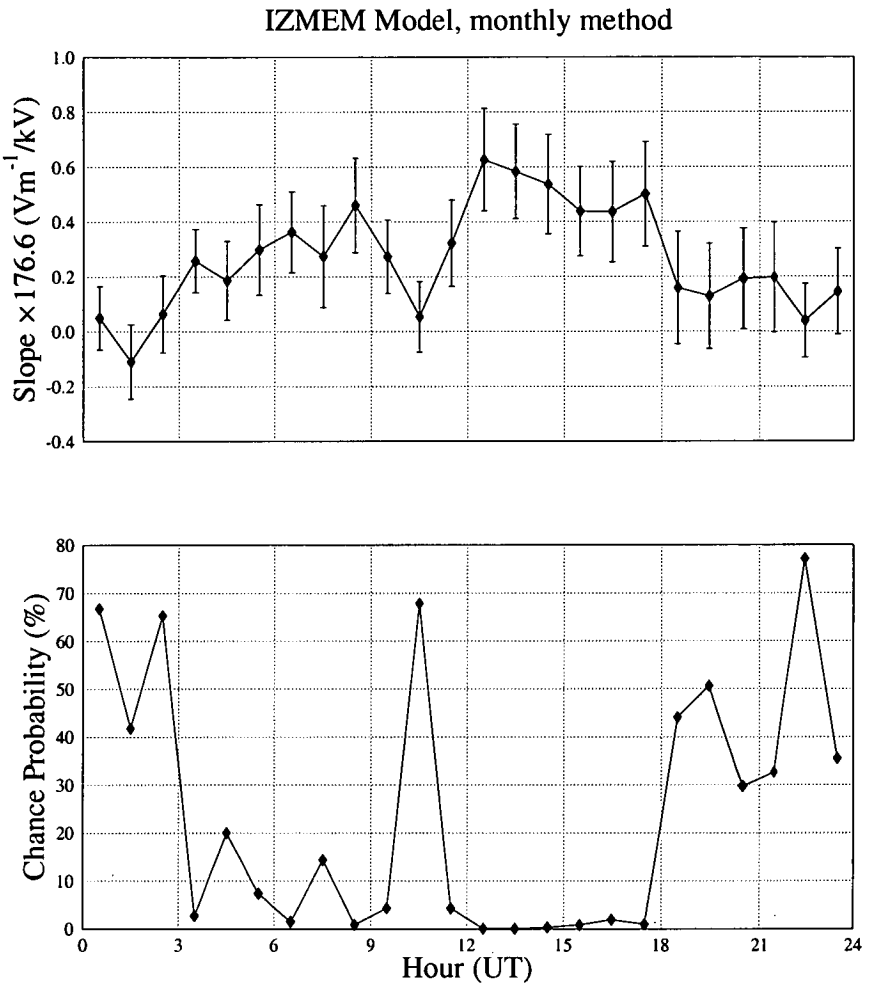

Figure 6.4: The slope of the straight line fits for variations in the scaled geoelectric field values, ΔE_n, and variation in the IZMEM modelled imposed polar cap potentials above Vostok, $\Delta\phi$, for each UT hour; and the associated P-value, the probability that the association is due to chance. The slope values and the associated standard errors were scaled by a factor of 176.6 Vm^{-1}. The error bars are $\pm$ one standard error. Local noon at Vostok occurs at $\sim$ 5 UT and local magnetic noon at $\sim$ 13 UT.

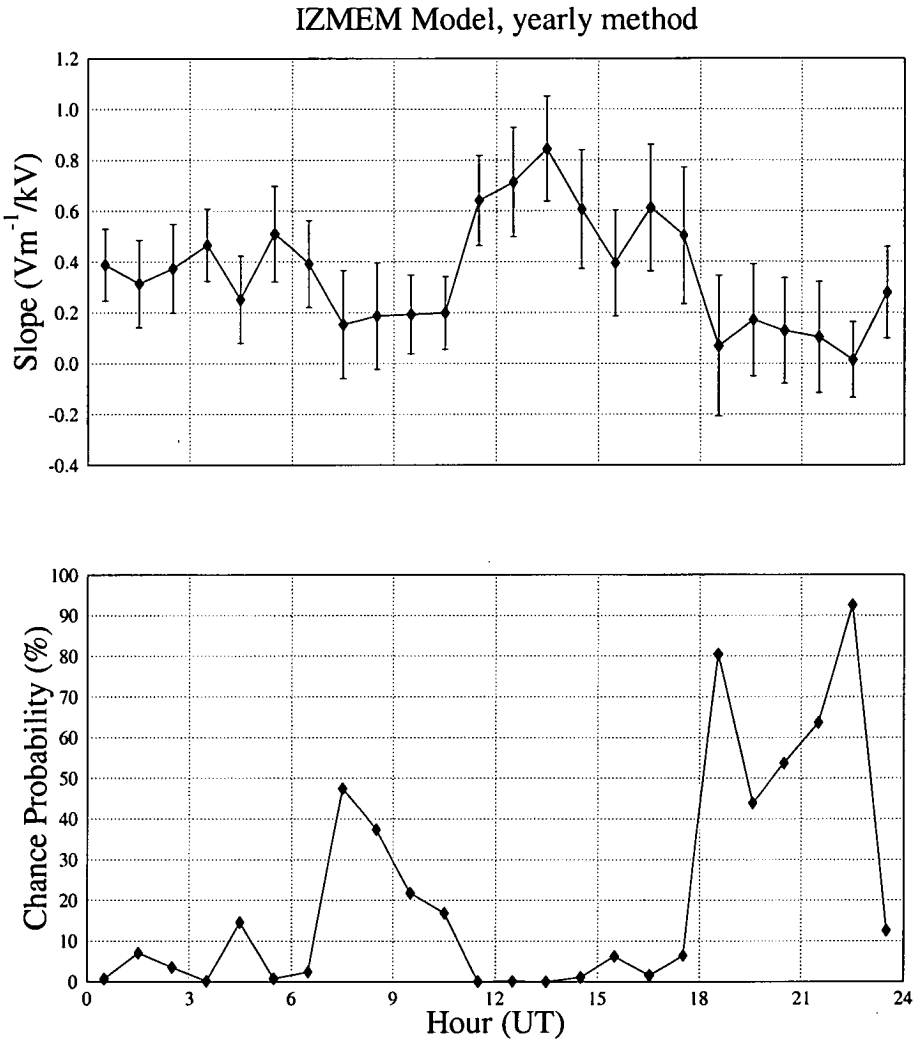

Figure 6.5: The slope of the straight line fits for variations in the scaled geoelectric field values, ΔE_S, and variation in the IZMEM modelled imposed polar cap potentials above Vostok, $\Delta\phi$, for each UT hour; and the chance probability. Local noon at Vostok occurs at $\sim$ 5 UT and local magnetic noon at $\sim$ 13 UT.

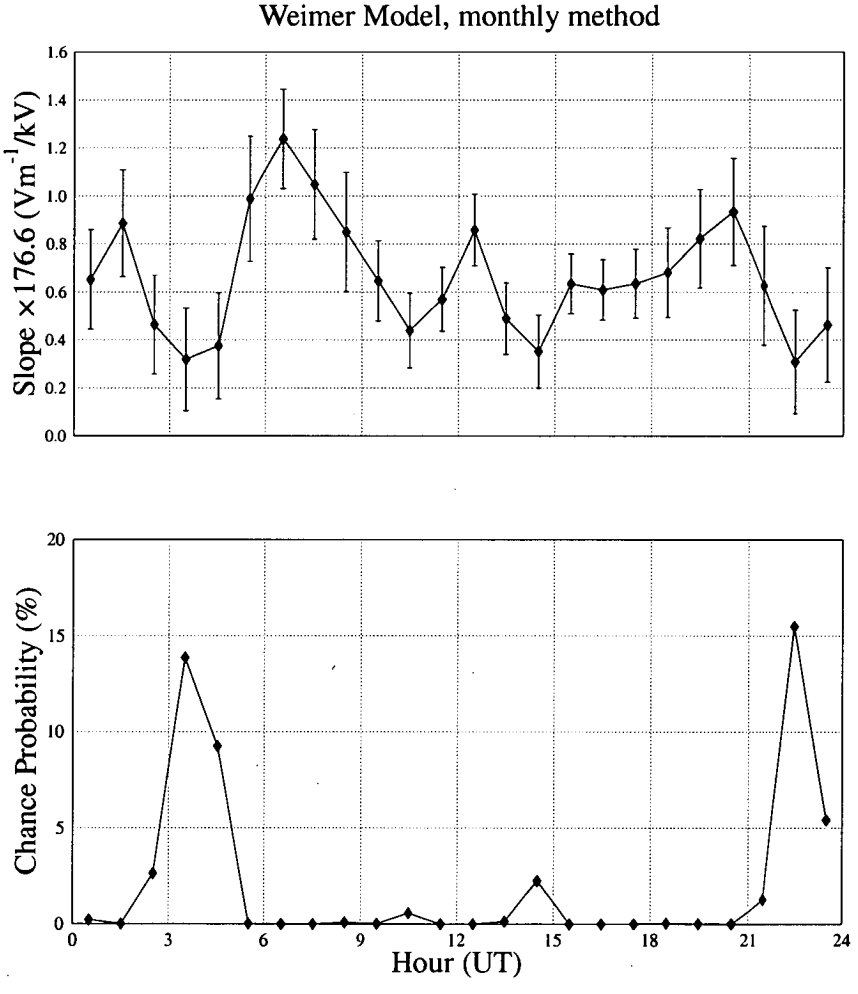

Figure 6.6: As per Figure 6.4 but using Weimer modelled imposed polar cap potentials above Vostok station.

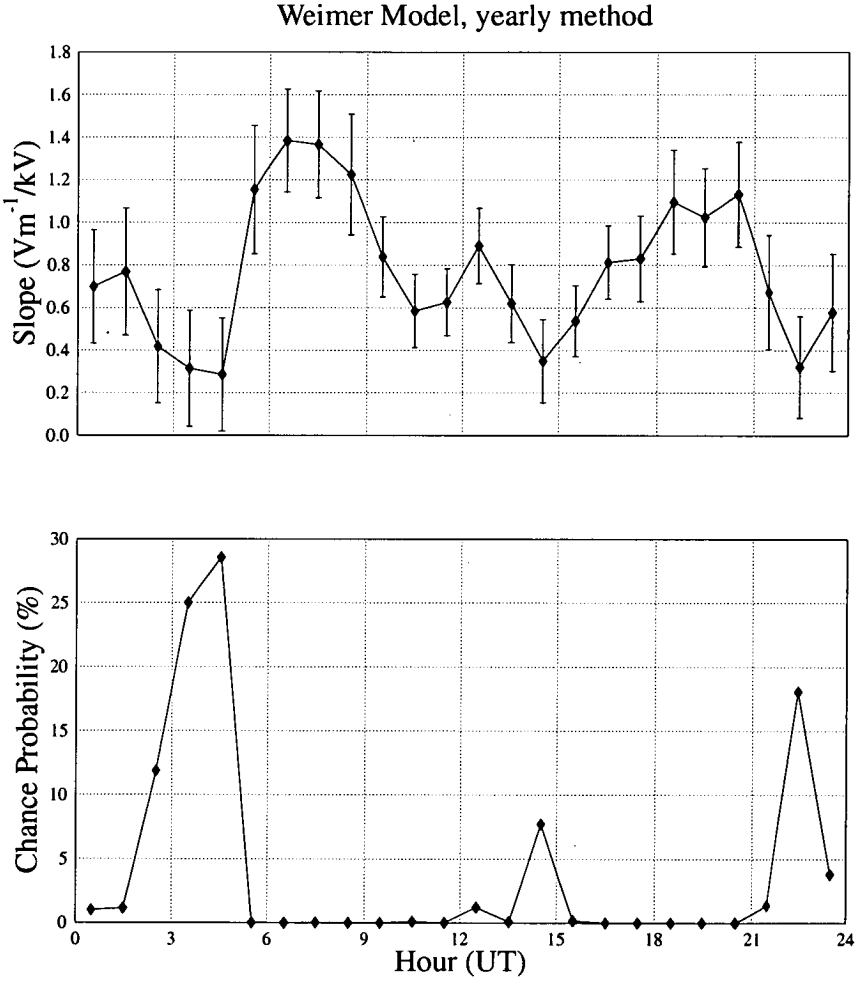

Figure 6.7: As per Figure 6.5 but using Weimer modelled imposed polar cap potentials above Vostok.

For the IZMEM model, the slope obtained from combining all data is only 0.29 Vm^{-1}/kV for the monthly method and 0.35 Vm^{-1}/kV for the yearly method. Significant correlations are obtained for 11 and 10 individual hours ranging from magnetic midnight to four hours after magnetic noon ($\sim$ 13 UT). The average slope for these significant hours is 0.44 Vm^{-1}/kV for the monthly method and 0.55 Vm^{-1}/kV for the yearly method.

6.3 Discussion

Frank-Kamenetsky et al. [1999] used the 1994-IZMEM model to investigate the influence of the imposed polar cap potentials above Vostok on geoelectric field measurements for 36 fair weather days at Vostok from 1979. The analysis procedure used by Frank-Kamenetsky et al. [1999] is similar to the yearly method presented here and found significant correlations for six individual UT hours. Using a modern digital data set, the same IZMEM model and similar analysis techniques, we have found significant correlations for 10 individual UT hours. Using the Weimer model and the yearly method we found significant correlations for 19 individual hours. The improvement appears to be principally due to the change of model. Use of a second analysis technique, the monthly method, resulted in a similar improvement; 11 significant UT hours for the IZMEM model compared to 20 significant UT hours for the Weimer model.

The range of hours for which the Weimer imposed polar cap potentials were significantly correlated were similar for both monthly and yearly methods. The uncorrelated hours were dominantly located on either side of magnetic midnight ($\sim$ 1 UT). The imposed polar cap potential distribution is a magnetic coordinate associated phenomena and a degree of symmetry is understandable. With the monthly method, this symmetry is reflected in the spread of significant UT hours. With the yearly method, however, the post-magnetic midnight interval of non-significant correlations (2.5 UT to 4.5 UT) is broader than the pre-midnight interval (22.5 UT to 23.5 UT) and may be associated with local conductivity

variations around local noon ($\sim$ 5 UT). The pattern of significantly-correlated UT hours is not as clear with the IZMEM imposed polar cap potentials. The significant hours range from 0.5 UT to 17.5 UT, with an apparent symmetry about 10.5 UT, for the monthly method, and 6.5 UT – 11.5 UT, for the yearly method. The results of Frank-Kamenetsky et al. [1999] are similar if some allowance is made for the larger modern dataset. The six significantly correlated UT hours were in the range 3.5 UT to 14.5 UT.

Both the Weimer and the IZMEM models seek to determine the imposed polar cap potential distribution from solar wind parameters. The polar ionosphere, directly linked to the dayside magnetosphere, may be more predictable from solar wind parameters whereas nightside activity may be less directly related due to storage and release mechanisms associated with the magnetotail. It is interesting to note that three significantly correlated Weimer model UT hours, 23.5 – 1.5 UT, for the yearly method and two, 1.5 – 2.5 UT, for the monthly method, extend across magnetic midnight.

The IZMEM model used in these investigations derives the imposed polar cap potential distribution above Vostok from ground based magnetic measurements and an E-region conductivity model. The magnetic signature of an imposed polar cap potential distribution is larger and thus more readily distinguishable when there is significant ionisation in the altitude range where ionospheric currents flow (120 – 160 km). The two principal sources of ionisation at these altitudes are solar EUV electromagnetic radiation and particle precipitation. At the magnetic latitude of Vostok, particle precipitation will generally be centred around magnetic noon. The ease of discerning the ground magnetic signal of the imposed polar potential distribution may be a contributing factor to the significantly correlated hours extending slightly beyond the interval between local noon and magnetic noon. The difference in the number of significant correlations between the Weimer and the IZMEM model analyses may indicate advantages of the Weimer model inputs over those of the IZMEM model. Both models use IMF B_z and B_y but the Weimer model uses solar wind speed as the third parameter rather than IMF B_x.

The Weimer model has a continuously variable seasonal parameter, the dipole tilt angle, whereas IZMEM allows for broad seasonal variations via splitting the data into summer, winter and equinox intervals. Satellite-measured ionospheric electric fields are more direct measurements of polar convection than ground-based magnetometer measurements that require interpretation via an ionospheric conductivity model, thus explaining the better correlation on the nightside, for the Vostok site, for Weimer calculated imposed polar cap potentials. The vertical geoelectric field measurements are expected to be significantly correlated with the large scale features of the imposed polar cap potential distribution above Vostok at all times [Park, 1976a], however, both models have the problem that it is physically unclear how well solar wind conditions can directly control the applied polar cap potential on the nightside.

Chapter 7

Conclusion

The rotating dipole electric field mill deployed at Vostok Station, Antarctica in December 1997 has to date collected several years of digital, calibrated, geoelectric field measurements. A total of 133 fair-weather days of vertical geoelectric field data were selected for further analysis from observations made during its first year of operation, 1998. Fair-weather diurnal curves, observed in the near-surface geoelectric field measurements, and seasonal variations in the diurnal electric field are similar to reported features of the Carnegie curves. These results re-confirm Vostok station as a suitable location for studies of the global electric circuit.

The interaction of the solar wind and the Earth's magnetic field imposes on the geoelectric field a variable dawn-to-dusk potential drop of $20-150$ kV. Large-scale horizontal electric fields in the ionosphere map into the vertical component of the near-surface electric field. The existence of a linkage between the solar-wind-imposed potential distribution and the near-surface electric field has been clearly demonstrated in this study. Subtracting the contribution of the solar wind imposed polar cap potentials above Vostok from the near-surface electric field values results in an increase in the range of the diurnal curve from 28% to 36% of the mean value. This range value is similar to the Carnegie value of 37%, indicating the significant influence of the solar wind-magnetosphere interaction on near-surface vertical electric field measurements.

The ionospheric electric potentials are linearly related to measurements of

the near-surface electric field. For the Vostok site, the expected ratio is $\sim$ 0.71 Vm^{-1}/kV. Correlations of the electric field at Vostok with the imposed polar cap potentials above Vostok predicted using the Weimer and IZMEM models resulted in up to 20 significantly correlated UT hours. Weimer model potential differences produced significantly better results than similar correlations using IZMEM potential differences, irrespective of the method used to calculate variations of the average electric field values (ΔE_S or ΔE_n). Weimer model potential differences resulted in significant correlations for 19 individual hours and an average slope of 0.77 Vm^{-1}/kV using the yearly method and 20 significant hours and a slope of 0.66 Vm^{-1}/kV using the monthly method. IZMEM model potentials resulted in 10 and 11 significant correlations and average slope values of 0.35 Vm^{-1}/kV and 0.29 Vm^{-1}/kV.

Only one significantly correlated hour separated the monthly and yearly methods, however, the average slopes of the lines of best fit differed by up to 0.2 Vm^{-1}/kV. The yearly method consistently yielded higher average slope values but both the average slope values are within 10% of the expected value, 0.77 Vm^{-1}/kV. The average diurnal variations of the electric field do themselves change from month to month, justifying calculating variations from the monthly averages. However, the number of fair-weather days contained within each month, for the 106 days, varies from 3 days in February to 13 days for January, April, September and December. Average hourly electric field values for February are calculated from only 3 values and the error associated with the hourly means are greater for this month than compared with other months. Obviously, more data is required for the use of this method. In the short-term this is not feasible. Of the 365 days of electric field data observed at Vostok, 133 days were judged suitable for further analysis and of these, IMF and solar wind speed data were available for only 106 days. For the Vostok 1998 data, two distinct groupings can be seen in the monthly diurnal variations. The diurnal variations for May, June and July appear to be similar, the range is minimal in all three months and the distinct shape of the Carnegie curve is not evident. The months of January to April and August

to December show evidence of Carnegie-like curves, peaking between 18 UT and 21 UT and displaying two other peaks around 6 UT and 15 UT. A method of calculating variations of the average electric field values based on this 3/9 month split may be more applicable than either yearly or monthly methods.

The difference in the number of significantly correlated hours between the two model analyses may indicate advantages of the Weimer model inputs over those of the IZMEM model. Both models use IMF B_z and B_y as solar wind input parameters, but the Weimer model uses solar wind speed as a third parameter rather than IMF B_x. The Weimer model has a continuously variable seasonal parameter, the dipole tilt angle, whereas IZMEM allows for broad seasonal variations via splitting the data into summer, winter and equinox intervals. Satellite measured ionospheric electric fields are more direct measurements of polar convection than ground-based magnetometer measurements that require interpretation via an E-region conductivity model. This may specifically explain the Weimer model's better performance on the nightside for the Vostok site. Both models, however, lack details associated with nightside processes; the plasma convection and potentials near midnight are influenced by substorm activity in the magnetotail and the models cannot accurately predict the convection patterns during magnetic substorms [Weimer, 2001].

An array of electric field mills on the Antarctic plateau has been proposed as a means of determining the instantaneous imposed polar cap potential distribution independent of any E-region ionisation [Byrne et al., 1993, Tinsley et al., 1998]. With a single site the variable meteorological contribution to the vertical electric circuit can only be removed by averaging. However, having demonstrated the linkage between the solar wind imposed potential pattern and the ground-based electric field signal [see also Tinsley et al., 1998, Frank-Kamenetsky et al., 1999] we can assert that the ratio linking these factors should be constant. Cosmic ray ionisation dominantly controls the resistance in the atmospheric column between the lower reaches of the ionosphere and the ground and shows no variation of significance to our measurements. As noted previously, the constant factor for

the Vostok site is $\sim$ 0.71 Vm^{-1}/kV. We cannot infer any information from our analysis about the absolute value of the imposed polar cap potentials in the ionosphere above Vostok with respect to the zero reference level (at CGM latitude 57°). However, the diurnal variation of the slope of the relationship between ΔE_S and $\Delta\phi$ indicates how appropriately the two models respond to solar wind induced variations in the potential difference above Vostok. The variation of the Weimer model potential above Vostok as the solar wind varies is too small between 5.5 and 8.5 UT, for both monthly and yearly methods (average slope $\sim$ 1.3 Vm^{-1}/kV and $\sim$ 1.0 Vm^{-1}/kV, respectively) and between 18.5 UT and 20.5 UT for the yearly method only (average slope $\sim$ 1.1 Vm^{-1}/kV and consistent with ground-level measurements of the vertical geoelectric field across the other hours for which significant correlations are obtained. Variation of the IZMEM model potential above Vostok as the solar wind varies is consistent with ground-level measurements of the vertical electric field field, using the yearly method, between 11.5 to 14.5 UT and 16.5 UT (average slope of $\sim$ 0.68 Vm^{-1}/kV), using the monthly method, between 12.5 and 14.5 UT and 17.5 UT (average slope of $\sim$ 0.58 Vm^{-1}/kV) and too large across other hours for which significant correlations are obtained.

The new IZMEM model, IZMEM/DMSP, uses ionospheric electrostatic potentials obtained from thermal ion drift measurements made by the DMSP (Defense Meteorological Satellite Program) satellites to recalibrate the IZMEM ionospheric electric potentials [Papitashvili et al., 1999] but does not include the influence of magnetic substorms. The latest Weimer model [Weimer, 2001] includes the influence of magnetospheric substorms or nightside processes in the magnetotail; it allows for more realistic predictions of the ionospheric potentials for larger input values of the IMF and allows the lower boundary of the potential patterns to vary according to the conditions rather than be fixed at an arbitrary location. Weimer [2001] demonstrated that the use of only IMF data to predict the electric potential patterns in the polar regions was inadequate especially during magnetic substorms. In a recent development, Papitashvili and Rich [2002] constructed

a series of high-latitude ionospheric convection models using DMSP thermal ion drift measurements. The DMSP Ionospheric Convection Model (DICM) can construct ionospheric convection patterns for any IMF configurations during quiet to moderate geomagnetic conditions. It is similar to the latest Weimer model but is fully parameterised by IMF strength and direction. These newer ionospheric electric potential models should account for the weaknesses noted in the 1994-IZMEM and Weimer models.

The electric field mill at Vostok station has been in operation since 1998 and several years of electric field data are available for analysis. This extensive dataset, comprising of fair-weather days selected from three years of electric field data, will facilitate further investigations into the relationship between solar wind imposed ionospheric electric potentials and near-surface electric field meausrements, using more recent ionospheric electric potential models. Further possibilities include investigations into the relationship between global thunderstorm activity and ionospheric potential and the role of the global electric circuit and thunderstorm activity in climate change.

Bibliography

E J Adlerman and E R Williams. Seasonal variation of the global electric circuit. *Journal of Geophysical Research*, 101(D23):29679, 1996.

E A Bering. The global circuit: Global thermometer, weather by-product or climatic modulator? *Reviews of Geophysics, Supplement*, 33:845, 1995.

E A Bering, A A Few, and J R Benbrook. The global electric circuit. *Physics Today*, 51:24, 1998.

G Brasseur and S Solomon. *Aeronomy of the Middle Atmosphere.* D Reidel Publishing Company, 1986.

G B Burns, A V Frank-Kamenetsky, O A Troshichev, E A Bering, and V O Papitashvili. The geoelectric field: A link between the troposphere and solar variability. *Annals of Glaciology*, 27:651, 1998.

G B Burns, M H Hesse, S K Parcell, S Malachowski, and K D Cole. The geoelectric field at Davis station, Antarctica. *Journal of Atmospheric and Terrestrial Physics*, 57(14):1783, 1995.

G J Byrne, J R Benbrook, and E A Bering III. Balloon observations of stratospheric electricity above the South Pole: Vertical electric field, conductivity, and conduction current. *Journal of Atmospheric and Terrestrial Physics*, 53 (9):859, 1991.

G J Byrne, J R Benbrook, E A Bering III, A A Few, G A Morris, W J Trabucco, and E W Pashal. Ground-based instrumentation for measurements of

atmospheric conduction current and electric field at the South Pole. *Journal of Geophysical Research*, 98(D2):2611, 1993.

W R Cotton and R A Anthes, editors. *Storm and Cloud Dynamics.* Academic Press, Inc, 1989.

K Davies. *Ionospheric Radio.* Peter Peregrinus Ltd, 1990.

H Dolezalek and R Reiter, editors. *Electrical Processes in Atmospheres.* Dr. Deitrich Steinkopff Verlag, 1977.

J Fishman, P N Bhat, R Mallozzi, J M Horack, T Koshut, C Kouveliotou, G N Pendleton, C A Meegan, R B Wilson, W S Paciesas, S J Goodman, and H J Christian. Discovery of intense gamma-ray flashes of atmospheric origin. *Science*, 264:1313, 1994.

J C Foster. An empirical electric field model derived from Chatanika radar data. *Journal of Geophysical Research*, 88:981, 1983.

A V Frank-Kamenetsky, G B Burns, O A Troshichev, V O Papitashvili, E A Bering, and W J R French. The geoelectric field at Vostok, Antarctica: It's relation to the interplanetary magnetic field and cross polar cap potential difference. *Journal of Atmospheric and Terrestrial Physics*, 61:1347, 1999.

A V Frank-Kamenetsky, O A Troshichev, G B Burns, and V O Papitashvili. Variations of the atmospheric electric field in the near pole region related to the interplanetary magnetic field. *Journal of Geophysical Research*, 106(A1): 179, 2001.

E Friis-Christensen, Y Kamide, A D Richmond, and S Matsushita. Interplanetary magnetic field control of high-latitude electric field and currents determined from Greenland magnetometer data. *Journal of Geophysical Research*, 90:1325, 1985.

E Friis-Christensen and K Lassen. Length of the solar cycle: an indicator of solar activity closely associated with climate. *Science*, 254:698, 1991.

H Fukunishi, Y Takahashi, MKubota, and K Sakanoi. Elves: Lightning-induced transient luminous events in the lower ionosphere. *Geophysical Research Letters*, 23(16):2157, 1996.

M R Hairston and R A Heelis. Model of the high-latitude ionospheric convection pattern during southward interplanetary magnetic field using DE 2 data. *Journal of Geophysical Research*, 95(A3):2333, 1990.

P B Hays and R G Roble. A quasi-static model of global atmospheric electricity. 1. the lower atmosphere. *Journal of Geophysical Research*, 84(A7):3291, 1979.

R A Heelis, K Lovell, and R W Spiro. A model of the high-latitude ionospheric convection pattern. *Journal of Geophysical Research*, 87:6339, 1982.

J P Heppner and N C Maynard. Empirical high-latitude electric field models. *Journal of Geophysical Research*, 92(A5):4467, 1987.

U S Inan, C Barrington-Leigh, S Hansen, V S Glukhov, and T F Bell. Rapid lateral expansion of optical luminosity in lightning-induced ionospheric flashes referred to as 'elves'. *Geophysical Research Letters*, 24(5):583, 1997.

H Israel. *Atmospheric Electricity, volume I and II*, volume I and II. Israel Program for Scientific Translations, 1973.

Y Kamide, A D Richmond, and S Matsushita. Estimation of ionospheric electric fields, ionospheric currents and field-aligned currents from ground magnetic records. *Journal of Geophysical Research*, 86:801, 1981.

J H King and N E Papitashvili. On adding Wind/SWE plasma data to omni. http://nssdc.gsfc.nasa.gov/OMNIweb, 1999.

J Lean, J Beer, and R Bradley. Reconstruction of solar irradiance since 1610: Implications for climate change. *Geophysical Research Letters*, 22(23):3195, 1995.

A E Levitin, R G Afonina, B A Belov, and Ya I Feldstein. Geomagnetic variation and field-aligned currents at northern high-latitudes, and their relations to the solar wind parameters. *Philosophical transactions of the Royal Society of London*, 304:253, 1982.

N D Marsh and H Svensmark. Low cloud properties influenced by cosmic rays. *Physical Review Letters*, 85(23):5004, 2000.

B M McCormac, editor. *Atmospheres of Earth and the Planets. Proceedings of the Summer Advanced Study Institute.* D. Reidel, 1974.

V M Mishin, A D Bazarzhapov, and G B Shpynev. Electric fields and currents in the Earth's magnetosphere, in: Dynamics of the magnetosphere. page 249, 1980.

V O Papitashvili, B A Belov, Ya I Feldstein D S Faermark, S A Golyshev, L I Gromova, and A R Levitin. Electric potential patterns in the northern and southern polar regions parameterized by the interplanetary magnetic field. *Journal of Geophysical Research*, 99(A7):13251, 1994.

V O Papitashvili, C R Clauer, A E Levitin, and B A Belov. Relationship between the observed and modelled modulation of the dayside ionospheric convection by the IMF B_y component. *Journal of Geophysical Research*, 100(A5):7715, 1995.

V O Papitashvili and F J Rich. High-latitude ionospheric convection models derived from dmsp ion drift observations and parameterized by the imf strength and direction. Accepted for publication in Journal of Geophysical Research, 2002.

V O Papitashvili, F J Rich, M A Heinemann, and M R Hairston. Parameterization of the defense meteorological satellite program ionospheric electrostatic potentials by the interplanetary magnetic field strength and direction. *Journal of Geophysical Research*, 104(A1):177, 1999.

C G Park. Downward mapping of high-latitude ionospheric electric fields to the ground. *Journal of Geophysical Research*, 81(1), 1976a.

C G Park. Solar magnetic sector effects on the vertical atmospheric electric field at Vostok, Antarctica. *Geophysical Research Letters*, 3(8), 1976b.

C G Park and M Dejnakarintra. The effects of magnetospheric convection on atmospheric electric fields in the polar cap. In H Dolezalek and R Reiter, editors, *Proceedings of the 5th International Conference on Atmospheric Eelctricity*, page 536, 1977.

W C Parkinson and O W Torreson. The diurnal variation of the electric potential of the atmosphere over the oceans. *UGGI Bulletin*, 8:340, 1931.

R Reiter. *Phenomena in Atmosheric and Environmental Electricity.* Elsevier, 1992.

F J Rich and M Hairston. Large-scale convection patterns observed by DMSP. *Journal of Geophysical Research*, 99:3827, 1994.

F J Rich and Y Kamide. Mapping electrodynamic features of the high-latitude ionosphere from localized observations: Technique. *Journal of Geophysical Research*, 93:5741, 1988.

A J Ridley, G Lu, C R Clauer, and V O Papitashvili. A statistical study of the ionospheric convection response to changing interplanetary magnetic field conditions using the assimilative mapping of ionospheric electrodynamics technique. *Journal of Geophysical Research*, page 4023, 1998.

R G Roble and I Tzur. The global atmospheric electric circuit. In *The Earth's Electrical Environment*, page 206. National Academic Press, Washington, D. C., 1986.

C J Rodger. Red sprites, upward lightning, and VLF perturbations. *Reviews of Geophysics*, 37(3):317, 1999.

J M Ruohoniemi and R A Greenwald. Statistical patterns of high-latitude convection obtained from Goose Bay HF radar observations. *Journal of Geophysical Research*, 101(A10):21, 1996.

M J Rycroft, S Israelsson, and C Price. The global atmospheric electric circuit, solar activity and climate change. *Journal of Atmospheric and Terrestrial Physics*, 62:1563, 2000.

D D Sentman and E M Wescott. Red sprites and blue jets: High altitude optical emissions linked to lightning. *EOS Transactions, American Geophysical Union*, 77:1, 1996.

H Svensmark and E Friis-Christensen. Variation of cosmic ray flux and global cloud coverage - a missing link in solar-climate relationships. *Journal of Atmospheric and Terrestrial Physics*, 59(11):1225, 1997.

L Symons. Electric field mill technical manual. Technical report, Australian Antarctic Division, 1997. Preliminary Version.

B A Tinsley. Do effects of global atmospheric electricity on clouds cause climate changes. *EOS, Transactions, AGU*, 78(33):341, 1997.

B A Tinsley. Influence of solar wind on the global electric circuit, and inferred effects on cloud microphysics, temperature, and dynamics in the troposphere. *Space Science Reviews*, 94:231, 2000.

B A Tinsley, G M Brown, and P H Scherrer. Solar variability influences on weather and climate: Possible connections through cosmic ray fluxes and storm intensification. *Journal of Geophysical Research*, 94(D12):14783, 1989.

B A Tinsley and G W Deen. Apparent tropospheric response to MeV-GeV flux variations: A connection via electrofreezing of supercooled water in high-level clouds? *Journal of Geophysical Research*, 96(D12):22283, 1991.

B A Tinsley and R A Heelis. Correlations of atmospheric dynamics with solar activity evidence for a connection via the solar wind, atmospheric electricity, and cloud microphysics. *Journal of Geophysical Research*, 98(D6):10375, 1993.

B A Tinsley, Weiping Liu, and R P Rohrbaugh. South Pole electric field responses to overhead ionospheric convection. *Journal of Geophysical Research*, 103(D20): 26137, 1998.

F Verniani, editor. *Structure and Dynamics of the Upper Atmosphere: Proceedings of the 2nd Course of the International School of Atmospheric Physics*, 1974. Elsevier Scientific Publishing Company.

D R Weimer. Models of high-latitude electric potentials derived with a least error fit of spherical harmonic coefficients. *Journal of Geophysical Research*, 100:19595, 1995.

D R Weimer. A flexible, IMF dependent model of high-latitude electric potentials having 'space weather' applications. *Geophysical Research Letters*, 23(18):2549, 1996.

D R Weimer. Substorm influence on the ionospheric electric potentials and currents. *Journal of Geophysical Research*, 104:185, 1999.

D R Weimer. An improved model ionospheric electric potentials including substorm perturbations and application to the geospace environment modeling November 24, 1996, event. *Journal of Geophysical Research*, 106(A1):407, 2001.

E M Wescott, D Sentman, D Osborne, D Hampton, and M Heavner. Preliminary results from the Sprites94 Aircraft Campaign: 2. blue jets. *Geophysical Research Letters*, 22(10):1209, 1995.

E Williams. The Schumann resonance: A global tropical thermometer. *Science*, 256:1184, 1992.

E R Williams and S J Heckman. The local diurnal variation of cloud electrification and the global diurnal variation of negative charge on the Earth. *Journal of Geophysical Research*, 98(D3):5221, 1993.

CTR Wilson. Investigation on lightning discharges and on the electric field of thunderstorms. *Philosophical Transactions of Royal Society of London*, page 73, 1920.

R S Zuelsdorf, R J Strangeway, C T Russell, C Casler, H J Christian, and R C Franz. Trans-Ionospheric pulse pairs (TIPPs): Their geographic distributions and seasonal variations. *Geophysical Research Letters*, 24(24):3165, 1997.